Southern Methodist University

SMU Scholar

Mechanical Engineering Research Theses and Dissertations

Mechanical Engineering

Winter 12-17-2022

Novel Locomotion Methods in Magnetic Actuation and Pipe Inspection

Adam Cox
acox@smu.edu

Follow this and additional works at: https://scholar.smu.edu/engineering_mechanical_etds

Part of the Aerospace Engineering Commons, Applied Mechanics Commons, Controls and Control Theory Commons, and the Electro-Mechanical Systems Commons

Recommended Citation

Cox, Adam, "Novel Locomotion Methods in Magnetic Actuation and Pipe Inspection" (2022). *Mechanical Engineering Research Theses and Dissertations*. 50.
https://scholar.smu.edu/engineering_mechanical_etds/50

This Dissertation is brought to you for free and open access by the Mechanical Engineering at SMU Scholar. It has been accepted for inclusion in Mechanical Engineering Research Theses and Dissertations by an authorized administrator of SMU Scholar. For more information, please visit http://digitalrepository.smu.edu.

NOVEL LOCOMOTION METHODS IN MAGNETIC ACTUATION AND PIPE INSPECTION

Approved by:

Yildirim Hurmuzlu
Mechanical Engineering
Dissertation Committee Chairperson

Edmond Richer

Edmond Richer
Mechanical Engineering

Volkan Otugen
Mechanical Engineering

Peter E. Raad

Peter Raad
Mechanical Engineering

Benno Rumpf

Benno Rumpf
Mathematics

Chris Colaw
Lockheed Martin Fellow

NOVEL LOCOMOTION METHODS IN MAGNETIC ACTUATION AND PIPE INSPECTION

A Dissertation Presented to the Graduate Faculty of the
Lyle School of Engineering
Southern Methodist University
in
Partial Fulfillment of the Requirements
for the degree of
Doctor of Philosophy
with a
Major in Mechanical Engineering
by

Adam Cox

M.S., Mechanical Engineering, Southern Methodist University
B.S., Mechanical Engineering, Southern Methodist University
B.S., Mathematics, Southern Methodist University

December, 2022

Copyright (2022)

Adam Cox

All Rights Reserved

Cox, Adam M.S., Mechanical Engineering, Southern Methodist University
B.S., Mechanical Engineering, Southern Methodist University
B.S., Mathematics, Southern Methodist University

Novel Locomotion Methods in
Magnetic Actuation and Pipe Inspection

Advisor: Yildirim Hurmuzlu

Doctor of Philosophy conferred December, 2022

Dissertation completed December 12, 2022

There is much room for improvement in tube network inspections of jet aircraft. Often, these inspections are incomplete and inconsistent. In this paper, we develop a Modular Robotic Inspection System (MoRIS) for jet aircraft tube networks and a corresponding kinematic model. MoRIS consists of a Base Station for user control and communication, and robotic Vertebrae for accessing and inspecting the network. The presented and tested design of MoRIS can travel up to 9 feet in a tube network. The Vertebrae can navigate in all orientations, including smooth vertical tubes. The design is optimized for nominal 1.5" outside diameter tubes. We developed a model of the Locomotion Vertebra in a tube. We defined the model's coordinate system and its generalized coordinates. We studied the configuration space of the robot, which includes all possible orientations of the Locomotion Vertebra. We derived the expression for the elastic potential energy of the Vertebra's suspensions and minimized it to find the natural settling orientation of the robot. We further explore the effect of the tractive wheel's velocity constraint on locomotion dynamics. Finally, we develop a general model for aircraft tube networks and for a taut tether.

Stabilizing bipedal walkers is a engineering target throughout the research community. In this paper, we develop an impulsively actuated walking robot. Through the use of magnetic actuation, for the first time, pure impulsive actuation has been achieved in bipedal walkers. In studying this locomotion technique, we built the world's smallest walker: Big Foot. A dynamical model was developed for Big Foot. A Heel Strike and a Constant Pulse Wave

Actuation Schemes were selected for testing. The schemes were validated through simulations and experiments. We showed that there exists two regimes for impulsive actuation. There is a regime for impact-like actuation and a regime for longer duration impulsive actuation.

TABLE OF CONTENTS

LIST OF FIGURES ix
LIST OF TABLES xii
ACKNOWLEDGMENTS xiii

CHAPTER

1. Introduction 1
  1.1. Tube Inspections 1
  1.2. Millimeter Bipedal Locomotion 5
2. Problem Statement of Tube Inspections 10
  2.1. Tube Network Model 11
  2.2. Description of MoRIS 11
  2.3. Locomotion Vertebra 13
    2.3.1. Transmission 13
    2.3.2. Suspension 15
    2.3.3. Hex Roller 17
    2.3.4. Camera Vertebra 18
    2.3.5. Mirror Mechanism 20
    2.3.6. Tether 20
  2.4. Base Station 21
    2.4.1. Winding Mechanism 21
    2.4.2. Custom PCB 23
    2.4.3. Deployment 23
3. Kinematic Analysis of MoRIS 24
  3.1. Locomotion Vertebra Model 24

3.2. Kinematical Constraint Equations and Configuration Space of MoRIS . . . 24
3.3. Potential Energy in MoRIS 27
3.3.1. Configuration Constrained Space 28
3.4. Combined Vertebrae Settling Orientation 30
3.5. Velocity Constraints of MoRIS 31
3.6. Control 33
4. Localization 34
4.1. Tube Network Model 34
4.2. Tether Positioning 34
4.3. Tether Projection on Tube Centerline 35
4.4. Localization Function 35
4.5. Experimental Results of MoRIS 35
5. Methods and Materials of Big Foot 41
5.1. Robot design and manufacturing 41
5.2. Dynamics 43
5.2.1. Coordinate Frames 43
5.2.2. Hybrid System 44
5.2.3. Position Vectors 45
5.2.4. Angular Velocities 46
5.2.5. Velocity Constraint 46
5.2.6. Energy Definitions 48
5.2.7. Constraint Forces 49
5.2.8. Magnetic Moment 50
5.2.9. Impact Map 52
5.3. Actuation Scheme 54

6. Results of Big Foot 58

  6.1. Simulations 58

    6.1.1. Heel Strike Scheme Simulation Results 58

    6.1.2. Constant Pulse Wave Scheme Simulation Results 61

    6.1.3. Stability Analysis 63

    6.1.4. Constant Pulse Wave Off Time Parameter Variation 65

  6.2. Experimental Setup 68

  6.3. Experimental Results 71

    6.3.1. Data Collection 71

    6.3.2. Parameter Variation: Platform Slope 72

    6.3.3. Parameter Variation: Pulse Length 74

7. Discussion and Conclusion 75

  7.1. MoRIS 75

  7.2. Big Foot 75

APPENDIX A 77

  7.3. Localization Algorithm 77

BIBLIOGRAPHY 79

LIST OF FIGURES

Figure Page

1.1. Pure borescope tube inspection example [1]. 2

1.2. Convential borescope flexion 3

1.3. In-pipe locomotion modalities [2] 3

2.1. Tube section with geometric parameters, $\{R_j, \beta_j, C_j\}$ and tube network coordinate system: $\{s, \gamma, \rho\}$ 12

2.2. Vertebrae 12

2.3. MoRIS design structure 13

2.4. Locomotion Vertebra design structure 14

2.5. Locomotion Vertebra transmission 14

2.6. Suspension system arm free body diagram 16

2.7. Suspension normal force vs. deflection 17

2.8. Hex Roller design 18

2.9. Camera Vertebra suspension 19

2.10. Mirror mechanism 20

2.11. Base Station 22

3.1. Locomotion Vertebra diagram 25

3.2. Potential elastic energy variation vs. ρ in a straight tube segment. 28

3.3. (a) Locomotion Vertebra configuration space at $p = r$. (b) Horizontal slice at $\phi = 0$. (c) Vertical slice at $\psi = 0$. (d) Dynamic equilibrium orientation of Locomotion Vertebra. 29

3.4. Minimum energy with respect to ϕ at $p = r$. 30

3.5. Potential elastic energy variation vs. ρ in a straight tube segment for the total Vertebrae. 31

3.6. Dynamic equilibrium orientation of total Vertebrae. 32

3.7. Kinematic paths 32

3.8. User-integrated control feedback loop 33

4.1. Bent tube network experimental setup (a) and model (b). 36

4.2. Vertebrae prototype 37

4.3. Measured position vs. actual position in a straight tube 38

4.4. Localization function 40

5.1. Isometric view of the multi-body diagram of Big Foot 41

5.2. Indexed Shaft Cylinder 42

5.3. Big Foot prototypes 43

5.4. The Multi-Body Diagram of Big Foot from an frontal view 46

5.5. Side View of Foot Curvature 47

5.6. Cross-section view of magnetic field generated by the inner Helmholtz coils. . 51

5.7. Input Regimes. $\{\phi_m = 60°, \psi_{in} = 10°\}$. 55

5.8. constant pulse wave actuation example. $\{\phi_m = 35°, \psi_m = 15°, P_L = 0.06$ s$, P_m = 48.2\%, t_{off} = 0.05$ s$, I_c = 0.55$ mN-mm-s$\}$. 57

6.1. Heel Strike Actuation Scheme Bifurcation Map. 59

6.2. Poincaré Return Map for the yaw angle in a Quasi-Periodic gait. 60

6.3. Constant Pulse Wave Actuation Scheme Bifurcation Map. 62

6.4. Period-1 Limit Cycle 64

6.5. Simulation: Stride Length vs. Input Frequency. $\{\beta = 0°, \phi_m = 55°, \psi_m = 25°, I_c = 0.2 \text{ (mN-mm-s)}, P_m = 13.2\%\}$ 66

6.6. Sample Frequency Responses. 67

6.7. A single pair of Helmholtz Coils [3] 68

6.8. Experimental setup of three orthogonally positioned pairs of Helmholtz coils . 69

6.9. Ramps from 1° to 10° used to test at various inclines. 70

6.10. Circuit schematic for the experimental setup 71

6.11. Experimental results of Big Foot stride length vs. Platform Slope. $\{\phi_m = 53°, \psi_m = 25°, P_L = 0.22 \text{ s}, t_{off} = 0.046 \text{ s}\}$. 72

6.12. Experimental results of Big Foot input frequency vs. Platform Slope. $\{\phi_m = 53°, \psi_m = 20°, P_m = 33.8\%, t_{off} = 0.046 \text{ s}, \beta = 0°\}$. 74

LIST OF TABLES

Table Page

4.1. Tube Model Parameters 39

ACKNOWLEDGMENTS

This project was supported by a contract from Lockheed Martin Aeronautics. We express our thanks to Mr. Necdet Yildirimer and Mr. Kenneth Sangston of the SMU Machine Shop for building and fitting various parts of MoRIS. We also are very grateful to Dr. Seth Orsborn and the Deason Innovation Gym for the tools and equipment necessary for completion of the prototypes.

Chapter 1

Introduction

1.1 Tube Inspections

Inspecting sophisticated fighter jets is an expensive process. To access the internals of the aircraft, significant disassembly is required. One cause of this laborous process is the lack of development of in-pipe inspection tools. MoRIS offers a solution.

Pipe inspection has a long history as an engineering challenge. From the point of a view of a bystander, locomotion inside a pipe seems to be very simple. There is a single path where one can send a borescope camera down. In fighter jets, this is the current method of inspecting tubes. However, this method has several limitations.

A single borescope is very effective as a quick and easy tool for inspection. Its simplicity, however, becomes its weakness. It has no structure around it for more detailed and controlled measurements. It has a semi-rigid cable behind to push it through. This is good for getting the borescope down a short tube. In fact, the tube networks in fighter jets are in small sections. So, aeronautical manufacturing companies are able to get away with inspecting section by section separately. But, this can only go so far.

Inspection of tube networks has become more common in the manufacturing of modern aircraft. This poses significant limitations in using borescopes for inspection. First, the only means of moving a borescope through a tube network is by pushing the cable from outside. This means that the two static forces that the borescope experiences in the tube; gravity and contact forces, severely restrict the distance the borescope can be inserted into the network. A specific number cannot be given as to the maximum insertion distance for borescopes in all situations, and manufacturers cannot pre-identify the set of tasks that can be achieved by use of a borescope. There are many factors involved. An obvious limit to insertion distance is friction. The greater the friction, the greater the resistance

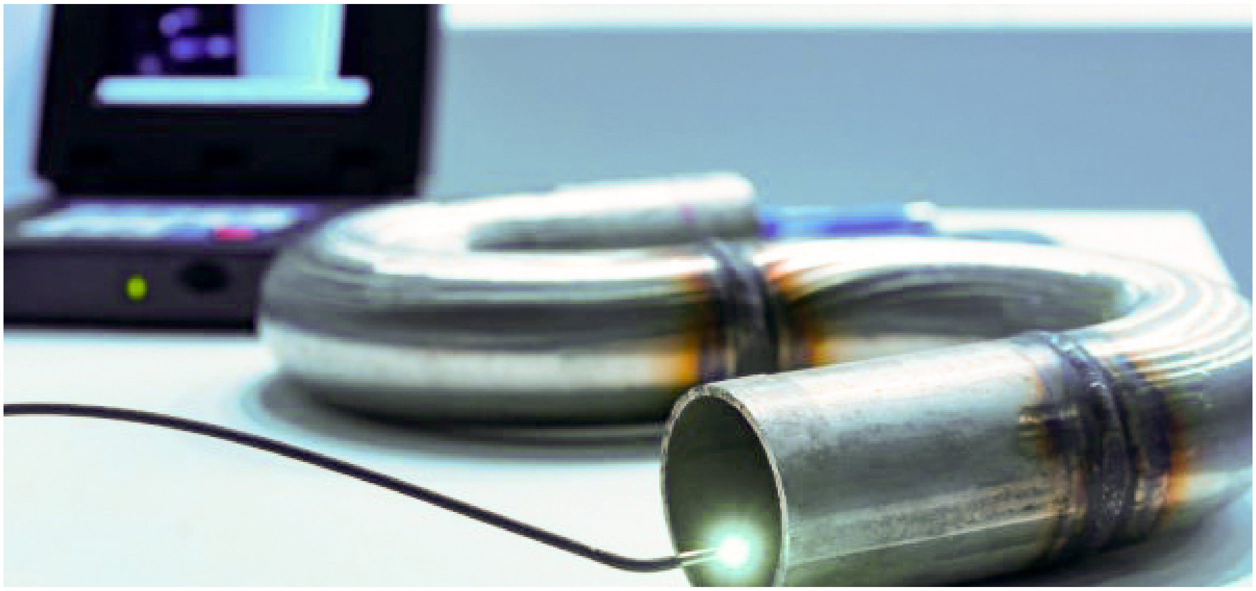

Figure 1.1: Pure borescope tube inspection example [1].

there is for insertion, and consequently a shorter maximum distance. A less obvious limit is the interaction a borescope's surfaces have with the tube network surfaces. Friction is dependent on the normal force between the surfaces. Cable Pulling Force equations have been developed by civil engineers [4]. These equations have not been applied to borescopes because borescopes are pushed, not pulled. However, the concept of friction in different pipe networks can be complex. For any pipe bend, except for perfectly horizontal and vertical sections, a numerical solver must be used. Thus, the inspection crew often have to go through a lengthy process just to find out whether the borescope is a suitable device for the task. Therefore, the effectiveness of borescopes can only be found through trial-and-error. This lack of predictability is expensive. Friction is just one aspect effecting maximum insertion distance for a borescope.

Additional factors dictating maximum insertion distance are as follows. The borescope cable has a certain degree of stiffness. Manufacturers fine-tune this stiffness such that, as the borescope is pushed in the pipe, the cable does not buckle. This stiffness, however, limits maximum insertion distance by increasing friction around bends. In the Cable Pulling Force equations, cable stiffness is ignored. For standard flexible cables, pulled around large bends, this can be ignored. But, borescopes are designed to be stiff, which further complicates the

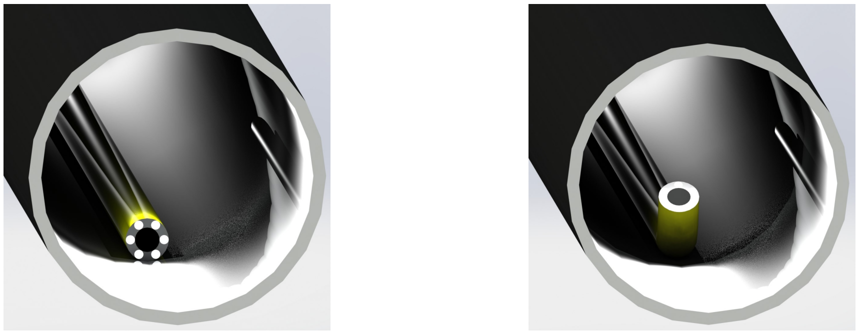

(a) Straight Tip (b) Flexed Tip

Figure 1.2: Convential borescope flexion

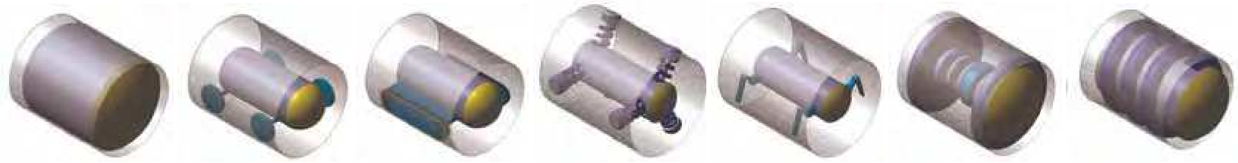

(a) PIG (b) Wheeled (c) Caterpillar (d) Wall-Press (e) Legged (f) Inchworm (g) Helical

Figure 1.3: In-pipe locomotion modalities [2]

analysis. Few more detailed factors affecting maximum insertion distance include: pipe and borescope materials, borescope camera orientation, environmental vibrations, experience of operator, etc.

The second design limitation is the control of the borescope's tip. Industrial borescopes have a camera end that flexes slightly for viewing the pipe walls at different angles (see Fig. 1.2). This movable tip has a limited turning motion. Often, the tip cannot be used to inspect completely around a tube bend. The limited motion also poses problems when inspecting welds. Finally, when inspecting a pre-assembled tube network, the tip lies on the bottom of the tube network. In small tube segments, the inspector can manually manipulate the tube to get a full inspection. But, in a tube network in a fully assembled jet, manual manipulation is not possible. This results in an incomplete inspection.

Figure 1.3, which is from Choi [2], shows different forms of In-Pipe Locomotion. The practical use of in-pipe inspection robots began with the inspection of large oil and gas pipelines [5]. Called pigs, these robots are large robots with many sensors and actuators. Pigs are sent deep into pipelines for the inspection of long networks. In [2], Fig. 1.3a shows the basic shape of a pig. A pig is simply a set of sensors and electronics pneumatically sealed in the pipe. The operator uses gas pressure to push the pig down the pipe. This method is effective only for consistently shaped pipelines to maintain the seal. Therefore, for the winding tube networks of fighter jets, a pig would not be effective.

The second locomotion mode is a simple wheeled robot, shown in Fig. 1.3b. Extensive research has been done in this area [6–21]. In Fig. 1.3c are treaded robots [22]. And, in Fig. 1.3d are robots that use legs to press against pipe walls for traction [15]. Also, Fig. 1.3e are legged robots for complicated paths [23–26]. Next, Fig. 1.3f are worm robots that expand and contract through pipes [27–40]. Finally, Fig. 1.3g are helical drive robots [41–43]. Many of these robots are combinations of the different types of locomotion.

A specific combination of locomotion modes is the focus of MoRIS's design. The design is a combination of the wheel, wall-press, and inchworm modes. MoRIS uses wheels to drive through the tube network. Attached to these wheels is a suspension that presses the wheels against the tube walls. Finally, MoRIS is broken up into segments like an inchworm. Several previous designs helped inspire the design of MoRIS. Kakogawa [44] creates an unusual design in which the front wheels are placed at an angle with respect to the pipe centerline. Then, the front wheels are rotated to created a helical motion to navigate the pipe. MoRIS's suspension design draw's from Kakogawa's robot. The suspension increases the normal force between the wheels and the tube wall. Kakogawa uses the normal force to enable the screw drive action. Whereas, MoRIS uses it to increase traction. Kakogawa also creates a caterpillar design [45]. The Kakogawa's caterpillar design uses an active suspension to create normal force between the treads and the pipe walls. MoRIS uses a passive suspension. Finally, Kakogawa explores a snake design called AIRo [46]. This design uses active joints to morph the geometry of AIRo to the pipe's geometry. MoRIS does not need such a complicated control scheme.

Bocko [47] creates a "micromachine" that is similar to MoRIS's Vertebrae. The machine uses the same combination of locomotion designs. Unfortunately, the performance of Bocko's design is undocumented and can not be compared.

MoRIS is a modular robotic inspection system for aircraft tube networks. It can travel deep into tube networks, and inspect around bends and welds. This paper introduces this system. First, the purpose and inspiration of MoRIS is presented. Next, the design of MoRIS is revealed and analyzed. Subsequently, the control scheme is given. In addition, we present the procedure to develop localization process. Finally, an actual prototype is developed at SMU and was tested at Lockheed Martin facilities.

1.2 Millimeter Bipedal Locomotion

Bipedal locomotion research pushes the limits of robotics miniaturization, efficient locomotion, and rapid prototyping. Passive locomotion for bipedal walkers have brought advances in efficiency. There are many different types of walking robot locomotion modes. The dynamics modeled for bipedal robots begin with simplifications from the real world to more complex models with impact dynamics. In this paper, we use Helmholtz coils to control a semi-passive walker. The semi-passive walker presented provides a novel means of locomotion.

A significant of work in bipedal design, modeling, stability analysis, and control was pioneered by Hurmuzlu. Moskowitz and Hurmuzlu [48] created the first stability analysis of bipedal locomotion. They found that a relationship could be derived between the leg angles at each foot impact. They [49, 50] also advanced the analysis by the use of Poincaré Maps and Floquet multipliers. Next, Hurmuzlu [51, 52] developed a characterization of the gait patterns of bipedal locomotion and objective functions, and generalized the stability analysis for any designed. Hurmuzlu and Change [53] proceeded to derive a sliding mode controller for bipedal robots. This controller eliminated the reaching phase, provided means to predict motion and tracking errors, and allowed for trajectory planning of the joint and/or Cartesian spaces. Hurmuzlu and Basdogan [54] developed quantitative measures of dynamic stability of human locomotion. Hurmuzlu, Basdogan, and Carollo [55] applied this stability analysis to the locomotion of actual humans. Hurmuzlu, Basdogan, and Stoianovici [56] applied it to polio patients. Borzova and Hurmuzlu [57] investigate a five-link passive walker to produce three distinct locomotion limit cycles. Hurmuzlu, Génot, and Brogliato [58] surveyed the framework of stability and control of bipedal systems with unilateral constraints. Tavakoli and Hurmuzlu [59, 60] investigate the control of bipedal robots by the hybrid combination of an impulsive and continuous controller. This controller is similar to the control scheme of Big Foot.

Passive dynamics involves motion driven by gravity. Tavakoli and Hurmuzlu [60–62] also established a family of gravity powered locomotors using a variety of different types of body members and corresponding control methods. Based on walking toys [63] that would "waddle" down a ramp and inspired by the mathematics of McMahon and Mochon [64], McGeer [65] designed a rigid, knee-less passive bipedal robot that could walk down an incline with a "compass-like" gait. McGeer analyzed the work using linearized mathematical models, after which Goswami et al. [66] analyzed using non-linear models to be more accurate to the complex, interconnected nature of walking [67]. Garcia et al. [68] did significant research on the efficiency, speed, and stability of passive walkers and proposed that a passive walker could achieve zero energy consumption when given the correct initial conditions such that the end of the swing phase is nearly identical to the initial conditions. Following Kuo's work [69], which investigated the stabilization of McGeer's [70] passive walker in 3D, Collins et al. [71] enhanced upon the McGeer design by incorporating knees, adjusting the foot design to be more laterally stable, adding softer heels with springs to reduce instability upon heel strike, adding counter-swinging arms to reduce yaw induced by the legs, and adding lateral-swinging arms to address the side-to-side lean, thus achieving true 3D passive walking. Spong and Bullo [72] used controlled symmetries to generalize the bipedal walker model to n degrees-of-freedom (DOF) in 3D space, making the addition of knees, arms, etc. easier.

Miniature walking robots have been produced using soft and flexible actuators. Ijaz et al. [73] developed a simple walking robot that uses embedded magnets to flex the robot's abdomen to produce locomotion. Baisch et al. [74–77] created a family of walking robots called the Harvard Ambulatory MicroRobot (HAMR). These microrobots use custom machined piezoelectric boards that flex with a voltage applied. HAMR was inspired by cockroaches. Miniaturizing actuators for rigid body robots is difficult. Microrobotics and Micromechanical Systems [78] provides ideas for miniaturizing actuators, but for actuators that perform like electric motors, Often these actuators use compliant surfaces to allow motion [79, 80].

The full extent of these "muscle-like" walking robots can be seen in the LCE-microrobots from Hao et al. [81]. These microrobots are basically a single torsional muscle, whose design has no other control or means of locomotion. With rigid actuation, Islam et al. [82] developed a minimally actuated, rigid bipedal walker, including five 3D printed rigid bodies and a single actuator per leg. Each actuator is controlled via an open-loop sinusoidal profile, thereby eliminating the need for feedback. They also found advanced stability through non-concentric curvature in the design of the feet, allowing turning and walking on level surfaces while achieving a reasonably small height of 15cm.

Modeling bipedal walking is complex due to the hybrid nature of the discrete (stance) phase and continuous (swing) phase of the motion. The balance and control necessary for bipedal walking beyond the "compass gait" is often interpreted as balancing an inverted pendulum. This primarily leads to the spring loaded inverted pendulum (SLIP) model [83] in conjunction with the zero-moment point (ZMP) [84,85]. The SLIP model assumes a point mass at the hip with mass-less spring legs that make a single contact with the surface. The ZMP approach, in contrast, uses a flat foot to aid in prediction of the stability point [86]. Takano et al. [86] developed a model that realizes the natural sequence of contact points that occur in stepping (i.e, from heel to sole to toe). Pratt et al. [87] advanced upon the inverted pendulum model by changing the hip from a point mass to a "fly-wheel", thereby accounting for angular momentum stored in the "fly-wheel" to generate a set of capture points the robot can step to fully recover following an external force or disruption. Pelit et al. [88] developed an improved spring loaded inverted pendulum model with swing leg (SLIP-SL), advancing the SLIP model to include the dynamics of the swing leg, using stiffness as parameters to define cyclic gaits. Another degree of complexity in analysis of bipedal walking arises from the impact dynamics when the swing leg makes first contact with the ground. Often this collision is assumed to be inelastic. Whittaker [89] offers solutions to many friction-involved collisions using the coefficient of restitution and coefficient of friction as means to describe the magnitude of an impulsive, instantaneous collision. While fundamental, given certain initial conditions, Whittaker's method breaks conservation of energy laws [90]. Keller [91] proposed analysis that assumes a finite impact time rather than instantaneous, thereby accounting for constant-direction slipping during contact. Keller's work, however, necessitates integration of the equations of motion. Brach [92] accounts for direction change in slipping while also achieving algebraic impact equations by considering tangential impulse to be a fraction of the normal impulse. However, Brach's work assumes no contact prior to collision and the point of the collision as the only point of potential separation. Hurmuzlu and Chang [93] offer significant investigation on impact dynamics for bipeds as a multi-link system, thereby accounting for the second potential separation point of the stance leg. Hurmuzlu and Chang also classify the motion as either single contact if one point of separation occurs or double contact if neither point separates. Experimental results show that Big Foot's feet do not slip during the impacts. Also, in modelling, double contact is ignored because the switching of stance is practically instantaneous. Ruilong et al. [94] analyzed the effect of joint member elasticity in locomotion dynamics.

The use of electromagnetic fields as a form of control allows untethered, low-power actuation of robots. Yesin et al. [95] used a combination of Helmholtz coils and Maxwell coils to control cubed microrobots in one-dimension, followed by Choi et al. [96] in two-dimensions and eventually Jeong et al. [97] in three-dimensions. Kim et al. [98] reduced the number of coils needed for two-dimensional control by using a pair of coils similar to Helmholtz coils that could receive independently controlled current. In addition, Mahoney et al. [99] explored various magnetic methods of microrobots with helical screw propulsion and rolling locomotion. Li et al. [100] created a completely rigid, two-legged magnetic microrobot that uses periodic magnetic fields to induce pivot walking to indirectly manipulate cell aggregates, though it is limited to this one mode of locomotion. While not bipedal, Khatib et al. [101] developed a rectangular millirobot capable of various modes of locomotion, including pivot-walking, tapping, and tumbling, with high maneuverability in tight spaces by capitalizing purely on the torque created by the magnetic field. They furthered their impact with "stag beetle" and "carbot" designs for increased application. A special novelty of magnetic actuation is that these robots are powered externally, but also untethered. This removes the need for power storage (batteries, compressed air tanks, hydraulic and pnuematic lines, and any other traditional power source.) or electronics (sensors and controllers). This allows for unheard-of miniaturization. All that is required to power the robots on the body itself is a magnet. This opens the door for rapid prototyping as simpler designs allow more ready solutions.

In this paper we present the first magnetically actuated bipedal walking robot. This robot is also the world's smallest bipedal robot. The robot weighs 0.3g and is 9mm tall. The robot has been called Big Foot accordingly.

The control of Big Foot is accomplished by simply placing a magnet in the abdomen of the standard passive walker. Next, a magnetic field applies a moment on the foot-lifting-dynamics to stabilize the gait. Traditional walkers use their natural dynamics to lift the feet. The success of locomotion is very inconsistent in these fully passive walks because of unmodeled dynamics and inconsistent initial conditions. The simple placement of a magnet solves this problem.

This research advances engineering in several ways. First, Big Foot offers a glimpse at the future of millirobotics. Second, Big Foot shows the potential of using magnetic actuation for rapid prototyping. Big Foot was manufactured in a day. Third, Big Foot reveals the undiscovered opportunity of magnetic actuation to produce new modes of locomotion and machine design.

This preliminary introduction to impulsively actuated bipedal walkers begins with a description of how they are made. Next, the dynamics are presented, including the impact mechanics. The Experimental setup is explained. Finally, the experimental and simulated results is presented with analysis. All of this is wrapped up with a discussion of the significance of Big Foot and future work.

Chapter 2

Problem Statement of Tube Inspections

Aircraft use tube networks as conduits to transfer assets among different compartments. Possible assets include: fuel, electrical power and controls, hydraulics, pilot oxygen, and more. The proper functioning of these networks is critical to the operation and survivability of the plane.

A unique aspect of fighter jet tube networks is the use of distinct interchangeable segments. Aircraft tube networks are designed for repairability and ease of disassembly. Consequentially, the tube networks have distinct joints between relatively short sections.

Furthermore, with the high pressures and volumetric flow rates in modern aircraft, the slightest defect in tube bend quality can have major effects on dynamics, and possibly cause catastrophic results. Thus, to ensure dimensional consistency, aircraft tube network bends are mandrel bent. Mandrel bending is a manufacturing process that preserves the inner diameter of a tube through its bends [102]. It is important to mention that mandrel bends are planar. This means that the bends are toroidal and there will be no helical bends in an aircraft tubing.Often the aforementioned tubes need to be inspected without disassembly. Thus, inspection robots are used. The inspection robots must either continually with a user or before and after operation [103]. Since most tubes in aircraft are metallic, real-time wireless communication is not a viable option. Experimental testing showed that a 2.5 GHz Wi-Fi signal disappears after 6 inches into a stainless steel tube. The range will change with different metals, but not significantly. The other option is wired communication, which is the solution used for MoRIS.

Having described the operating environment, now we present the detailed specifications for testing of the prototype. First, the nominal tube size is BWG 1-1/2" diameter 16-gauge tube. The inner diameter is 1.370" (34.8 mm) and wall thickness 0.065" (1.6 mm). The bends have a minimum centerline radius of 3" (76 mm). Second, MoRIS must be able to travel in the tube network in all orientations, including: Up, Down, Horizontal, and Sloped. Third, MoRIS must be able to inspect the entire inner surface of the tube network. Fourth, the maximum distance traveled must be as far as possible.

2.1 Tube Network Model

We modeled the aircraft tube network as a succession of bent and straight segments. The bent sections are considered toroidal sectors with the torus center, C_j, radius of the centerline, R_j, the sector angle, β_j, and tube radius, r as shown in Fig. 2.1. The straight segments have length, l_j. Thus, the tube network is defined piece-wise:

$$\begin{aligned}
\boldsymbol{r_{P/O}} &= \boldsymbol{r_{O_j/O}} + \begin{cases} R_j(\boldsymbol{I} + \boldsymbol{R}_{\boldsymbol{\hat{e}_{bj}}}(\frac{s_j}{R_j})) \cdot \boldsymbol{\hat{e}_{nj}} & \text{Bend} \\ s_j \boldsymbol{\hat{e}_{tj}} & \text{Straight} \end{cases} \\
\boldsymbol{r_{Q/O}} &= \boldsymbol{r_{P/O}} + \rho \, \boldsymbol{R}_{\boldsymbol{\hat{e}_{tj}}}(\gamma) \boldsymbol{R}_{\boldsymbol{\hat{e}_{bj}}}(\frac{s_j}{R_j}) \cdot \boldsymbol{\hat{e}_{nj}}
\end{aligned} \tag{2.1}$$

where, $\boldsymbol{r_{P/O}}$ is the position vector of point P on the centerline, $\boldsymbol{r_{O_j/O}}$ is the position vector of the starting point for centerline of the jth tube section, and $\{\boldsymbol{\hat{e}_{tj}}, \boldsymbol{\hat{e}_{nj}}, \boldsymbol{\hat{e}_{bj}}\}$ are the unit vectors of the path variable (Frenet) coordinate system with origin O_j. Point Q is the center of mass of the robot, s_j is the arc length of the tube section centerline to point P, ρ is the radial offset of point Q, and γ is the angle between the normal direction at point P and the position vector $\boldsymbol{r_{P/Q}}$. $\boldsymbol{R}_{\boldsymbol{\hat{e}_{bj}}}(\frac{s_j}{R_j})$ is a simple rotation about $\hat{e}_{bj}$ and $\boldsymbol{R}_{\boldsymbol{\hat{e}_{tj}}}(\gamma)$ is a simple rotation about $\hat{e}_{tj}$. This model can be applied recursively for all tube network segments:

$$\boldsymbol{r_{O_{j+1}/O}} = \boldsymbol{r_{O_j/O}} + \begin{cases} R_j(\boldsymbol{I} + \boldsymbol{R}_{\boldsymbol{\hat{e}_{bj}}}(\beta_j)) \cdot \boldsymbol{\hat{e}_{nj}} & \text{Bend} \\ l_j \boldsymbol{\hat{e}_{tj}} & \text{Straight.} \end{cases} \tag{2.2}$$

2.2 Description of MoRIS

MoRIS encompasses four main assemblies (see Fig. 2.2 and 2.11): Locomotion Vertebra, Camera Vertebra, tether, and Base Station.

The operation of MoRIS starts at the Base Station. The user controls and connects with MoRIS at the Base Station. The Base Station connects with the Vertebrae through

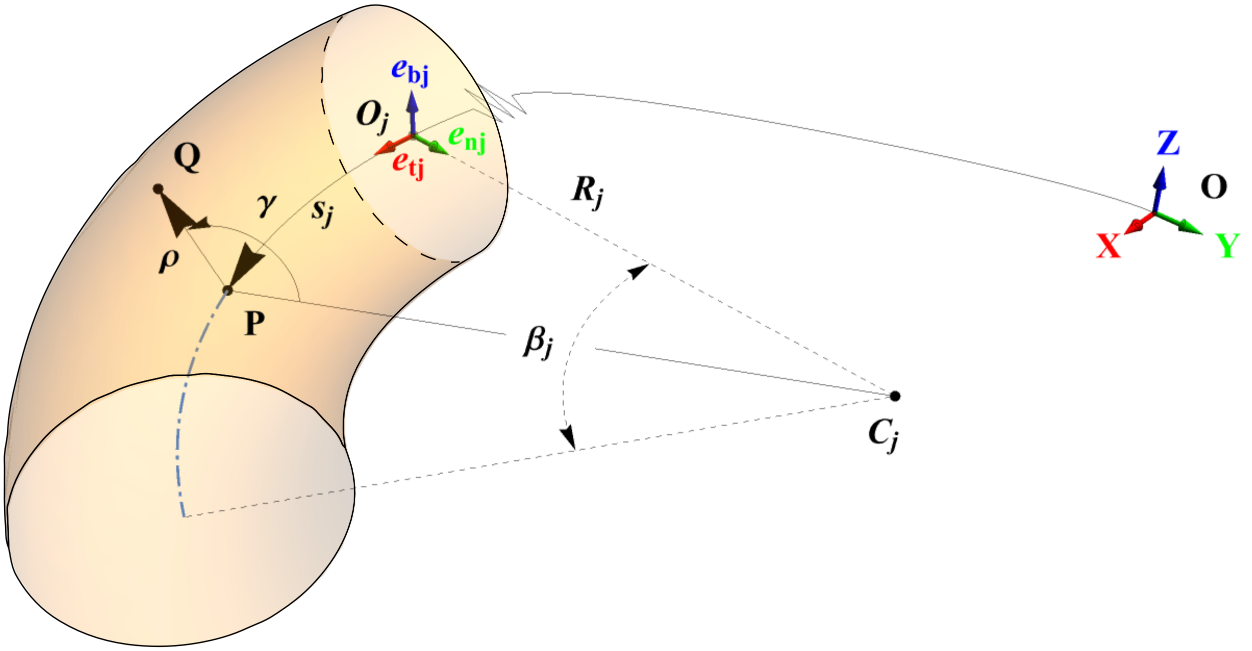
e_{bj}
O_j
e_{nj}
e_{tj}
Q
γ
s_j
R_j
ρ
P
β_j
C_j
Z
O
X
Y

Figure 2.1: Tube section with geometric parameters, $\{R_j, \beta_j, C_j\}$ and tube network coordinate system: $\{s, \gamma, \rho\}$

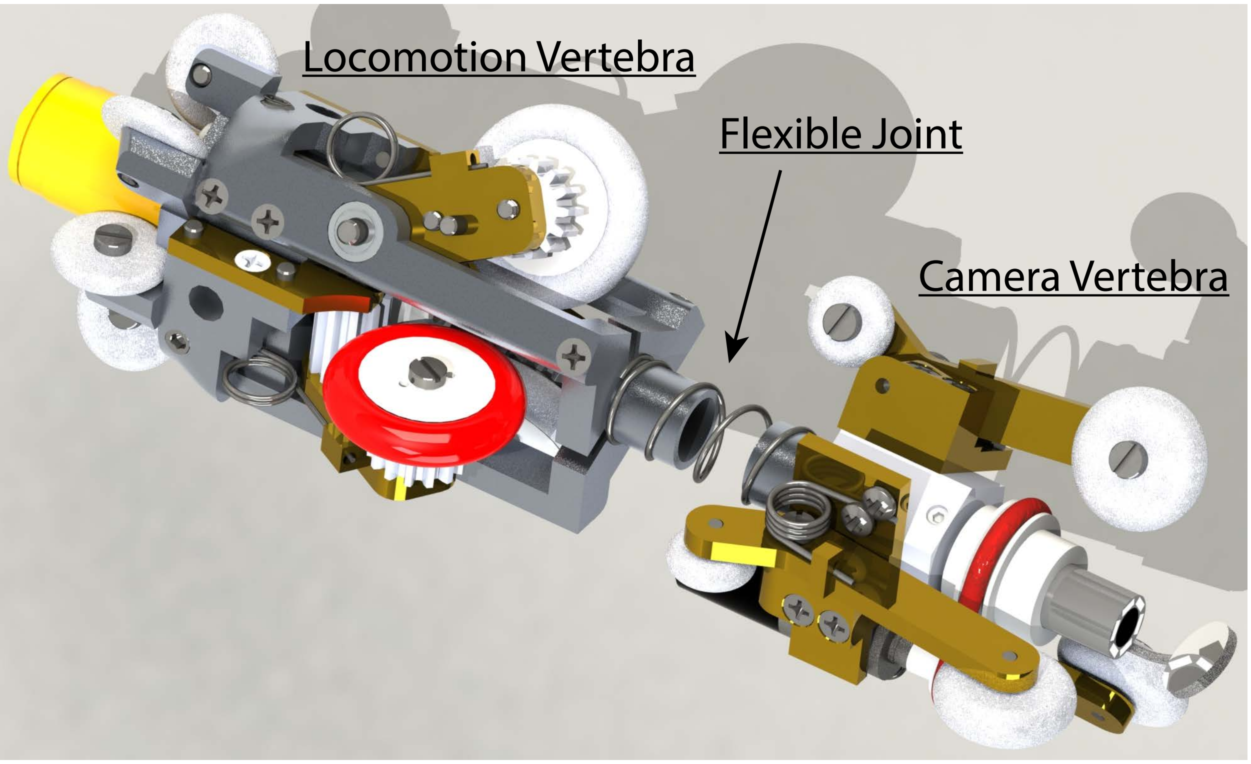
Locomotion Vertebra
Flexible Joint
Camera Vertebra

Figure 2.2: Vertebrae

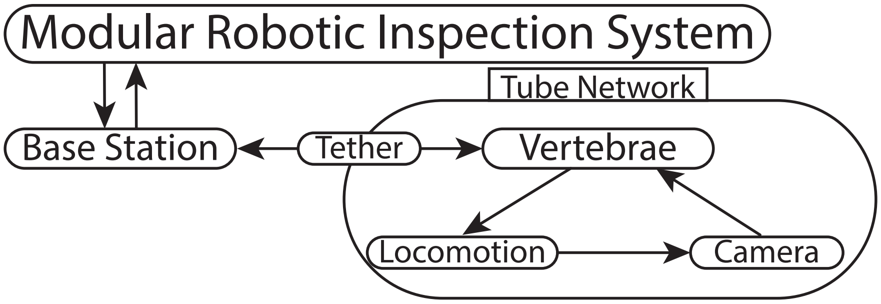

Figure 2.3: MoRIS design structure

the tether. The Vertebrae are composed of a Locomotion and a Camera Vertebra. The Locomotion Vertebra provides the power to drive MoRIS through the tube network. The Camera Vertebra holds the camera and potentially other instruments for inspection.

2.3 Locomotion Vertebra

In order for an inspection camera to be moved in a tube network, a Locomotion Vertebra was designed. The Locomotion Vertebra converts stepper motor power signals from the tether to kinetic power. The design focus of this unit is maximizing the drive torque while keeping the design reasonably compact.

2.3.1 Transmission

The power transmission starts at a 10 mm stepper motor with a 16:1 gearhead (Faulhaber, Schönaich, Germany). The motor drives a worm gear combination that amplifies the motor torque by 14. The transmission, starting at the gear train, is shown in Fig. 2.5. The theoretical output torque is 314 mNm. The actual output torque is much lower as there are high frictional losses that will be discussed later. At the end, a wheel has been coupled to the final gear through a 1/32 inch dowel pin. In the Locomotion Vertebra, there are three transmissions orientated at 120° with respect to each other. In two transmissions, the wheels are made from acetal. However, the third transmission has a wheel with a soft silicone O-Ring rim (Red). The red wheel provides the majority of traction and is called the tractive wheel. The purely acetal wheels are required to allow the wheels to slip due to misalignments. The suspension of the Locomotion Vertebra was incorporated into the transmission to save space.

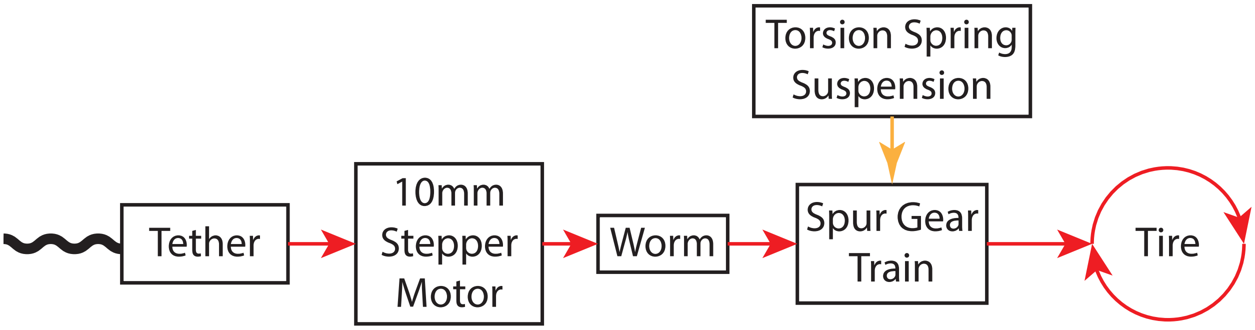
Torsion Spring Suspension
Tether
10mm Stepper Motor
Worm
Spur Gear Train
Tire

Figure 2.4: Locomotion Vertebra design structure

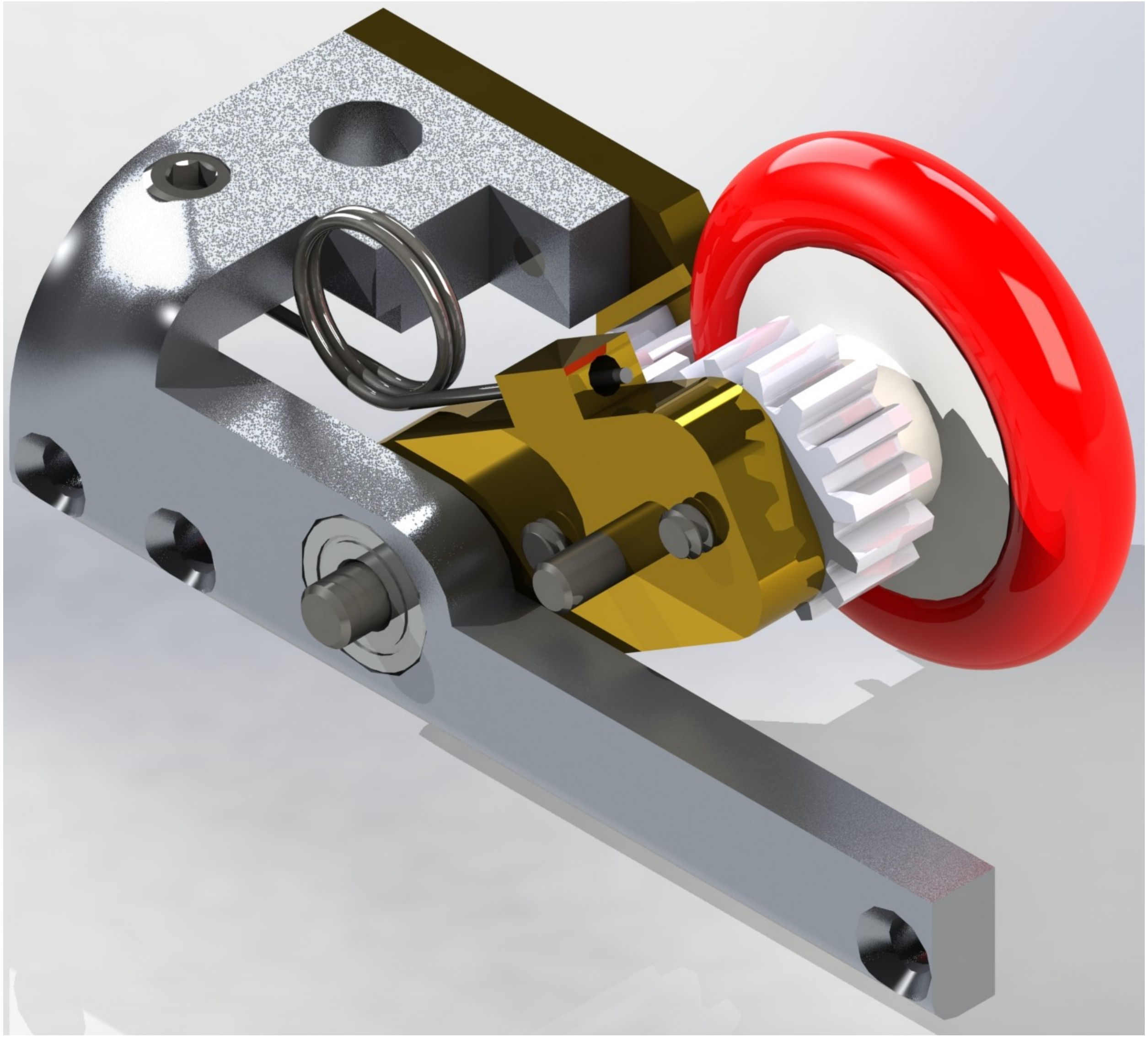

Figure 2.5: Locomotion Vertebra transmission

2.3.2 Suspension

The shape of the tube networks change. The tube diameter can change. There are bends in the network that result in different positioning and geometries of the Vertebrae in the tube bends versus a straight section. Such differences require Vertebrae that can flex. MoRIS's solution is a torsional suspension. A brass arm is mounted on a dowel pin that acts as a shaft for the worm gear. There is a high reaction force between the arm and the shaft. A ball bearing is required to reduce friction between these. A 90° angle, left-hand wound, 0.204 inch OD music-wire steel torsional spring was selected. The spring has a maximum torque of 0.28 in-lbs. It is secured between the transmission and the Locomotion Vertebra body with a set screw. The spring connects with the suspension arm through a slip-hole. As the suspension is compressed, the spring slips in the hole. This results in a dynamic geometry between the spring and the arm.

There are two main advantages of this design. First, the equal forces of the three suspensions keep the Vertebra centered in the tube. Sometimes there is debris in the tube. The suspension keeps the body of the Vertebra away from the tube wall, where the debris is. This positioning of the Vertebra minimizes the likelihood of interference that can prevent robot operation.

The second advantage of the suspension is the creation of tube surface reaction forces. A tube is a unique locomotion surface because the ground wraps around itself. This allows the suspension to push in all directions, instead of just down. This is exploited by varying the stiffness (k) of the torsional spring and the length (L_A) of the suspension arm to optimize the normal force between the wheels and their contact points for the range of deflections (δ) in operation. The optimal set of parameters depend on the required normal force for traction and internal transmission friction. The origin of this design decision was the requirement for the Vertebra to have the ability to climb vertical tube sections while dragging the tether and pushing the Camera Vertebra.

Within the design and prototyping process, the radial load exerting on the suspension arm ball bearing needs to be checked to be less than the ball bearing's maximum. In this analysis the Vertebra is assumed to be static because dynamic forces are insignificant. The radial load can be found from the normal force. Figure 2.6 shows a free body diagram of

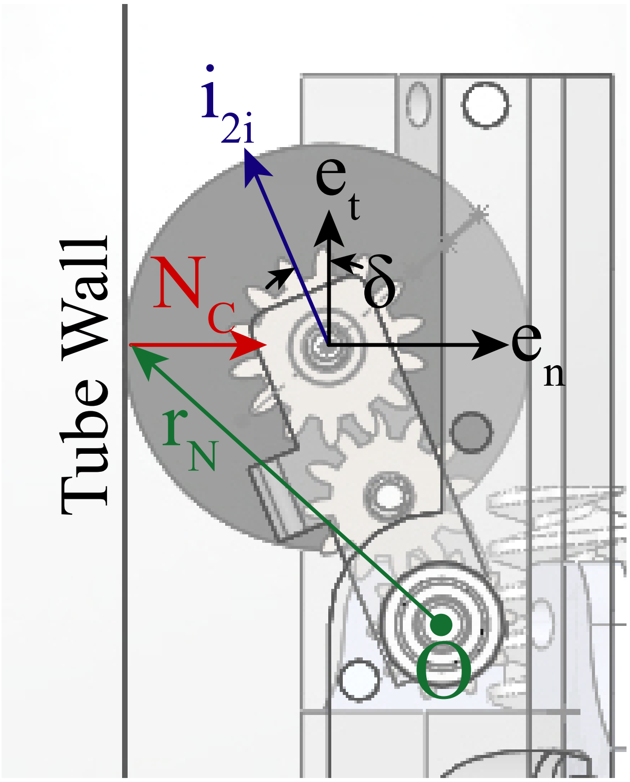

Figure 2.6: Suspension system arm free body diagram

one suspension system without the reaction forces in the bearing.

A sum of the moments about one of the suspension's arms ball bearing, point O_{2i}, can be evaluated as:

$$\Sigma M_{O_{2i}} = (\boldsymbol{r_{N_i}} \times (N_{C_i}\ \boldsymbol{\hat{e}_n})) \cdot \boldsymbol{\hat{e}_b} + k(\delta_0 - \delta_i) = 0 \tag{2.3}$$

where, $\boldsymbol{r_{N_i}}$ is the position vector from the ball bearing to the contact point between the tire and the tube wall, N_{C_i} is the normal force at contact, k is the torsional spring stiffness, δ_i is the suspension arm angle, and δ_0 is the angle corresponding to zero spring deflection.

Solving for the normal force between the tube wall and the suspension system:

$$N_{C_i} = \frac{k}{L\cos(\delta_i)}(\delta_0 - \delta_i). \tag{2.4}$$

The normal force, shown in Fig. 2.7, can be used to calculate the maximum traction

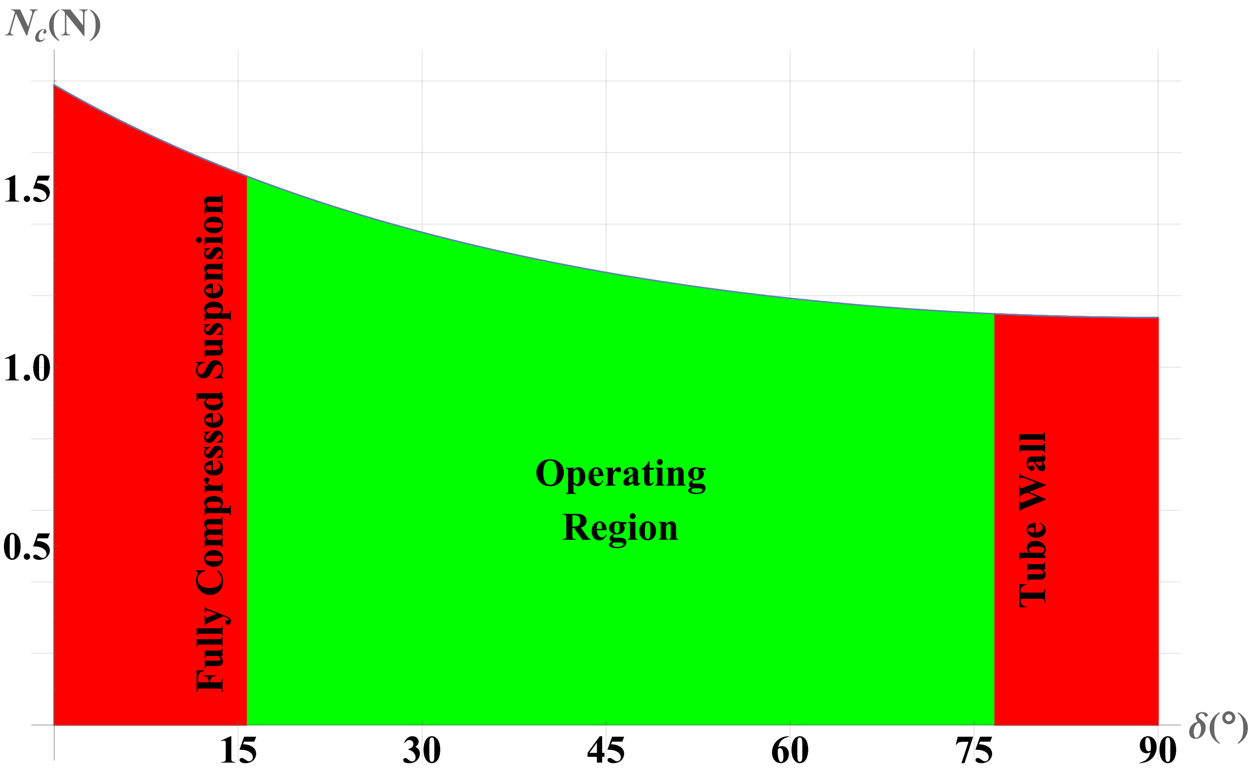

Figure 2.7: Suspension normal force vs. deflection

the Vertebra has in a tube, if the coefficient of friction is known. This also can be used to identify what largest tube size the Vertebrae can perform in, to choose a suitable bearing in the design process, and to estimate the effect the normal force has on internal friction of the transmission. Finally, as the Vertebrae travel through different tube network geometries, the suspension compresses and decompresses. The motor must provide the torque required to compress the suspensions. This analysis would be used to calculate the drag force.

2.3.3 Hex Roller

A passive component, called the Hex Roller (see Fig. 2.8), was added to prevent the back of the body of the Locomotion Vertebra from colliding with debris or the tube wall. As will be shown later, the Hex Roller is essential for operation because the Vertebra's orientation in the tube has an unstable static equilibrium when aligned with the centerline. Thus, in standard operation, the hex roller can be in contact with the tube wall and be involved in the locomotion.

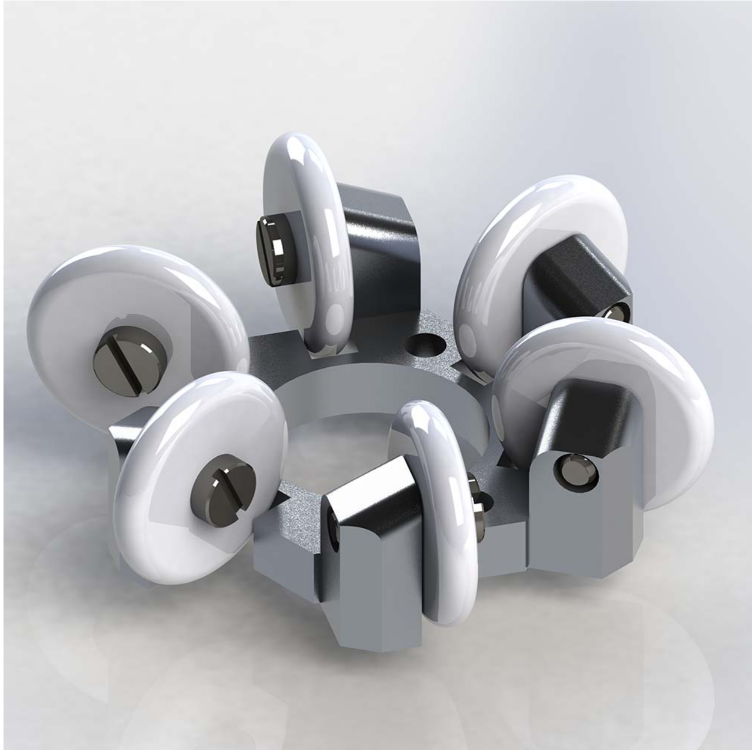

Figure 2.8: Hex Roller design

2.3.4 Camera Vertebra

Another functional Vertebra is the Camera Vertebra. It carries a high resolution camera and a mirror assembly. The purpose of the Camera Vertebra is to perform the inspection of defects and detect debris. The Camera Vertebra also has the room and potential for incorporation of additional inspection tools.

The Camera Vertebra has a suspension similar to that of the Locomotion Vertebra, as seen in Fig. 2.9. This cantilever suspension has a lighter spring than the Camera Vertebra's suspension. Its purpose is to center the camera in the tube and mitigate debris interference. MoRIS inspection camera is kept approximately centered in the tube. This is a competitive advantage compared to the conventional inspection borescopes, where the camera advances in contact with the tube's inner surface. Thus, the MoRIS camera shows the entire tube section at once and at any orientation.

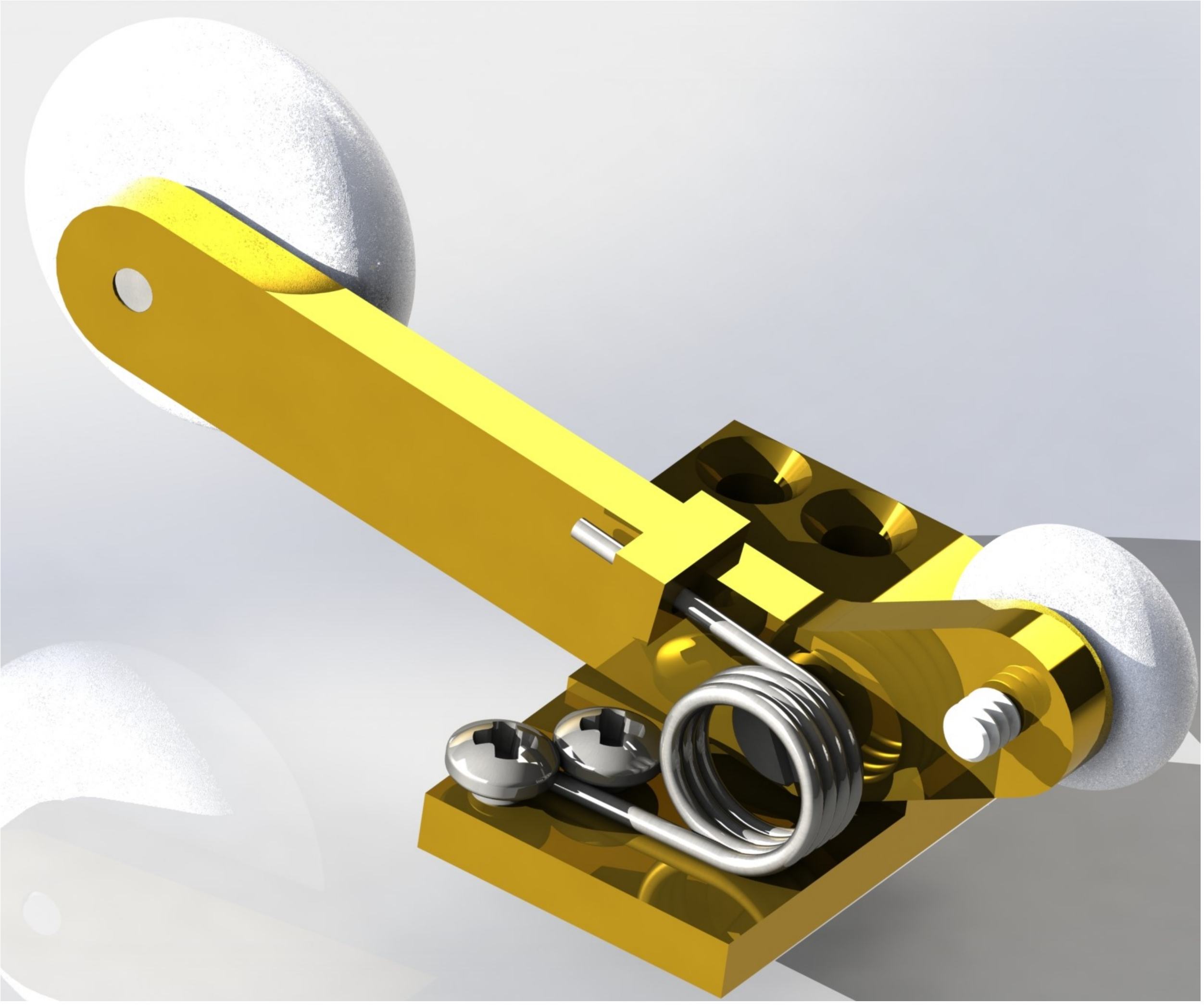

Figure 2.9: Camera Vertebra suspension

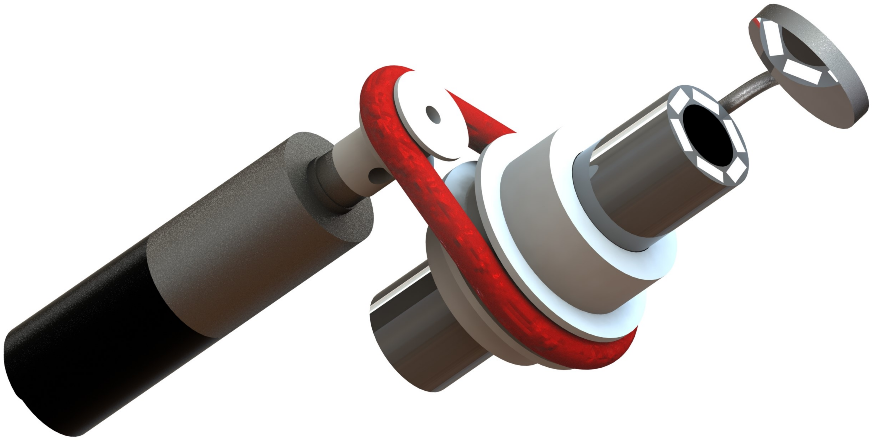

Figure 2.10: Mirror mechanism

2.3.5 Mirror Mechanism

In the current inspection method, borescopes cannot look around sharp bends and welds. MoRIS has a movable mirror mechanism included to accomplish this. The mechanism uses a 6 mm stepper motor (DM06202R008015+06/1 64:1+MG32 Faulhaber, Schönaich, Germany) to move the mirror. The motor drives a 64:1 gearhead, then through a 2.26:1 belt drive that employs a soft silicone O-Ring. The body of the camera is used as a shaft for rotation and the the belt and pulleys keeps the system securely attached to the Vertebra. The total gear ratio of 144:1 gives the motor a high torque of 36 mNm and a mirror roll angle resolution of 1.7568 arc seconds.

2.3.6 Tether

The tether consists of a set of wires that connects the Vertebrae to the Base Station. The wires provide both electrical and mechanical features. The wire provides:

1. Power to Stepper Motors

2. Power and Ground to the Camera and the Camera's LEDs.
3. USB Data Pair from the Camera to the user computer.

There are a total of 13 conductors in the tether. Due to the large number of conductors, the tether is also used as a mechanical tether. If the Vertebrae stall in the network, then the tether can be used to manually pull the Vertebrae out. The stepper motor cables are Teflon coated to reduce friction.

2.4 Base Station

A platform for the deployment of MoRIS is developed, (see Fig. 2.11). The main functions of MoRIS's Base Station are tether management, tether length measurement, user control and communication, and physical deployment. The Base Station is a vertical delrin board that holds the essential components for the operation of the Vertebrae. The Base Station is built with plastic to reduce weight, except for the lightweight extruded aluminum legs. A Dewalt battery powers the stepper motors. The battery is mounted on the back of the Base Station. A joystick is chosen for user control.

2.4.1 Winding Mechanism

The winding mechanism provides tether management and measurement.

As the user drives the Vertebrae in and out of the tubes, the tether extends and retracts. With an approximately 3 meter tether, a method of keeping the tether from getting tangled and nicely wound is needed. Inspiration was found in a fishing reel. In most tether reels, a slip ring is required to keep the tether from twisting. This problem was avoided by having a relatively large reel. The reel in MoRIS creates one twist for every 0.34 meters of tether. This low turn rate creates an insignificant twist as the Vertebrae are extended into the tube network. Another feature was the ease of extension of the tether. PVC sweeps were selected to guide the tether to the centerline of the mechanism. The sweeps reduce the friction of the tether at the bends, as it is pulled out of the Base Station. Also, for proper insertion of the tether into the tube network, the entrance of the tether into the Base Station should be stationary.

Second, the winding mechanism is used in localization. An encoder is attached to the

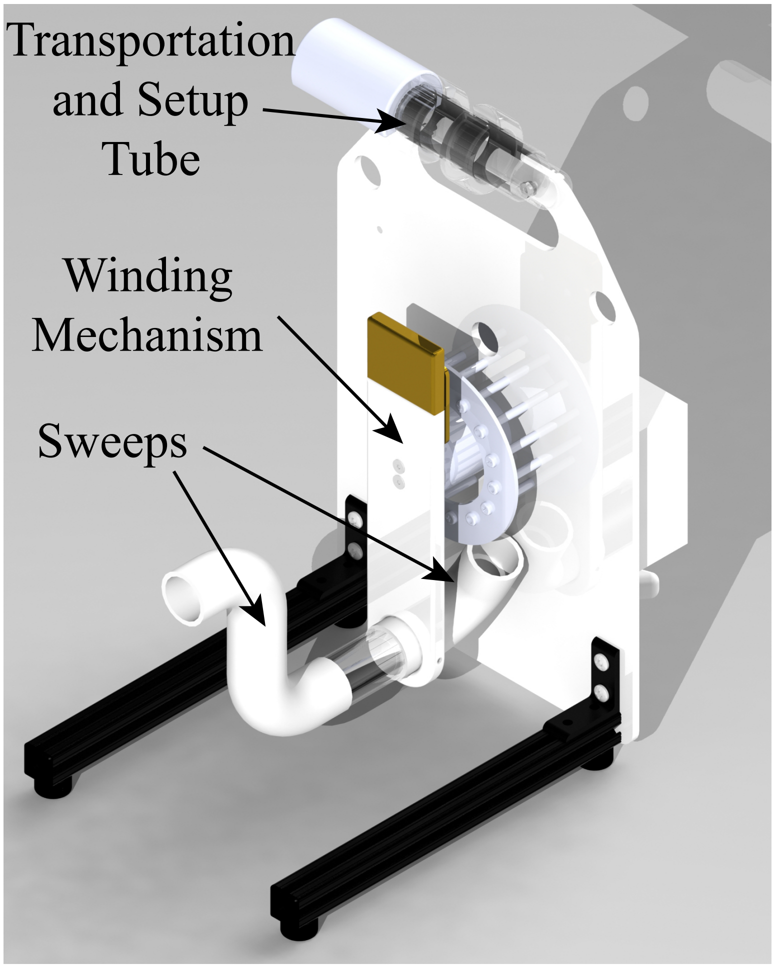
Transportation and Setup Tube
Winding Mechanism
Sweeps

Figure 2.11: Base Station

back of the winding mechanism to measure the number of rotations the tether has been fed out of the Base Station. The calculation of tether length is as follows:

$$L_T = n_E \tau_R \tag{2.5}$$

where, L_T is the length of the tether in the tube network, n_E is the number of counts the encoder has sensed, and τ_R is the counts-to-length multiplier found in calibration. Once the tether length has been acquired, the localization algorithm presented in section 4 will specify the tube network centerline position of the identified area of interest.

2.4.2 Custom PCB

A custom PCB is produced to hold the electrical components of the Base Station. Two TMC5072-BOB (Trinamic, Hamburg, Germany) stepper motor drivers are used for controlling the stepper motors in the Vertebrae. A microcontroller is used for communication and control. A E4T miniature optical kit encoder (US Digital, Vancouver, WA, USA) is used. The encoder has a 1000-count resolution. This provides a theoretical quadrature tether length resolution of 86 microns. The PCB provides connections for all external off-the-shelf electrical components.

2.4.3 Deployment

Finally, a simpler function of the Base Station is creating a physical structure for deployement in an aeronautical manufacturing facility. In the design presented here, extruded aluminum legs with rubber feet are used to hold the Base Station up. A mount on the top of the Base Station was 3D printed to create a soft grip for the user and as a mounting point for the storage tube. A 1.5" Polycarbonate tube is used to protect the Vertebrae in transportation and for setup. Attached to the storage tube is a coupler. First, the coupler attaches to the entrance to the tube network. Next, the storage tube is attached to the coupler. The storage tube provides a deployment platform. This allows the Camera Vertebra to inspect the entrance of the tube network and in effect places the Vertebrae in the tube network.

Chapter 3

Kinematic Analysis of MoRIS

3.1 Locomotion Vertebra Model

In order to understand the kinematics of the Locomotion Vertebra in the tube network, a multi-body diagram is shown in Fig 3.1. Five coordinate systems are chosen: the Frenet coordinate system presented in section 2.1; $\{\hat{\boldsymbol{x}}_{\boldsymbol{1}}, \hat{\boldsymbol{y}}_{\boldsymbol{1}}, \hat{\boldsymbol{z}}_{\boldsymbol{1}}\}$ is the body-fixed coordinate of the Vertebra's body; $\{\hat{\boldsymbol{x}}_{\boldsymbol{2i}}, \hat{\boldsymbol{y}}_{\boldsymbol{2i}}, \hat{\boldsymbol{z}}_{\boldsymbol{2i}}\}$ are body-fixed coordinates of the suspension system, with $\hat{\boldsymbol{x}}_{\boldsymbol{2i}}$ aligned along the respective suspension arm. To go from $\{\hat{\boldsymbol{e}}_{\boldsymbol{tj}}, \hat{\boldsymbol{e}}_{\boldsymbol{nj}}, \hat{\boldsymbol{e}}_{\boldsymbol{bj}}\}$ to $\{\hat{\boldsymbol{x}}_{\boldsymbol{1}}, \hat{\boldsymbol{y}}_{\boldsymbol{1}}, \hat{\boldsymbol{z}}_{\boldsymbol{1}}\}$, there is first a translation of s along $\hat{\boldsymbol{e}}_{\boldsymbol{tj}}$, then the simple rotation with angle γ about $\hat{\boldsymbol{e}}_{\boldsymbol{tj}}$, a translation of ρ along $\hat{\boldsymbol{e}}_{\boldsymbol{nj}}$, followed by the rotation transformations from the space fixed coordinates to the robot-body coordinate system with the vehicle attitude angles of yaw (ψ), pitch (θ), and roll (ϕ) in order. The transformation from the body fixed coordinates to each suspension coordinate is first a translation of L_{BF} along $\hat{\boldsymbol{i}}_{\boldsymbol{1}}$. Next, a rotation about $\hat{\boldsymbol{x}}_{\boldsymbol{1}}$ at $\{0°, 120°, -120°\}$, corresponding to each suspension system. This results in the intermediate coordinate system of $\{\hat{\boldsymbol{x}}_{\boldsymbol{1i}}, \hat{\boldsymbol{y}}_{\boldsymbol{1i}}, \hat{\boldsymbol{z}}_{\boldsymbol{1i}}\}$. Finally, the translation with L_O along $\hat{\boldsymbol{k}}_{\boldsymbol{1i}}$ is followed by the rotation about $\hat{\boldsymbol{y}}_{\boldsymbol{1i}}$ with the deflection conjugate angle of the torsional spring, δ_i.

3.2 Kinematical Constraint Equations and Configuration Space of MoRIS

The requirement that each wheel ($i = 1, 2, 3$) to be in contact with the tube wall results in three kinematical constraints. Thus, the contact points' position can be expressed from the perspective of the robot and that of the tube as follows:

$$\begin{aligned} (\boldsymbol{r}_{\boldsymbol{C_i/O}})_{robot} &= \boldsymbol{r}_{\boldsymbol{C_i/P}} + \boldsymbol{r}_{\boldsymbol{P/O}} \\ (\boldsymbol{r}_{\boldsymbol{C_i/O}})_{tube} &= \boldsymbol{r}_{\boldsymbol{P'_i/O}}(s_i) + r\ \boldsymbol{R}_{\hat{\boldsymbol{e}}_{\boldsymbol{t}}}(\gamma_i) \cdot \hat{\boldsymbol{e}}_{\boldsymbol{n}}(s_i) \end{aligned} \tag{3.1}$$

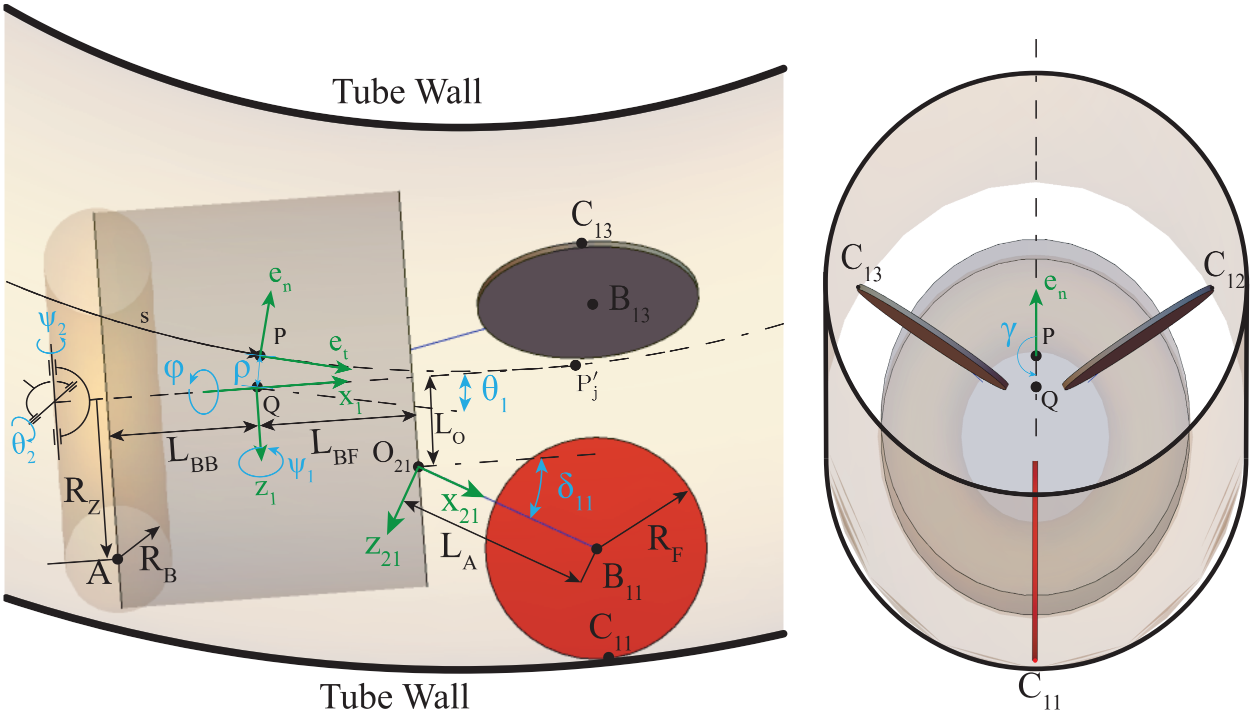
Tube Wall
C13
B13
e_n
P
s
e_t
ψ2
φ
ρ
Q
x1
θ1
P′j
θ2
L_O
L_BB
L_BF
O21
z1
ψ1
R_Z
R_B
A
δ11
x21
z21
L_A
R_F
B11
C11
Tube Wall
C13
C12
e_n
γ
P
Q
C11

Figure 3.1: Locomotion Vertebra diagram

where, P_i' is an intermediate point located on the centerline, and s_i and γ_i are intermediate coordinates used in solving the constraint equations.

Setting the two vectors equal, we find the kinematical constraints:

$$(\boldsymbol{r}_{\boldsymbol{C_i/O}})_{robot} = (\boldsymbol{r}_{\boldsymbol{C_i/O}})_{tube}. \tag{3.2}$$

In a straight tube section, the following equations are used:

$$\boldsymbol{r}_{\boldsymbol{C_i/P}} = \rho\hat{\boldsymbol{e}}_{\boldsymbol{n}} + L_{BF}\hat{\boldsymbol{\imath}}_{\boldsymbol{1}} + L_O\hat{\boldsymbol{k}}_{\boldsymbol{1}} + L_A\hat{\boldsymbol{\imath}}_{\boldsymbol{2i}} + R_F\hat{\boldsymbol{k}}_{\boldsymbol{2i}}|_{\delta_i\to\xi_i} \tag{3.3}$$

$$\hat{\boldsymbol{e}}_{\boldsymbol{t}} = \begin{pmatrix} \cos\theta\cos\psi \\ -\sin\theta\cos\psi\sin\phi - \sin\psi\cos\phi \\ \sin\psi\sin\phi - \sin\theta\cos\psi\cos\phi \end{pmatrix} \tag{3.4}$$

$$\boldsymbol{\hat{e}_n} = \begin{pmatrix} \cos\theta\cos\psi \\ -\sin\theta\cos\psi\sin\phi - \sin\psi\cos\phi \\ \sin\psi\sin\phi - \sin\theta\cos\psi\cos\phi \end{pmatrix} \tag{3.5}$$

$$\left\{\boldsymbol{\hat{i}_1}, \boldsymbol{\hat{j}_1}, \boldsymbol{\hat{k}_1}\right\} = \begin{pmatrix} 1 & 0 & 0 \\ 0 & 1 & 0 \\ 0 & 0 & 1 \end{pmatrix} \tag{3.6}$$

$$\boldsymbol{\hat{i}_{2i}} = \begin{pmatrix} \cos\delta \\ \sin\delta\sin(2\pi i/3) \\ -\sin\delta\cos(2\pi i/3) \end{pmatrix} \tag{3.7}$$

$$\boldsymbol{\hat{k}_{2i}} = \begin{pmatrix} \sin\delta \\ -\cos\delta\sin(2\pi i/3) \\ \cos\delta\cos(2\pi i/3) \end{pmatrix} \tag{3.8}$$

$$\xi_1 = \tan^{-1}\Big(\tan(\theta)\cos(\phi) - \sec(\theta)\tan(\psi)\sin(\phi)\Big) \tag{3.9}$$

$$\begin{aligned}\xi_2 = \tan^{-1}\Bigg(\frac{1}{2}\sec\theta\sec\psi\bigg(&\sin\phi\left(\sin\psi - \sqrt{3}\sin\theta\cos\psi\right) \\ &- \cos\phi\left(\sin\theta\cos\psi + \sqrt{3}\sin\psi\right)\bigg)\Bigg)\end{aligned} \tag{3.10}$$

$$\begin{aligned}\xi_3 = \tan^{-1}\Bigg(\frac{1}{2}\sec\theta\sec\psi\bigg(&\sin\phi\left(\sqrt{3}\sin\theta\cos\psi + \sin\psi\right) \\ &+ \cos\phi\left(\sqrt{3}\sin\psi - \sin\theta\cos\psi\right)\bigg)\Bigg)\end{aligned} \tag{3.11}$$

where, ξ_i is the solution to $\boldsymbol{\hat{k}_{2i}} \cdot \boldsymbol{\hat{e}_t} = 0$. This corresponds to the direction of $\boldsymbol{r_{C_i/B_i}}$. To facilitate the detection of contact between the hex roller with the tube's wall, an additional coordinate is introduced as:

$$p = R_B + R_Z \cos(\theta) + \rho \tag{3.12}$$

where, R_Z and R_B are shown in Fig. 3.1.

In order to describe the position and the orientation of the robot inside the tube network we need the following generalized coordinates: $\boldsymbol{q} = \{s, \rho, \gamma, \psi, \theta, \phi\}$. To complete the description of the robot's configuration we need the additional coordinates δ_i obtained by solving the kinematical constraint equations. Thus, the robot has a total of nine degrees of freedom. The constrained generalized coordinates that form the configuration space of the system become:

$$\boldsymbol{q_s} = \{s, \gamma, \rho, \psi, \theta, \phi, p, \delta_1, \delta_2, \delta_3\}. \tag{3.13}$$

3.3 Potential Energy in MoRIS

The elastic potential energy is defined as:

$$V_s = k \sum_{i=1}^{3} (\delta_0 - \delta_i)^2. \tag{3.14}$$

To find the extremum of the energy, we take the derivative and set it equal to zero:

$$\nabla V_s(\boldsymbol{q}) = 0. \tag{3.15}$$

In Fig. 3.2, the two curves show the potential elastic energy corresponding to equilibrium points as coordinate ρ varies between the extreme values corresponding to the hex roller contacting the tube wall ($p = r$). The robot is considered to be in a straight segment and two values of the roll angle, ϕ, were considered. The plot shows that the maximum energy corresponds to the centerline position and as the magnitude of ρ increases, the energy decreases. Thus, in the absence of an additional Vertebrae, the robot will settle in the position where the hex roller contacts the wall.

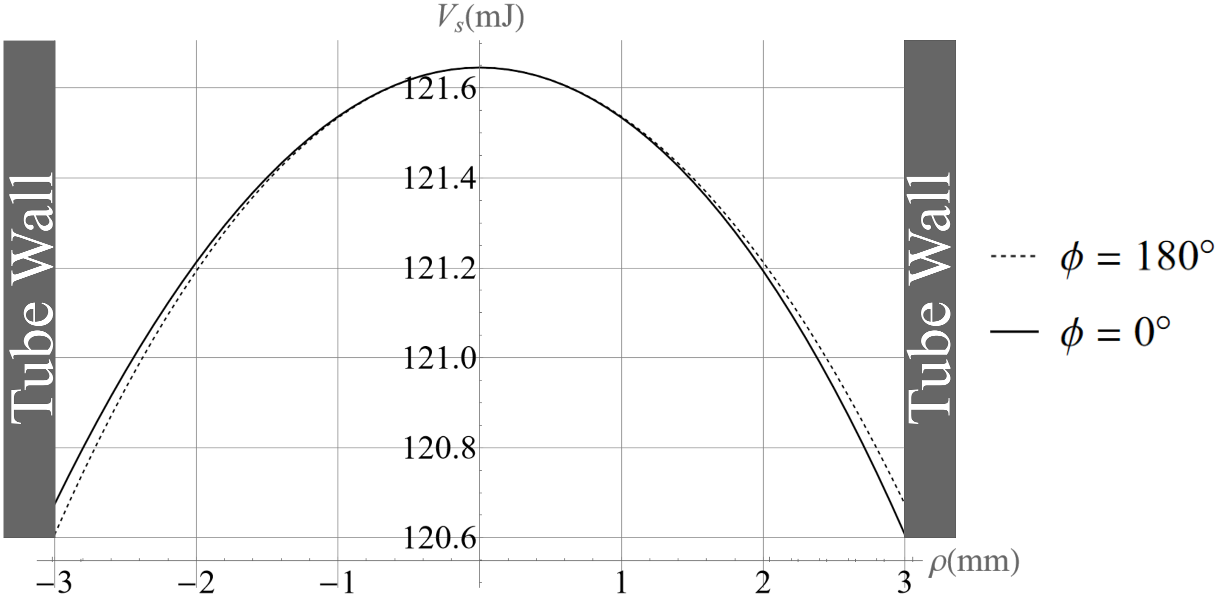

Figure 3.2: Potential elastic energy variation vs. ρ in a straight tube segment.

3.3.1 Configuration Constrained Space

The configuration constrained space for the Vertebra can be identified by solving the kinematically constrained equations (all wheels maintaining contact with the wall), with $p = r$ and limiting the δ_i within their physical range. Due to the axial and radial symmetry of a straight tube segment, s and γ can be held constant and not included in the analysis.

Figure 3.3a was formed by using 1,278 simulations performed in Mathematica v.13 (Wolfram Research, Inc). The constrained configuration space can be represented in the attitude angle coordinates and it forms a twisted Reuleaux triangular prism. A horizontal crossection of this space, at $\phi = 0°$, is shown in Fig. 3.3b with elastic energy contours and a vertical crossection at $\psi = 0°$, is shown in Fig. 3.3c. The slice shows that the minimum elastic potential energy exists approximately in the center. By starting the numerical solution at the centroid, the minimum energy can be found as the roll angle is varied (see Fig. 3.4).

The minimum energy value is repeated every 120° due to the Locomotion Vertebra suspension arms placed every 120°. Figure 3.3d shows Locomotion Vertebra in the minimum energy equilibrium.

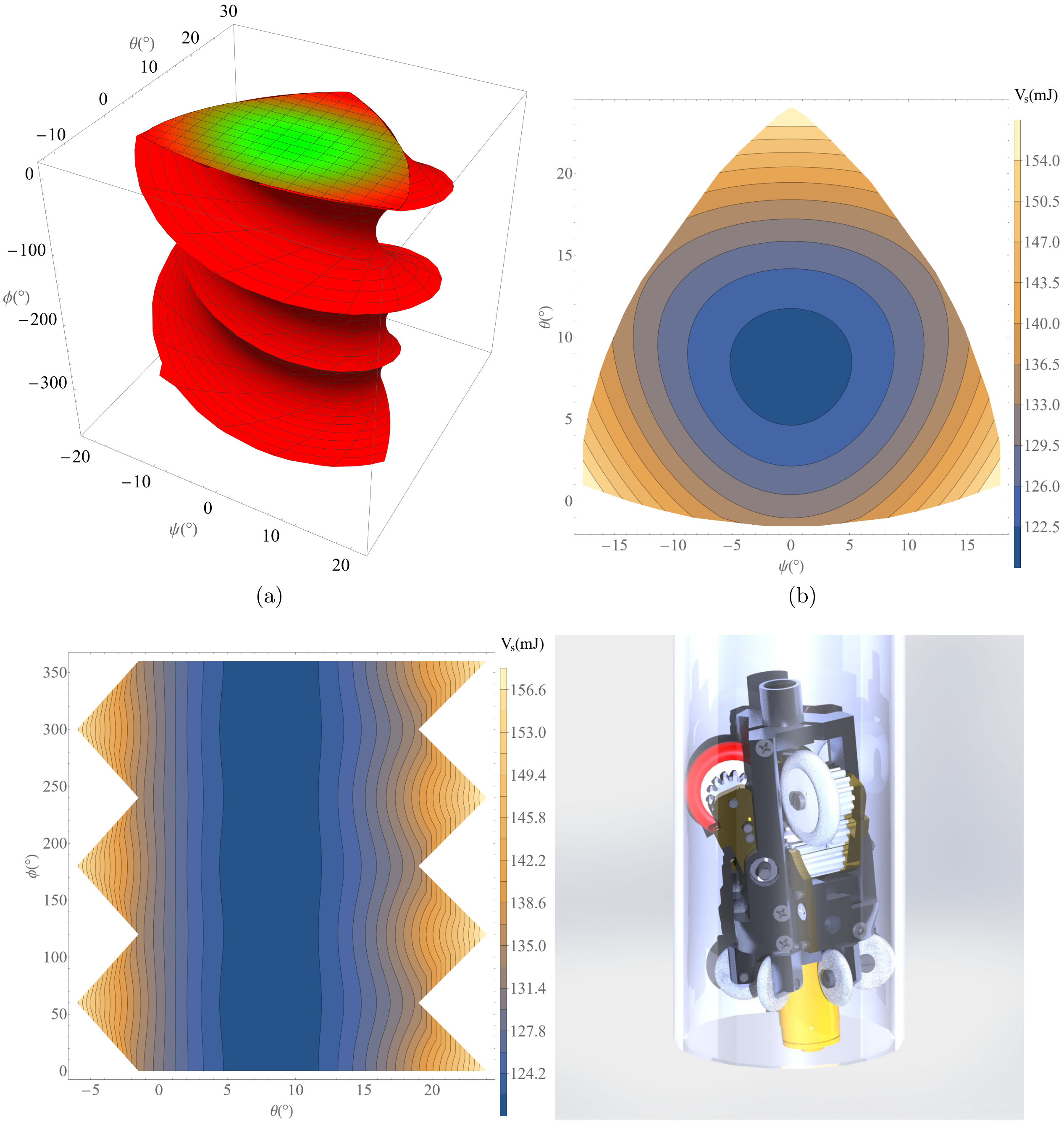

(a) (b)

(c) (d)

Figure 3.3: (a) Locomotion Vertebra configuration space at $p = r$. (b) Horizontal slice at $\phi = 0$. (c) Vertical slice at $\psi = 0$. (d) Dynamic equilibrium orientation of Locomotion Vertebra.

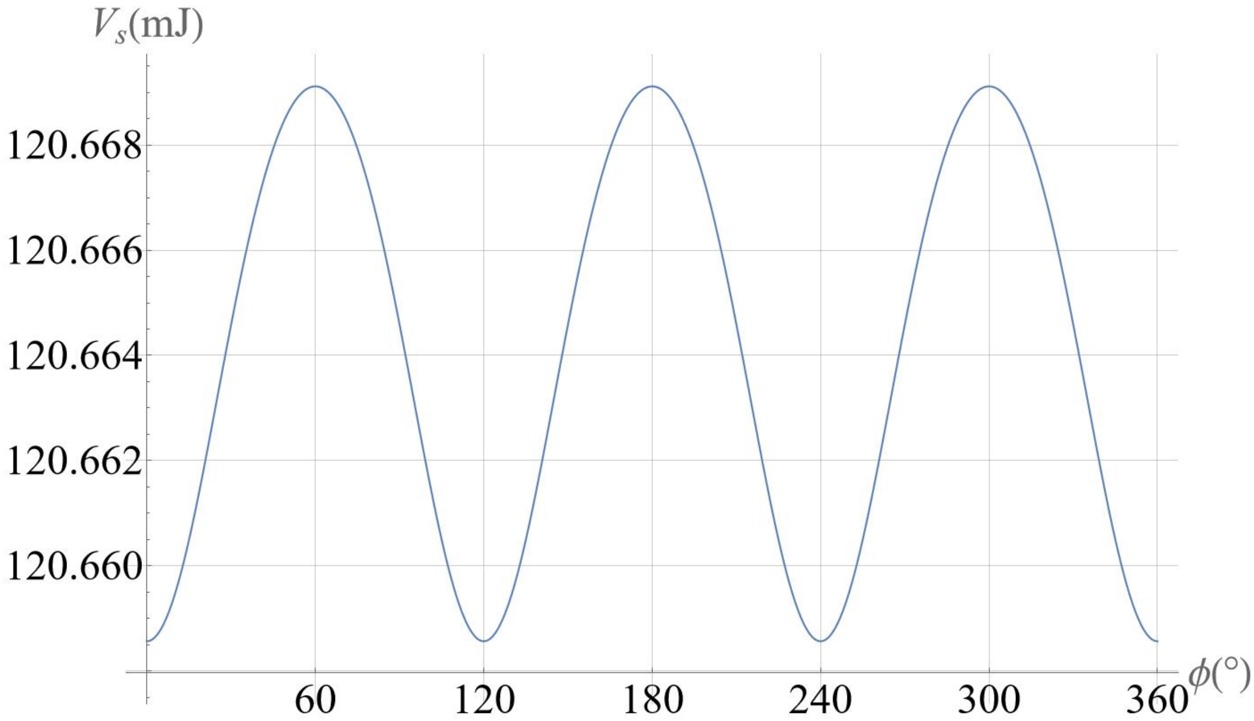

Figure 3.4: Minimum energy with respect to ϕ at $p = r$.

3.4 Combined Vertebrae Settling Orientation

To consider the settling response of the Locomotion Vertebra and Camera Vertebra combined, two additional unconstrained coordinates (θ_2, ψ_2) and three additional constrained coordinates $(\delta_{21}, \delta_{22}, \delta_{23})$ are introduced. The unconstrained coordinates are shown in Fig. 3.1 as the degrees of freedom to two orthogonal pin joints. These joints are mathematically and practically equivalent to the spring and wires that connect the Locomotion Vertebra to the Camera Vertebra. In fact, a n-number vertebra spine can be used in this method, with coordinates $(\theta_i, \psi_i, \delta_{i1}, \delta_{i2}, \delta_{i3})$ cooresponding to the i-th vertebra.

As shown in section 3.3.1 for a single Vertebra, the minimum elastic potential energy is at the tube wall. Figure 3.5 shows the settling orientation of the multi-vertebra spine with respect to the coordinate ρ. As a result of the connecting elastic joints, the minimum is not at the tube wall. With a single vertebra, the deflection of the suspension would decrease monotonically as the magnitude of ρ increased. However, for the multi-vertebrae spine, the deflection of the elastic joints (θ_2 and ψ_2) increases with ρ. This causes the minimum to be

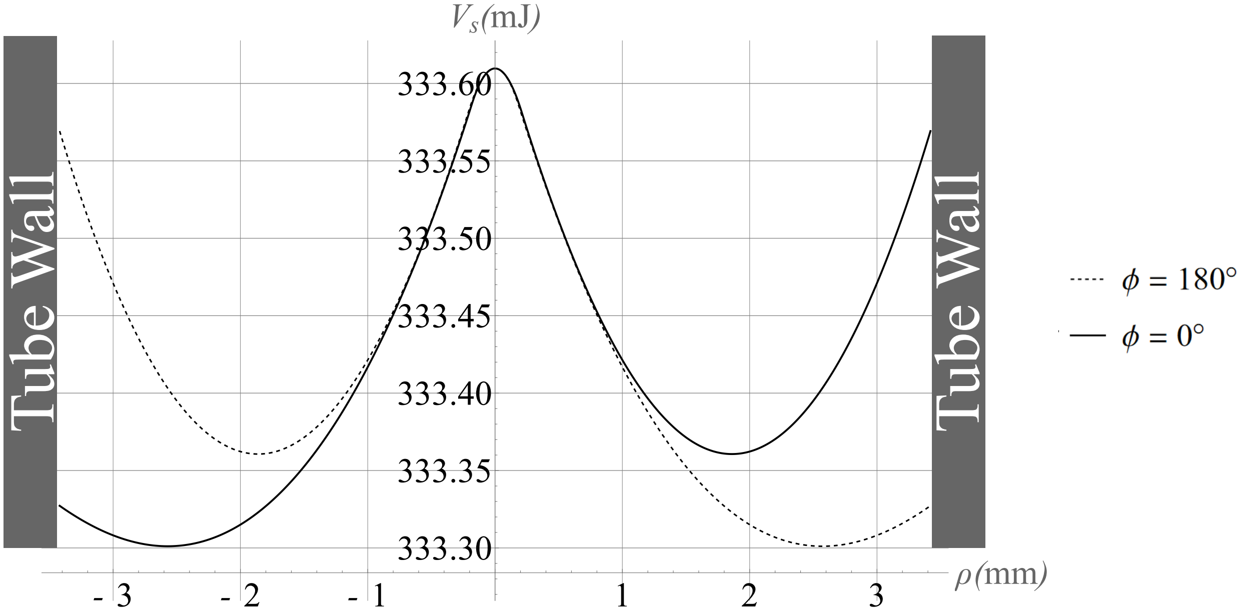

Figure 3.5: Potential elastic energy variation vs. ρ in a straight tube segment for the total Vertebrae.

moved closer to the tube centerline and the relation is no longer monotonic. The settling orientation for the CAD model is shown in Fig. 3.6.

3.5 Velocity Constraints of MoRIS

In addition to the configuration constraints we have to consider the velocity constraint that keeps the tractive wheel aligned with the direction tangent to the path. Ideally, if the body of the robot is aligned along the centerline of the tube, then all the wheels are aligned and the paths will follow the centerline with an offset (dashed curves Fig. 3.7). However, in reality the body is misaligned and the deflection of the suspension arms are different. Assuming no slippage at the tractive wheel tire/tube wall contact point, $\boldsymbol{v_{C_1}} = 0$. As a result, the path that the tractive wheel must follow is a curved path, as shown by the thick solid line in Fig. 3.7. Therefore, the velocity constraints for the other two wheels must be violated, resulting in wheel slippage. This is the reason why the tractive wheel has a high friction rubber tire. Whereas, the other Locomotion Vertebra wheels are manufactured from delrin plastic. Even with such a slippery material, there is still drag friction that the motor must overcome.

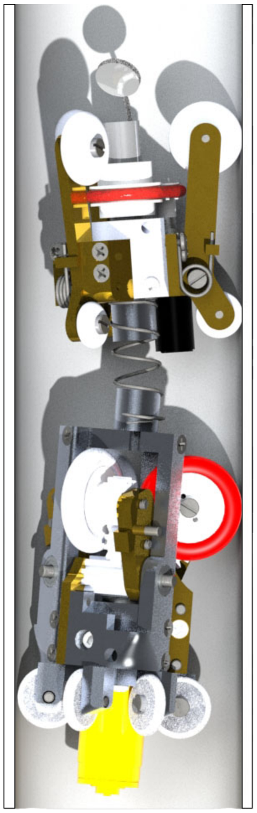

Figure 3.6: Dynamic equilibrium orientation of total Vertebrae.

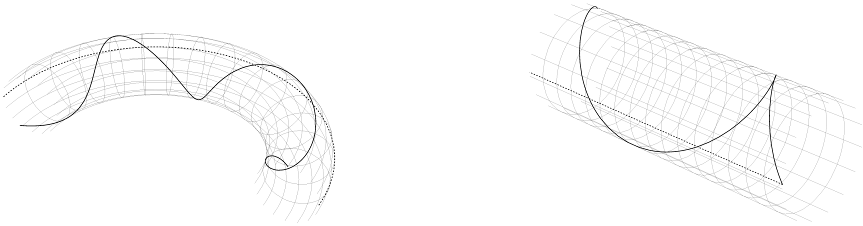

(a) Curved section

(b) Straight section

Figure 3.7: Kinematic paths

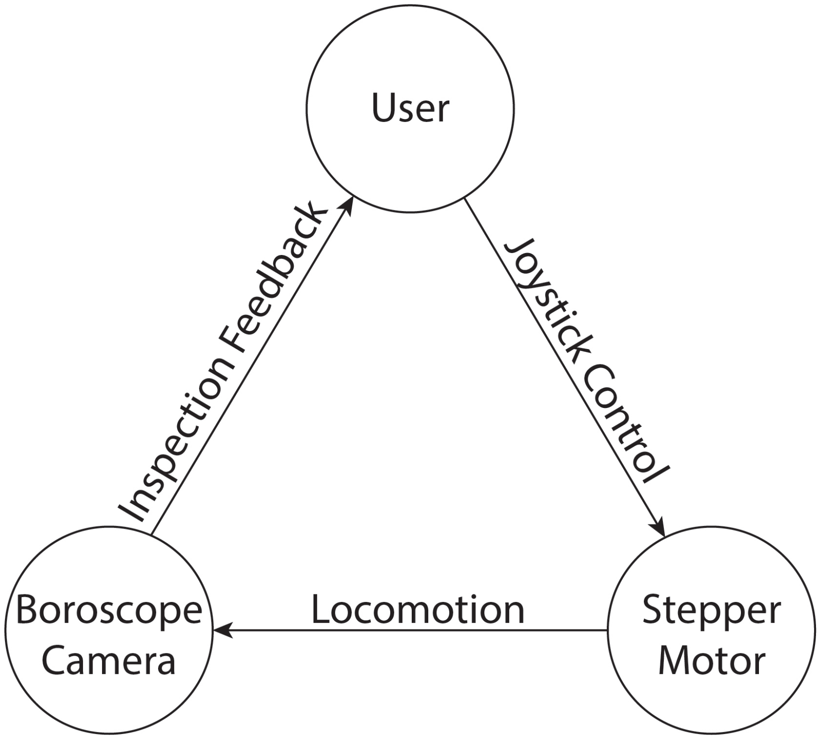

Figure 3.8: User-integrated control feedback loop

3.6 Control

The control of MoRIS is a user-integrated closed loop system. After setup, the user inputs a desired speed and a computer outputs video image of the inside of the network. The user adjusts the position and orientation of MoRIS as needed by an inspection task. Figure 3.8 shows the control system block diagram. The user controls the Vertebrae through a 2-axis joystick. One axis controls the motor speed of the Locomotion Vertebra. The second axis controls the motor speed of the Camera Vertebra. Tuned velocity profiles for the stepper motors are develop and tested before the deployment of MoRIS. As the Vertebra travel in the tube network, the user watches the live video footage of the borescope camera. When an point of interest is found, the user enters the tether length, measured from the Base Station, into the localization algorithm. The localization algorithm returns the tube centerline position of interest.

Chapter 4

Localization

When MoRIS is deep in a tube network, the only way to absolutely know the location of the Vertebrae is through the length of the tether. The tether's length in the tube network, when taut, is directly related to the actual location. A localization function has been developed to convert between the tether length and the robot position in the tube network.

4.1 Tube Network Model

There is a generalized pattern of tube networks that can be considered here. For an accurate localization, the tube network model presented in section 2.1 is used.

As mentioned before in section 2, all of the bends in the tube networks of jet aircraft lie on a plane. So, in analyzing the tube network, the model begins with an alternating list of straight and bent tube segments, or $t_i = \{t_S, t_B, t_S, t_B, ...\}$. In cases that there is a missing straight section, the length of t_S is zero. In Appendix 2, the algorithm for setting up the model is presented. The algorithm begins with setting up a list of the tube network centerline lengths, c_i. Each element of c_i corresponds to the centerline length of the tube network at the end of the $i-th$ section of the tube network. Next, a list of coordinate systems, $\boldsymbol{F}_i$, is setup. This list represents the coordinate frame for each section of the tube network. Finally, a list, called $\boldsymbol{m}_i$, holds the mathematical model of each corresponding tube network section.

4.2 Tether Positioning

Once a mathematical model of the tube network has been developed, using certain assumptions, a model of the tether in the tube network can be made. The model assumes that the tether is taut. This means that between bends, in straight sections, the tether can be represented as a line. This also means that the tether is tight against the tube bend wall at the surface closest to the center of the bend. So, the tether can be approximated as a circular arc. These assumptions ignore factors such as gravity, tether flexibility, and cases the tether is not taut. The model of the tether begins with calculating the geometric points that the tether alternates between the straight sections and the bends. A list of points, $\boldsymbol{t}_{Pi}$, is created in Appendix 4. This list contains the points corresponding to these transitions. The transitions are calculated using projections.

4.3 Tether Projection on Tube Centerline

Now that the geometry of the tube network and the tether in the network have been quantified, the tether model can be projected onto the tube network model for localization. Using $\boldsymbol{t}_{Pi}$, the centerline length, b_i, can be calculated. b_i is the centerline length corresponding to each point the tether transitions from a straight section to a bend. This is different from c_i because it corresponds to tether tangencies. The values c_i cooresponds to the geometry of the tube network and not the tether.

4.4 Localization Function

Finally, now that the tube network and the tether have been modeled, a piecewise one-to-one function can be found:

$$F[t] = \{r_i\} \tag{4.1}$$

where, $i \in \{1...\frac{1}{2}(3\boldsymbol{t}_n.size - 7)\}$. This function is derived in Appendix 5.

4.5 Experimental Results of MoRIS

MoRIS was prototyped in the machine shop at Southern Methodist University. The prototype is shown in Fig 4.2. Once the prototype is built, the next step is validation. In supplemental videos, the Vertebrae are shown to successfully travel through a BWG 1-1/2" diameter 16-gauge tube in all possible orientations. Other videos show interior views from the Camera Vertebra as the Vertebrae travel through bends. Finally, a video shows the view through the rotating mirror. The final validation is the success of the localization algorithm.

Before the full algorithm can be tested, the encoder on the Base Station is validated. A short experiment was conducted in which the Vertebrae was sent down a transparent plastic tube. A tape measure was used to compare the calculated tether length with the encoder to the actual tether length. The results are shown in Fig 4.3. The thick curve is the robot

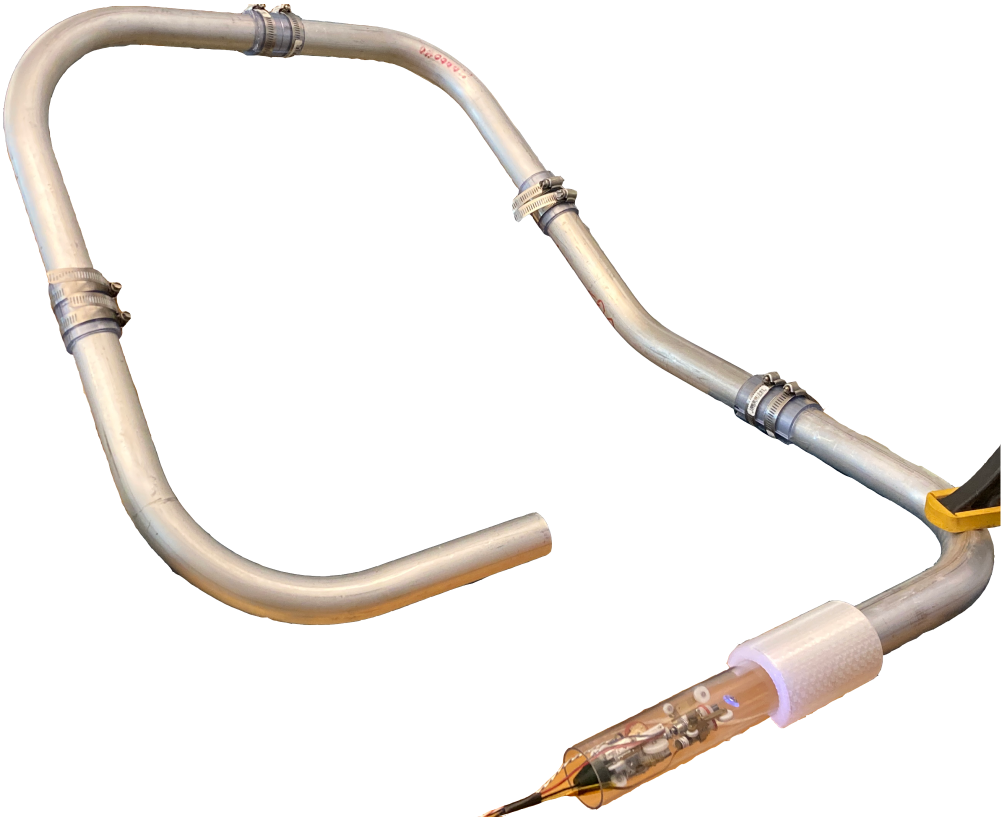

(a)

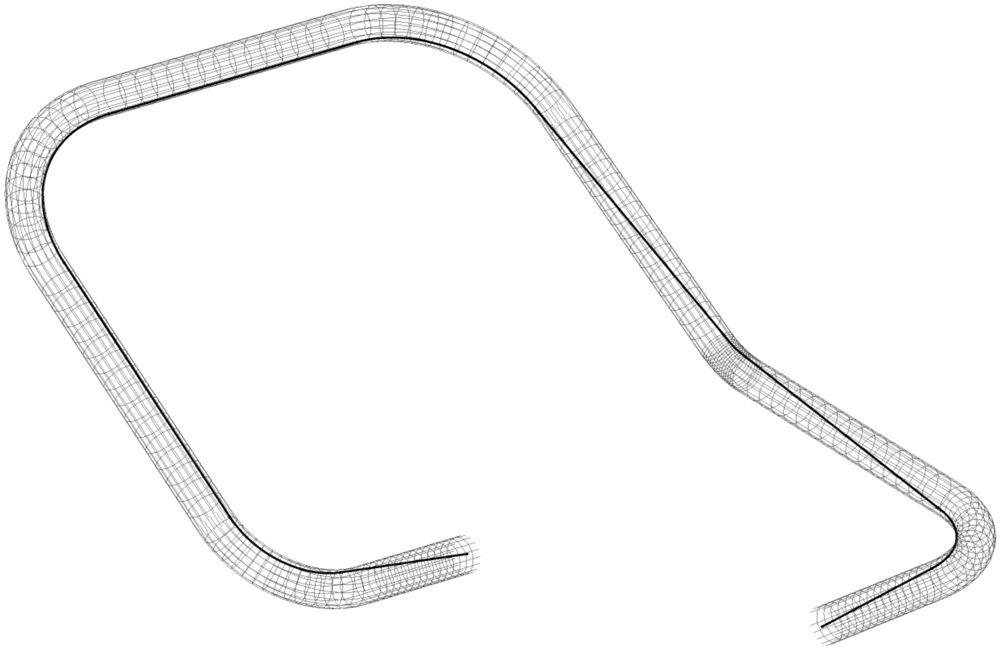

(b)

Figure 4.1: Bent tube network experimental setup (a) and model (b).

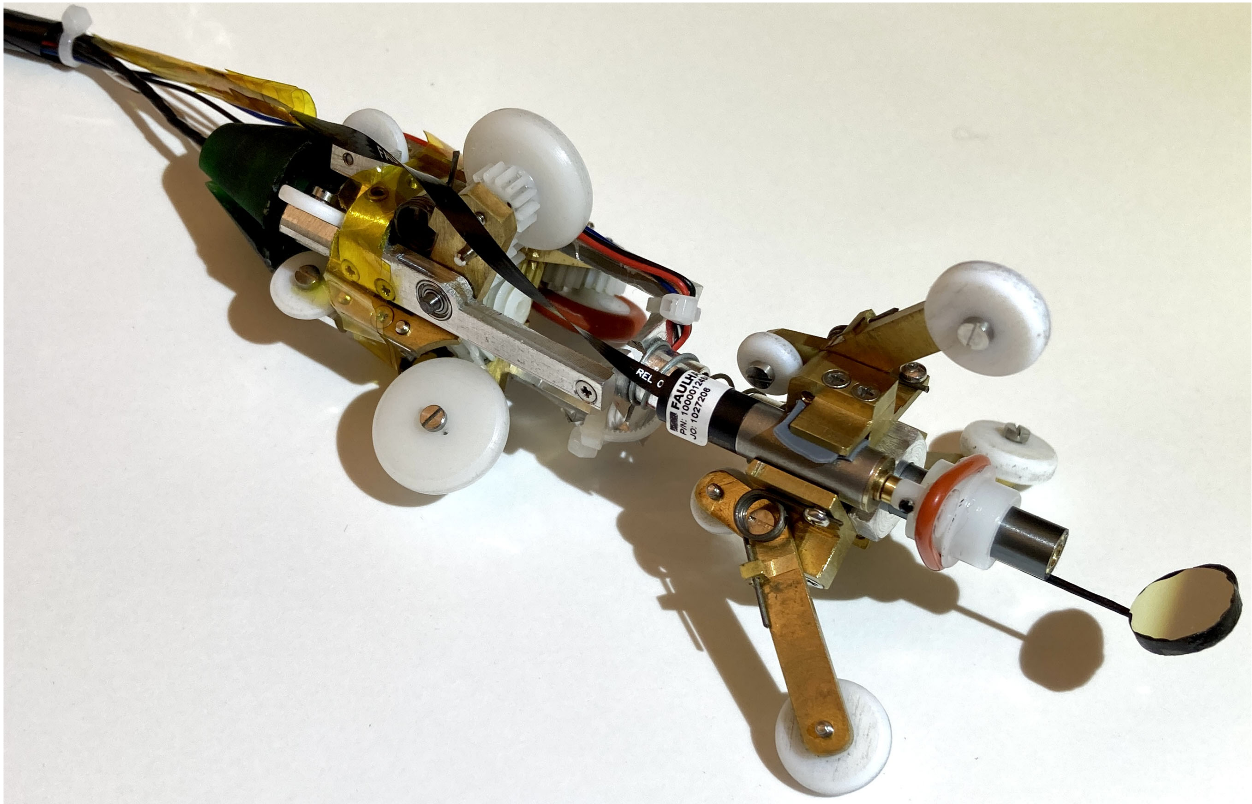

Figure 4.2: Vertebrae prototype

position according to the steps from the stepper motor driving the Locomotion Vertebra. The thin curve is the robot position according to the tether reel. The stepper motor's average error is 18.58 cm. This error is mostly caused by lost steps and slippage, which is caused by external forces opposing motion. The tether reel's average error is -2.23 cm. This error is caused by the tether not being completely taut and by the radius of the reel changing as the amount of wound tether decreases and increases. Lockheed Martin requires an accuracy of 10.16 cm. The stepper motor proved to not be accurate enough, but the tether reel is well within bounds.

Next, an experiment was setup to validate the localization algorithm in tube networks with bends. In Fig 4.1a, the tube network is shown. In Fig 4.1b, the computer model of this network is shown. Also, in the figure, the thick curve represents the tether.

The experimental network has four 90° bends, one 30° bend, and straight sections between. The 30° bend is tilted at an angle such that the robot climbs uphill. The angle

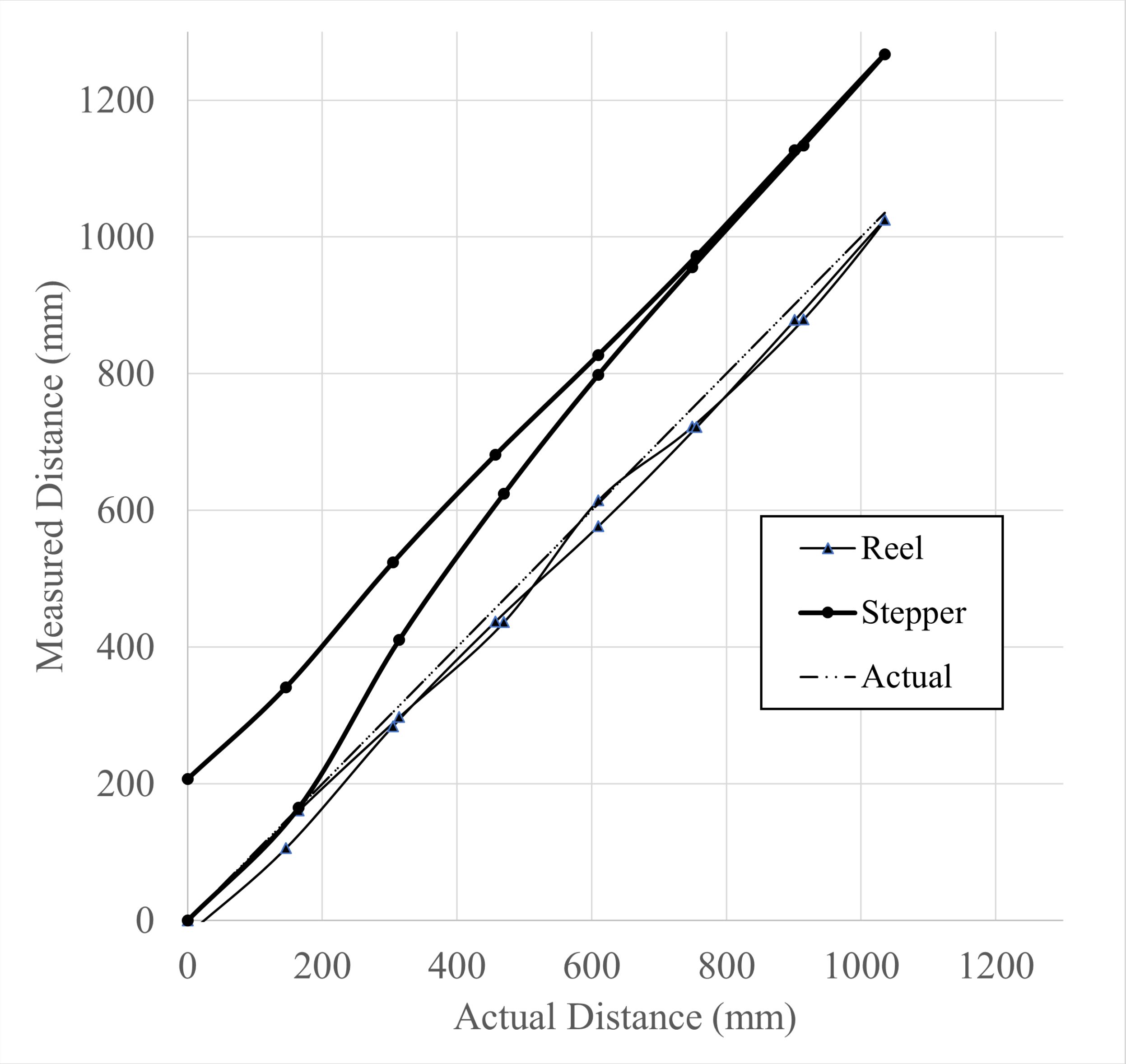

Figure 4.3: Measured position vs. actual position in a straight tube

Table 4.1: Tube Model Parameters

i	l (mm)	σ (°)	R (mm)	β
1	130.175			
2		0	101.6	90 °
3	285.75			
4		90 °	101.6	30 °
5	279.4			
6		-1.49383	152.4	90 °
7	292.1			
8		0	152.4	90 °
9	292.1			
10		-0.076969	101.6	90 °
11	127			

σ is angle between adjacent tube bends plane of curvature. In Fig 4.4, the results of the localization function applied to this network are shown. The solid curve is the localization function developed. The cross markers are the actual network joint positions. In the experiment, tether length measurements were taken at predefined positions in the tube. These positions are chosen as the joints between sections. The actual location of the Vertebrae could be visually localized using the camera's view. These measurements and the output of the localization function are plotted for validation. The localization algorithm error was specified as the difference in tether lengths measured from experiments and predicted by the algorithm at the end of the tube network. This was chosen as the error would be the greatest here through the accumulation of error from the previous sections. This average error was found to be about 19.7 mm. This result is well below the required accuracy of 101.6 mm, specified by Lockheed Martin. Therefore, with tube networks of up to approximately 7.5 feet long, the localization algorithm has been shown to be successful in predicting the centerline position of the vertebrae with inspections.

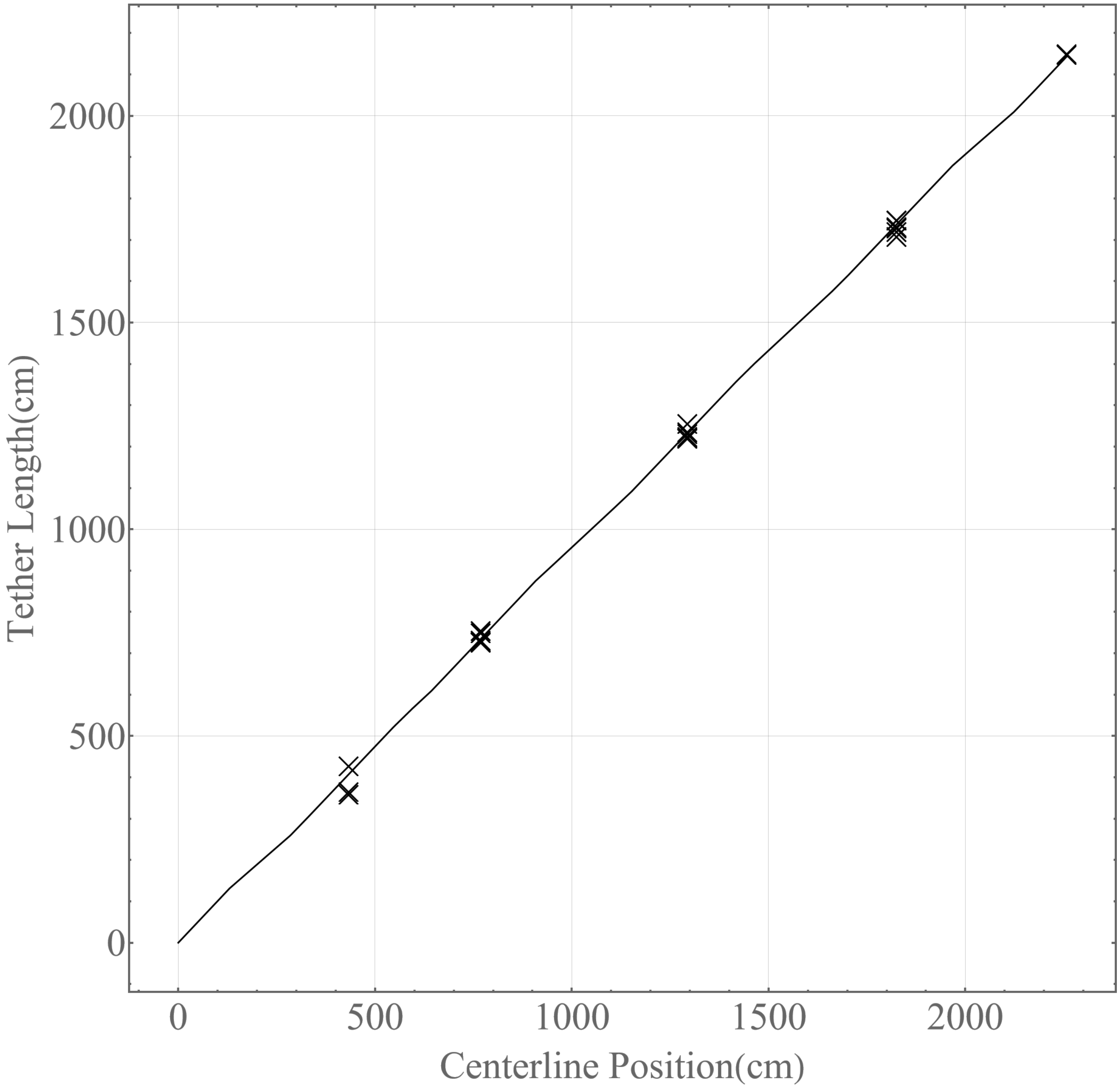

Figure 4.4: Localization function

Chapter 5

Methods and Materials of Big Foot

5.1 Robot design and manufacturing

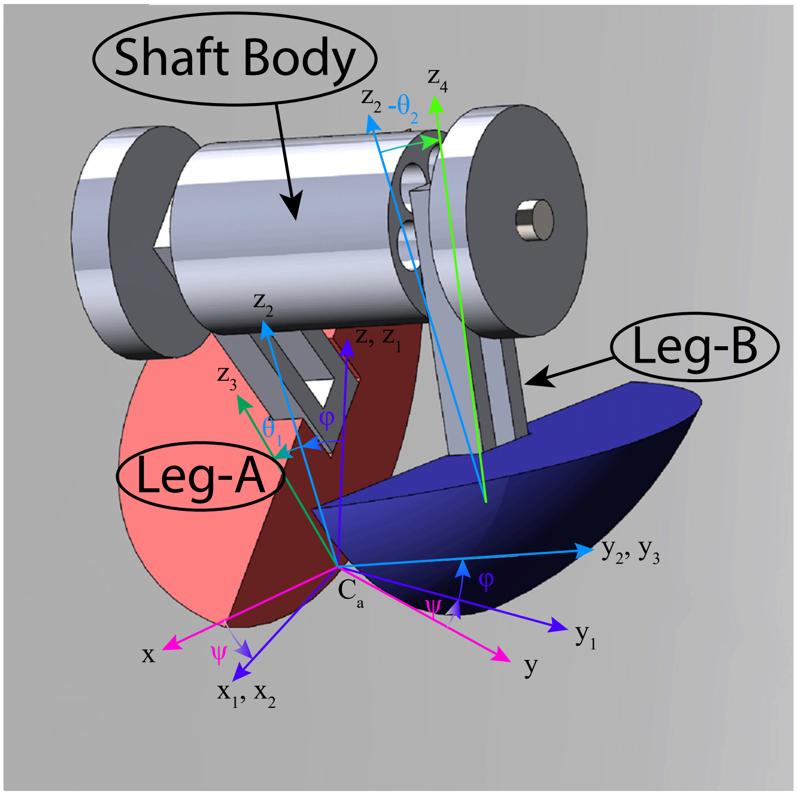
Shaft Body
z_4
z_2 $-\theta_2$
z_2
z, z_1
z_3
θ_1
φ
Leg-B
Leg-A
y_2, y_3
φ
C_a
ψ
y_1
x
ψ
y
x_1, x_2

Figure 5.1: Isometric view of the multi-body diagram of Big Foot

Big Foot is actuated by simply placing a magnet in its body. Magnetic actuation highly simplifies the design and manufacturing of the robot. Figure 5.1 shows the design of Big Foot.

Raw materials were acquired from Amazon (Seattle, Washington, USA) and McMaster-Carr (Elmhurst, Illinois, USA). The design includes 3 main assemblies. The first two assemblies are Leg-A and Leg-B. These two assemblies mirror each other. The Leg assemblies contain 3 parts: the Leg, the Foot, and 5 minute set Gorilla Glue epoxy (Cincinnati, Ohio, USA). The leg is configured such that there is a hole for a shaft, and a rectangular slot to reduce weight and add surface area for the adhesive. The leg's material is Delrin, which is a self-lubricating plastic. This reduces friction between the sliding surfaces of Big Foot. Finally, Delrin is easily machinable, which is important when machining very small parts. Accordingly, the leg was manufactured by the PS48 laser cutter and engraver (Full Spectrum Laser, Las Vegas, NV, USA). The leg is 6.5x0.79x1.75 mm. Next, the feet were built using a Photon S SLA 3D printer (AnyCubic, Shenzhen, Guangdong, China). The feet are a section of a 8mm sphere. The feet were designed to smoothly transfer Big Foot's linear momentum during each step [110]. The design also stabilizes the robot while it is tilting.

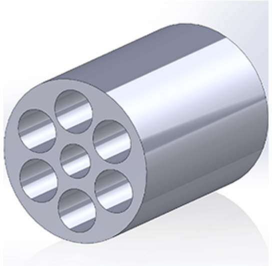

Figure 5.2: Indexed Shaft Cylinder

The upper body is called the Shaft Body. The CAD model of the Shaft Body's Cylinder is shown in Fig 5.2. The Cylinder consists of a central bore and six equally spaced cells. The central bore transition fits with the 0.794 mm diameter shaft. The cells are transition fits for 1mm diameter Neodymium magnets (Super Magnet Man, Pelham, AL, USA). The shaft is made from a non-magnetic stainless steel. The purpose of the Shaft Body is to hold the magnet and connect the legs. Notice in magnetic actuation that the location of the magnets does not effect the performance because the actuation is through a torque and not a force. Two prototypes were produced. These prototypes are shown in Fig. 5.3. The larger robot with the green feet was produced to initially check the feasibility of the dynamics. Once successfully test, the smaller white prototype was produced. This prototype is what we call Big Foot and the robot design that is used in this paper.

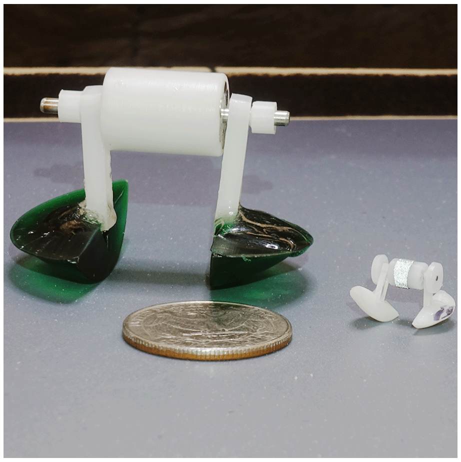

Figure 5.3: Big Foot prototypes

5.2 Dynamics

5.2.1 Coordinate Frames

A generalized model of Big Foot is shown in Fig 5.1 and Fig 5.4. The components of Big Foot include two legs with integrated feet, and a central shaft. The legs are designed such that the center of mass is close to the ground, and the feet give Big Foot a vertical static equilibrium orientation.

Six coordinate systems are required to fully model Big Foot's dynamics:

1. The Platform Fixed coordinate system; $\{\hat{\boldsymbol{\imath}}, \hat{\boldsymbol{\jmath}}, \hat{\boldsymbol{k}}\} = \boldsymbol{I}$.

2. The Space Fixed coordinate system; $\{\hat{\boldsymbol{I}}, \hat{\boldsymbol{J}}, \hat{\boldsymbol{K}}\} = [\boldsymbol{R}_{\boldsymbol{y}}(\boldsymbol{\beta})]^{\boldsymbol{T}} \{\hat{\boldsymbol{\imath}}, \hat{\boldsymbol{\jmath}}, \hat{\boldsymbol{k}}\}$.

3. An Intermediate coordinate system; $\{\hat{\boldsymbol{i}}_1, \hat{\boldsymbol{j}}_1, \hat{\boldsymbol{k}}_1\} = [\boldsymbol{R_z}(\boldsymbol{\psi})]\{\hat{\boldsymbol{I}}, \hat{\boldsymbol{J}}, \hat{\boldsymbol{K}}\}$.

4. The Shaft Fixed coordinate system; $\{\hat{\boldsymbol{i}}_2, \hat{\boldsymbol{j}}_2, \hat{\boldsymbol{k}}_2\} = [\boldsymbol{R_x}(\boldsymbol{\phi})]\{\hat{\boldsymbol{i}}_1, \hat{\boldsymbol{j}}_1, \hat{\boldsymbol{k}}_1\}$.

5. The Leg-A Fixed coordinate system; $\{\hat{\boldsymbol{i}}_3, \hat{\boldsymbol{j}}_3, \hat{\boldsymbol{k}}_3\} = [\boldsymbol{R_y}(\boldsymbol{\theta_1})]\{\hat{\boldsymbol{i}}_2, \hat{\boldsymbol{j}}_2, \hat{\boldsymbol{k}}_2\}$.

6. The Leg-B Fixed coordinate system; $\{\hat{\boldsymbol{i}}_4, \hat{\boldsymbol{j}}_4, \hat{\boldsymbol{k}}_4\} = [\boldsymbol{R_y}(\boldsymbol{\theta_2})]\{\hat{\boldsymbol{i}}_2, \hat{\boldsymbol{j}}_2, \hat{\boldsymbol{k}}_2\}$.

The following coordinate transformations are required to fully define the coordinate frames. The simple rotation transformations $\{[\boldsymbol{R_x}], [\boldsymbol{R_y}], [\boldsymbol{R_z}]\}$ are from Ginsberg's foundational textbook [107]. First, a rotation of β about $\hat{\boldsymbol{J}}$ transforms the Space Fixed coordinate system to the Platform Fixed coordinate system. In Fig 5.1 and Fig 5.4, the Space Fixed coordinate system is not shown. The Platform Fixed coordinate system is aligned with the surface Big Foot is walking on. Next, a rotation of ψ about about $\hat{\boldsymbol{k}}$, followed by a rotation of ϕ about $\hat{\boldsymbol{j}}_1$, transforms the Platform Fixed coordinate system to the Shaft Fixed coordinate system. The Platform Fixed coordinate system is chosen as the global for the final equations of motion. Subsequently, a rotation of θ_1 and θ_2 about $\hat{\boldsymbol{j}}_2$ transform the Shaft Fixed coordinate system to the Leg-A and Leg-B coordinate systems. Figure 5.1 shows these transformations.

5.2.2 Hybrid System

As a biped robot, Big Foot is a hybrid system [58]. In general for bipedal walkers, there are two states $\{a, b\}$. These states correspond to which foot a bipedal walker is standing on. Big Foot actually has four states corresponding to the contact point between Big Foot and the platform: $\{a, b, c, d\}$

a) Leg-A foot inner edge

b) Leg-B foot inner edge

c) Leg-A foot curved surface

d) Leg-B foot curved surface

These states are a result of the unique foot design. In numerical simulations, the switching between states is achieved by toggling the respective state to 1 and the other states to 0.

5.2.3 Position Vectors

To develop the kinematic constraints of motion and the centers of mass, the following position vectors have been defined. These positions are shown in Fig 5.4. Point $\boldsymbol{r_{C_i/O}}$ is the position vector of the foot/platform contact point. Point $\boldsymbol{r_{A_i/O}}$ is the position of the center of the joint connecting the leg with the shaft. Finally, $\boldsymbol{r_{D/O}}$ is the position of the center of the shaft.

$$\boldsymbol{r_{D/O}} = \boldsymbol{r_{A_i/O}} + (a-b)L\boldsymbol{\hat{j}_2}. \tag{5.1}$$

where,

$$\boldsymbol{r_{A_i/O}} = \begin{bmatrix} X \\ Y \\ Z \end{bmatrix}. \tag{5.2}$$

The coordinates of the center of mass for the rigid bodies are as follows. The position vector of the center of mass (COM) Leg-A is $\boldsymbol{r_{G_A/O}}$ and Leg-B is $\boldsymbol{r_{G_B/O}}$. The COM of the shaft body is $\boldsymbol{r_{G_D/O}}$. These vectors are defined as:

$$\begin{aligned} \boldsymbol{r_{G_A/O}} &= \boldsymbol{r_{D/O}} - L_G\boldsymbol{\hat{j}_2} - H_G\boldsymbol{\hat{k}_3}. \\ \boldsymbol{r_{G_B/O}} &= \boldsymbol{r_{D/O}} + L_G\boldsymbol{\hat{j}_2} - H_G\boldsymbol{\hat{k}_4}. \\ \boldsymbol{r_{G_D/O}} &= \boldsymbol{r_{D/O}}. \end{aligned} \tag{5.3}$$

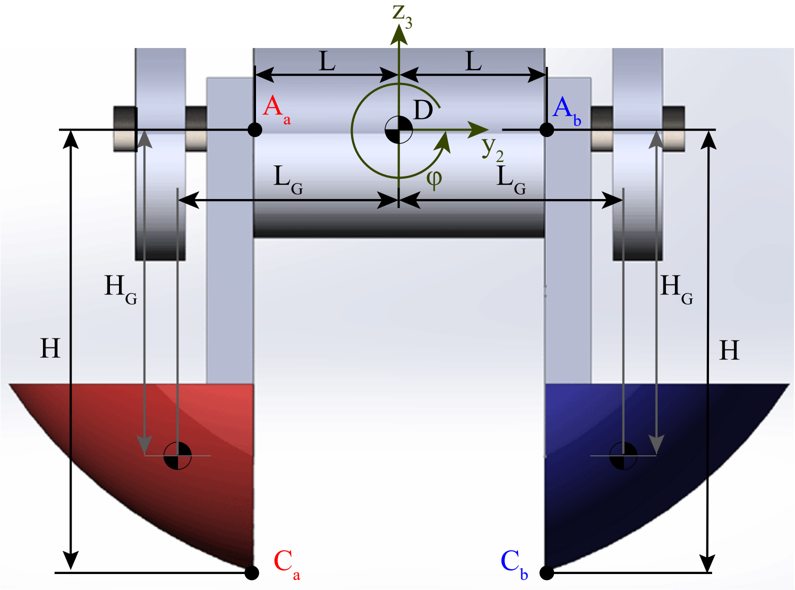

Figure 5.4: The Multi-Body Diagram of Big Foot from an frontal view

5.2.4 Angular Velocities

Next, the angular velocities are defined. The angular velocities of Leg-A, Leg-B, and the Shaft Body are $\boldsymbol{\omega}_1$, $\boldsymbol{\omega}_2$, and $\boldsymbol{\omega}_3$, respectively.

$$\begin{aligned}\boldsymbol{\omega_1} &= \dot{\psi}\hat{\boldsymbol{k}} + \dot{\phi}\hat{\boldsymbol{i}}_{\boldsymbol{1}} + \dot{\theta}_1\hat{\boldsymbol{j}}_{\boldsymbol{2}}.\\ \boldsymbol{\omega_2} &= \dot{\psi}\hat{\boldsymbol{k}} + \dot{\phi}\hat{\boldsymbol{i}}_{\boldsymbol{1}} + \dot{\theta}_2\hat{\boldsymbol{j}}_{\boldsymbol{2}}.\\ \boldsymbol{\omega_3} &= \dot{\psi}\hat{\boldsymbol{k}} + \dot{\phi}\hat{\boldsymbol{i}}_{\boldsymbol{1}}.\end{aligned} \tag{5.4}$$

There is only two angular velocities for the Shaft Body because there are no moments acting about the $\hat{\boldsymbol{j}}_{\boldsymbol{2}}$ direction, which makes one degree of freedom of the Shaft Body static and able to be ignored.

5.2.5 Velocity Constraint

Next, a velocity constraint must be defined for the position of Big Foot with respect to the walking surface. The feet are designed to be circular, as shown in Fig 5.5.

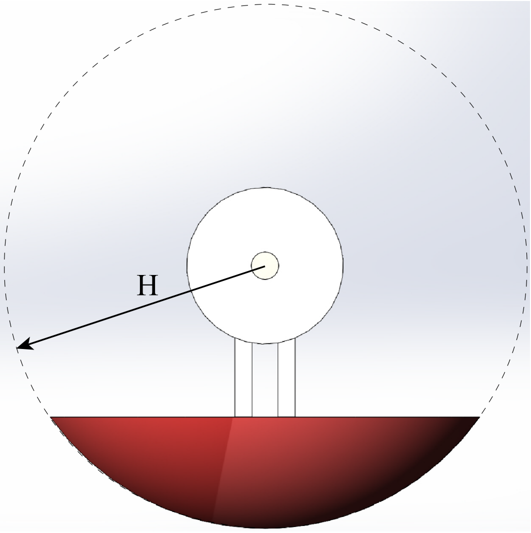

Figure 5.5: Side View of Foot Curvature

Two velocity constraints exist for each state. The first velocity constraint is the requirement that the foot is in contact with the ground. This is modeled as the velocity of the foot contact point with the platform, $\dot{C}_i$, is zero.

Next, a velocity constraint exists that represents the roll of the circular foot on the platform as Big Foot moves. There are four equations for this constraint corresponding to each state.

a) $\dot{\boldsymbol{r}}_{\boldsymbol{A_i/O}} = \boldsymbol{\omega_1} \times \boldsymbol{r}_{\boldsymbol{A_A/C_A}}$

b) $\dot{\boldsymbol{r}}_{\boldsymbol{A_i/O}} = \boldsymbol{\omega_2} \times \boldsymbol{r}_{\boldsymbol{A_B/C_B}}$

c) $\dot{\boldsymbol{r}}_{\boldsymbol{A_i/O}} = \boldsymbol{\omega_1} \times (H_B\hat{\boldsymbol{k}}) - L\dot{\hat{j}}_2$

d) $\dot{\boldsymbol{r}}_{\boldsymbol{A_i/O}} = \boldsymbol{\omega_2} \times (H_B\hat{\boldsymbol{k}}) + L\dot{\hat{j}}_2$

where,

$$\boldsymbol{r}_{\boldsymbol{A_i/C_i}} = H\hat{\boldsymbol{k}}_{\boldsymbol{2}}. \tag{5.5}$$

and H_B is the radius of the spherical surface of the feet.

The $\hat{\boldsymbol{k}}$-direction of the rolling constraint is holonomic and when integrate for each state is:

a) $Z = H\cos\phi$

b) $Z = H\cos\phi$

c) $Z = H_B - L\sin\phi$

d) $Z = H_B + L\sin\phi$

5.2.6 Energy Definitions

Now that the position vectors have been fully defined, the Lagrangian can be derived. We start with the different types of energy. First, we have translational kinetic energy:

$$T_t = \frac{1}{2}(m_A\ \dot{\boldsymbol{r}}_{\boldsymbol{G_A/O}} \cdot \dot{\boldsymbol{r}}_{\boldsymbol{G_A/O}} + m_B\ \dot{\boldsymbol{r}}_{\boldsymbol{G_B/O}} \cdot \dot{\boldsymbol{r}}_{\boldsymbol{G_B/O}} + m_C\ \dot{\boldsymbol{r}}_{\boldsymbol{G_C/O}} \cdot \dot{\boldsymbol{r}}_{\boldsymbol{G_C/O}}) \tag{5.6}$$

where, m_A, m_B, and m_C are the masses of the two legs and the shaft body, respectively. Next, the rotational kinetic energy:

$$T_r = \frac{1}{2}(\boldsymbol{\omega_1^T}[\boldsymbol{R_3}]^{\boldsymbol{T}}\boldsymbol{I_1}[\boldsymbol{R_3}]\boldsymbol{\omega_1} + \boldsymbol{\omega_2^T}[\boldsymbol{R_4}]^{\boldsymbol{T}}\boldsymbol{I_2}[\boldsymbol{R_4}]\boldsymbol{\omega_2} + \boldsymbol{\omega_3^T}[\boldsymbol{R_2}]^{\boldsymbol{T}}\boldsymbol{I_3}[\boldsymbol{R_2}]\boldsymbol{\omega_3}) \tag{5.7}$$

where, $\boldsymbol{I_1}$ is the inertia matrix of Leg-A with respect to $\{\boldsymbol{\hat{x}_3}, \boldsymbol{\hat{y}_3}, \boldsymbol{\hat{z}_3}\}$, $\boldsymbol{I_2}$ is the inertia matrix of Leg-B with respect to $\{\boldsymbol{\hat{x}_4}, \boldsymbol{\hat{y}_4}, \boldsymbol{\hat{z}_4}\}$, $\boldsymbol{I_3}$ is the inertia matrix of the Shaft Body with respect to with respect to $\{\boldsymbol{\hat{x}_2}, \boldsymbol{\hat{y}_2}, \boldsymbol{\hat{z}_2}\}$, and the rotation matrices are defined below:

$$\begin{aligned}
[\boldsymbol{R_2}] &= \begin{bmatrix} \boldsymbol{\hat{\imath}_2^T} \\ \boldsymbol{\hat{\jmath}_2^T} \\ \boldsymbol{\hat{k}_2^T} \end{bmatrix} \\
[\boldsymbol{R_3}] &= \begin{bmatrix} \boldsymbol{\hat{\imath}_3^T} \\ \boldsymbol{\hat{\jmath}_3^T} \\ \boldsymbol{\hat{k}_3^T} \end{bmatrix} \\
[\boldsymbol{R_4}] &= \begin{bmatrix} \boldsymbol{\hat{\imath}_4^T} \\ \boldsymbol{\hat{\jmath}_4^T} \\ \boldsymbol{\hat{k}_4^T} \end{bmatrix} .
\end{aligned} \tag{5.8}$$

Finally, the potential energy of the system:

$$V = g(m_A \boldsymbol{r_{G_A/O}} + m_B \boldsymbol{r_{G_B/O}} + m_C \boldsymbol{r_{G_C/O}}) \cdot \boldsymbol{\hat{K}}. \tag{5.9}$$

The Lagrangian can be written as:

$$\mathcal{L} = T_t + T_r - V, \tag{5.10}$$

5.2.7 Constraint Forces

The constrained generalized coordinates for the system are:

$$\boldsymbol{q} = \{\theta_1, \theta_2, \phi, \psi, x, y\}. \tag{5.11}$$

As a result of the rolling velocity constraint, there are two constraint forces $\{r_x, r_y\}$. These forces interact with the system through generalized forces and moments (Q_{ic}):

$$\begin{aligned}
Q_{1c} &= -(a\ H + c\ H_B \cos\phi)(r_x \cos\psi + r_y \sin\psi) \\
Q_{2c} &= -(b\ H + d\ H_B \cos\phi)(r_x \cos\psi + r_y \sin\psi) \\
Q_{3c} &= (r_y \cos\psi - r_x \sin\psi(H(a+b)\cos\phi + H_B(c+d) + L(d-c)\sin\phi) \\
Q_{4c} &= (r_x(-\cos\psi) - r_y \sin\psi)(H(a+b)\sin\phi + L(c-d)\cos\phi) \\
Q_{5c} &= r_x \\
Q_{6c} &= r_y
\end{aligned} \tag{5.12}$$

There are two types of external loads. The first type of external load is friction. There is rolling friction between the feet and the platform [108]:

$$\begin{aligned} Q_{1r} &= -c_{r1} sgn(\dot{\theta}_1) \\ Q_{2r} &= -c_{r1} sgn(\dot{\theta}_2) \\ Q_{3r} &= -c_{r2} sgn(\dot{\phi}) \\ Q_{4r} &= -c_{r2} sgn(\dot{\psi}) \end{aligned} \tag{5.13}$$

where, c_{ri} is the rolling coefficient for the respective dynamics.

The model also includes the normal force between the foot and the platform, but this normal force varies insignificantly and can be assumed to be constant.

The damping friction term is:

$$\begin{aligned} Q_{1f} &= -c_{f1}\dot{\theta}_1 \\ Q_{2f} &= -c_{f1}\dot{\theta}_2 \end{aligned} \tag{5.14}$$

where, c_{fi} is the damping coefficient for the respective dynamics. The damping friction of θ_i is the result of the constraint forces between the legs and the Shaft Body.

5.2.8 Magnetic Moment

The active control of Big Foot is achieved through an arbitrary uniform magnetic field [101]. The magnetic field is generated with 3 sets of orthogonal Helmholtz coils. The magnetic field produced by in the inner set of coils is shown in Fig. 5.6. The yellow rectangle represents the foam platform the experiments are run on. After calibration, the magnetic field can be represented by a vector $p_m\boldsymbol{\hat{j}_m}$, where p_m is the power level of the field and $\boldsymbol{\hat{j}_m}$ is the y-direction of the coordinate frame as defined below:

$$\boldsymbol{\{\hat{i}_m, \hat{j}_m, \hat{k}_m\}} = [\boldsymbol{R_x}(\boldsymbol{\phi_m})][\boldsymbol{R_z}(\boldsymbol{\psi_m})]\boldsymbol{\{\hat{i}, \hat{j}, \hat{k}\}} \tag{5.15}$$

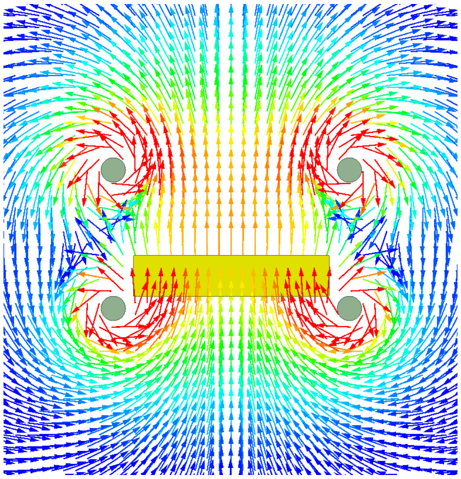

Figure 5.6: Cross-section view of magnetic field generated by the inner Helmholtz coils.

Once the magnetic field has been created, the magnet in Big Foot interacts with the field with the following magnetic moment equation:

$$\boldsymbol{\tau_m} = (k_m \boldsymbol{\hat{j}_2}) \times (p_m \boldsymbol{\hat{j}_m}) \tag{5.16}$$

where, k is a magnet strength coefficient found through tuning the model to experimental results.

Next, to find the applied load of the magnetic moment on the shaft assembly's generalized coordinates, the moment is projected on each coordinate's rotation axis:

$$\begin{aligned} Q_{3m} &= \boldsymbol{\tau_m}.\boldsymbol{\hat{i}_1} = k_m p_m (\sin\phi_m \cos\phi - \cos\phi_m \sin\phi \cos(\psi_m - \psi)) \\ Q_{4m} &= \boldsymbol{\tau_m}.\boldsymbol{\hat{k}} = k_m p_m \cos\phi_m \cos\phi \sin(\psi_m - \psi) \end{aligned} \tag{5.17}$$

Finally, using the Lagrangian method, the equations of motion for Big Foot are:

$$\begin{aligned}
\frac{d}{dt}\Big(\frac{\partial \mathcal{L}}{\partial \dot{\theta}_1}\Big) - \frac{\partial \mathcal{L}}{\partial \theta_1} &= Q_{1c} + (a+c)\ Q_{1r} + Q_{1f} \\
\frac{d}{dt}\Big(\frac{\partial \mathcal{L}}{\partial \dot{\theta}_2}\Big) - \frac{\partial \mathcal{L}}{\partial \theta_2} &= Q_{2c} + (b+d)\ Q_{2r} + Q_{2f} \\
\frac{d}{dt}\Big(\frac{\partial \mathcal{L}}{\partial \dot{\phi}}\Big) - \frac{\partial \mathcal{L}}{\partial \phi} &= Q_{3c} + Q_{3r} + Q_{3m} \\
\frac{d}{dt}\Big(\frac{\partial \mathcal{L}}{\partial \dot{\psi}}\Big) - \frac{\partial \mathcal{L}}{\partial \psi} &= Q_{4c} + Q_{4r} + Q_{4m} \\
\frac{d}{dt}\Big(\frac{\partial \mathcal{L}}{\partial \dot{x}}\Big) - \frac{\partial \mathcal{L}}{\partial x} &= Q_{5c} \\
\frac{d}{dt}\Big(\frac{\partial \mathcal{L}}{\partial \dot{y}}\Big) - \frac{\partial \mathcal{L}}{\partial y} &= Q_{6c}
\end{aligned} \tag{5.18}$$

.

5.2.9 Impact Map

Every time Big Foot switches stance legs, there is an impact. This impact has been observed through a loss of kinetic energy and audible sound produced.

Hurmuzlu writes that the Lagrangian formalism for impact problems can be written as [112]:

$$\left[\frac{\partial T}{\partial \dot{q}_i}\right]^{+} - \left[\frac{\partial T}{\partial \dot{q}_i}\right]^{-} - \hat{Q}_i - \sum_{K}^{j=1} \lambda_j \frac{\partial \psi_j}{\partial \dot{q}_i} = 0 \quad i = 1, 2, ..., N+2 \tag{5.19}$$

where, T is the total kinetic energy, the superscripts $-$ and $+$ correspond to the states immediately before and after impact, respectively, $\partial \dot{q}_i$ is the ith generalized velocity, $\hat{Q}_i$ is the generalized impulse in the direction of the ith generalized coordinate, and ψ_j and λ_j are the jth constraint and the corresponding Lagrange multiplier, respectively.

In using this impact model, once $\left[\frac{\partial T}{\partial \dot{q}_i}\right]^{+}$ and $\left[\frac{\partial T}{\partial \dot{q}_i}\right]^{-}$ are evaluated, the velocity constraints are substituted back in. This eliminates the constrained coordinates from the impact model and simplifies the map. Also, to model the movement of the foot/platform contact point of the pre-impact stance leg, the generalized coordinates are expanded as follows:

$$\boldsymbol{q_{impacts}} = \{\theta_1, \theta_2, \phi, \psi, c_x, c_y, c_z\}. \tag{5.20}$$

The position of these contact points is incorporated by defining the velocity constraint at impact as:

$$\dot{\boldsymbol{r}}_{\boldsymbol{A_i/O}} = \dot{\boldsymbol{c}}_i + a(\boldsymbol{\omega_1} \times \boldsymbol{r}_{\boldsymbol{A_A/C_A}}) + b(\boldsymbol{\omega_2} \times \boldsymbol{r}_{\boldsymbol{A_B/C_B}}) \tag{5.21}$$

where, $\dot{\boldsymbol{c}}_i$ is the velocity of point c_i and state a is used when the stance leg switches from Leg-a to Leg-b and visa versa.

The generalized impulse, $\hat{Q}_i$, is found as:

$$\begin{aligned}
Q_{1c} &= (a-b)H(\tau_x \cos\psi + \tau_y \sin\psi) \\
Q_{2c} &= (b-a)H(\tau_x \cos\psi + \tau_y \sin\psi) \\
Q_{3c} &= 2(a-b)L\ \tau_z \\
Q_{4c} &= -2(a-b)L(\tau_x \cos\psi + \tau_y \sin\psi) \\
Q_{5c} &= \tau_x \\
Q_{6c} &= \tau_y \\
Q_{7c} &= \tau_z
\end{aligned} \tag{5.22}$$

where, τ_i is the contact impulses at the striking foot and ϕ is set equal to 0 because this is the stance switching angle.

Finally, we have a set of equations to solve. There is the Lagrangian formalization from Equ. 5.19 with the generalized impulses in Equ. 5.22 and the substituted impact velocity constraints in Equ. 5.21. Next, There are post- and pre-impact velocity constraints. Before impact, the contact point on the stance leg is static, meaning:

$$\dot{\boldsymbol{c}}^- = 0 \tag{5.23}$$

After impact, the post-impact stance contact point is static. This is reprsented kinematically as:

$$\begin{aligned}
\dot{c}_x^+ &= -\Big((a-b)\cos\psi\big(H\dot{\theta}_1^+ - H\dot{\theta}_2^+ - 2L\dot{\psi}^+\big)\Big) \\
\dot{c}_y^+ &= (a-b)\sin\psi\big(-H\dot{\theta}_1^+ + H\dot{\theta}_2^+ + 2L\dot{\psi}^+\big) \\
\dot{c}_z^+ &= 2L(b-a)\dot{\phi}^+
\end{aligned} \tag{5.24}$$

This post impact constraint comes from assuming the coefficient of restitution is 0. Next, these equations are fed into a numerical solver and the post-impact velocities can be found through the solution. This solution is called the impact map.

Once the equations of motion and the impact map has been derived, the system can be simulated.

5.3 Actuation Scheme

The actuation scheme of Big Foot is based on impulsive locomotion. The applied impulse has four control parameters:

- ϕ_m: This is the yaw angle of the magnetic field vector.
- ψ_m: This is the roll angle of the magnetic field vector.
- P_L: This is the time duration of the applied pulse.
- P_m: This is the intensity of the applied magnetic field.

The rotational impulse acting on the biped by this magnetic field is defined as:

$$I_m = \int_{t_i}^{t_i+P_L} ||\boldsymbol{\tau_m}||\, dt \tag{5.25}$$

where, t_i is the time of heel strike. In impact dynamics, impulses are considered instantaneous and are independent of time. We investigate the boundary between considering the impulse to be instantaneous, to which $||\boldsymbol{\tau_m}||$ is constant, and the impulse being dependent on time. To make this comparison, we will define a constant impulse, I_c, corresponding to a practically instantaneous control:

$$I_c = ||\boldsymbol{\tau_m}||P_L \tag{5.26}$$

with I_c, regimes can be defined that correspond to the interaction of the input magnetic field with the dynamical response.

- Impact regime (Very Short Pulse Duration): During this regime, the generalized coordinates and velocities remain constant during application of the magnetic torque. Thus, the applied magnetic torque has a similar effect to that of an external impact.

- Impulsive regime (Moderate Pulse Duration): During this regime, the generalized coordinates and velocities change significantly during the application of the magnetic torque. Thus, the applied magnetic torque cannot be characterized as an external impact.

Responses illustrating these regimes are shown in Figs. 5.7

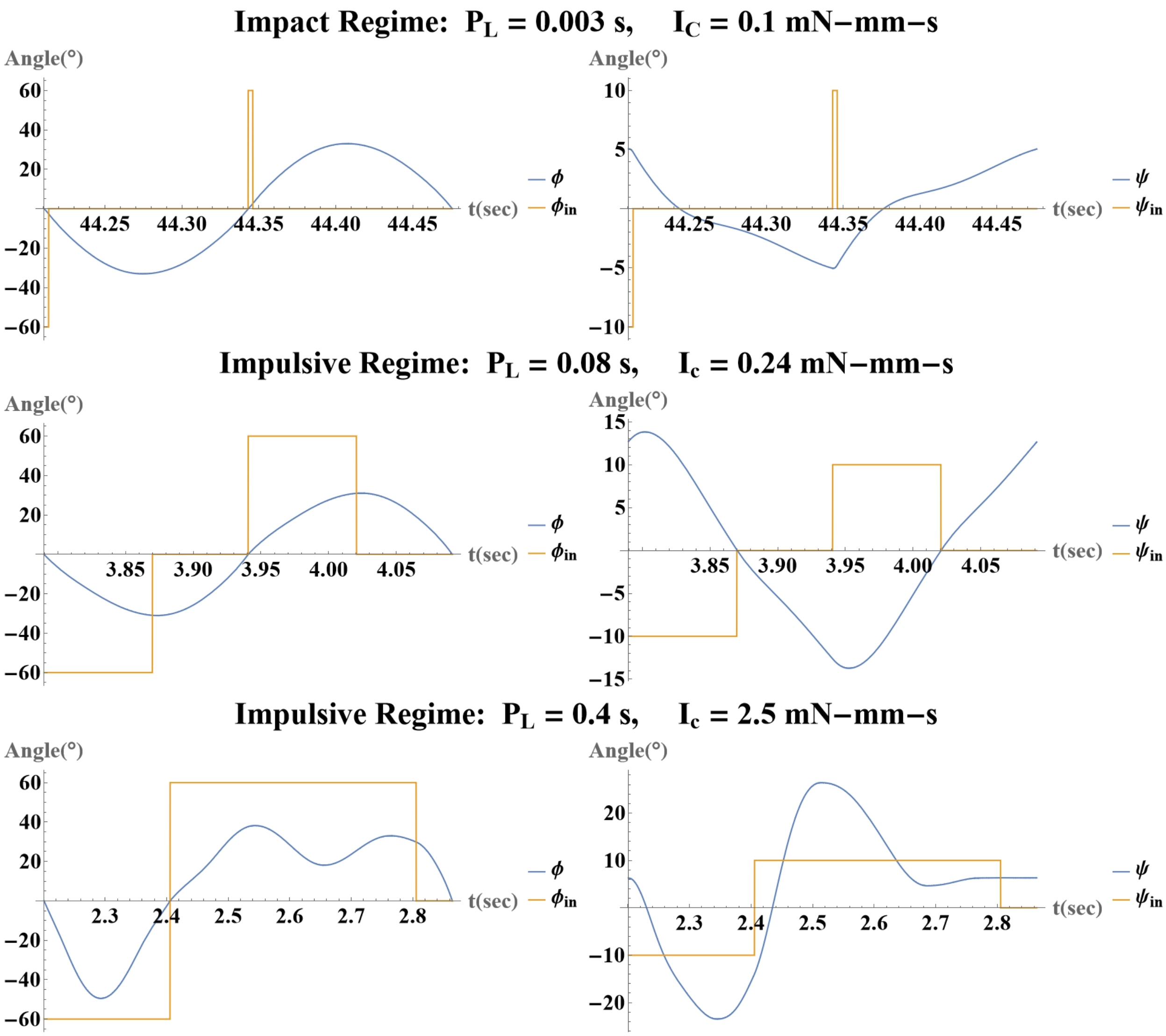

Figure 5.7: Input Regimes.
$\{\phi_m = 60°, \psi_{in} = 10°\}$.

Two actuation schemes will be studied. The first scheme is based on triggering the pulse every time Big Foot has a heel strike:

$$\phi[t] = \begin{cases} \phi_{in} & \phi > 0 \\ -\phi_{in} & \phi < 0 \end{cases}, \tag{5.27}$$

$$\psi[t] = \begin{cases} \psi_{in} & \phi > 0 \\ -\psi_{in} & \phi < 0 \end{cases}, \text{ and} \tag{5.28}$$

$$P_m = \begin{cases} P_{in} & t_s < t < t_s + P_L \\ 0 \end{cases} \tag{5.29}$$

where, t_s is the time of heel strike. An example run of this foot strike actuation is shown in Fig. 5.7.

The second actuation scheme is completely open-loop and is simply a pattern of periodically applied pulses:

$$\phi_m = \begin{cases} \phi_{in} & 0 < \mathrm{mod}(t, t_4) < t_1 \\ -\phi_{in} & t_2 < \mathrm{mod}(t, t_4) < t_3 \end{cases}, \tag{5.30}$$

$$\psi_m = \begin{cases} \psi_{in} & 0 < \mathrm{mod}(t, t_4) < t_1 \\ -\psi_{in} & t_2 < \mathrm{mod}(t, t_4) < t_3 \end{cases}, \text{ and} \tag{5.31}$$

$$P_m = \begin{cases} P_{in} & (0 < \mathrm{mod}(t, t_4) < t_1) || (t_2 < \mathrm{mod}(t, t_4) < t_3) \\ 0 \end{cases} \tag{5.32}$$

where, $t_1 = P_L$, $t_2 = P_L + t_{off}$, $t_3 = 2P_L + t_{off}$, $t_4 = 2P_L + 2t_{off}$, and t_{off} is the time period that the pulse is turned off.

An example run of this constant pulse wave actuation is shown in Fig. 5.8.

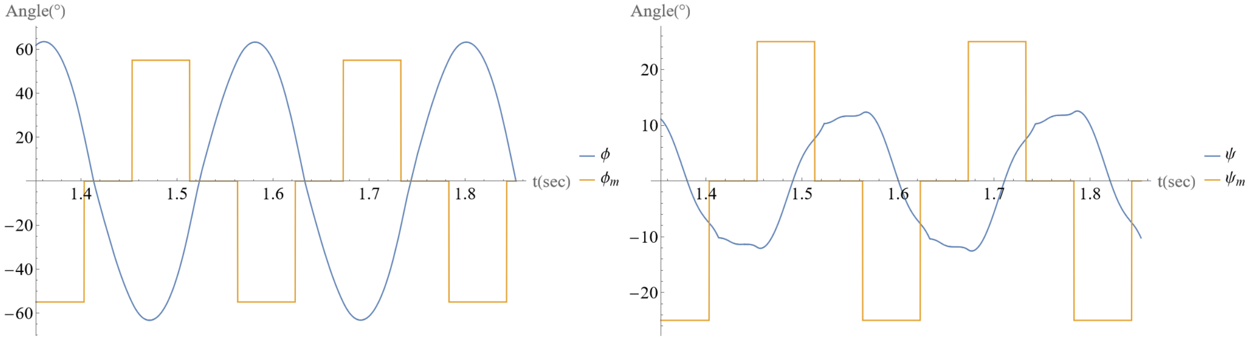

Figure 5.8: constant pulse wave actuation example.
$\{\phi_m = 35°, \psi_m = 15°, P_L = 0.06 \text{ s}, P_m = 48.2\%, t_{off} = 0.05 \text{ s}, I_c = 0.55 \text{ mN-mm-s}\}$.

In Figs. 5.7 and 5.8, the plots show the steady state response. Notice the timing between the heel strike and the switching of the input pulse. For the heel strike actuation, as enforced by the magnetic torque input, the heel strike and the input pulse are synchronous. But, for the constant pulse wave, the pulse does not necessarily initiate at the heel strike. This shows how the gait pattern can be initiated without the syncing of the pulse wave and the heel strike.

The selection of actuation parameters depend on the desired gait characteristics. Next, we explore the effect of the input parameters on the resulting gait patterns.

Chapter 6

Results of Big Foot

6.1 Simulations

The simulations were conducted using Wolfram Research Mathematica software. In the next subsections we present the simulation results.

6.1.1 Heel Strike Scheme Simulation Results

In Fig. 6.1, the results of the simulations for the heel strike actuation scheme are shown. The results are composed of 3 sets of different P_L values:$\{5\text{ ms}, 22.5\text{ ms}, 40\text{ ms}\}$. In each set, a set of 5 pulse areas were used:$\{2\ \%\text{ms}, 4\ \%\text{ms}, 6\ \%\text{ms}, 8\ \%\text{ms}, 10\ \%\text{ms}\}$. Pulse area is defined as:

$$P_{Area} = P_L \times P_m. \tag{6.1}$$

Other parameters used are $\{\phi_m = 60°, \psi_m = 20°\}$. The simulations began with running the model at a 0° slope for each P_{Area} until either a limit cycle was identified, a set amount of simulation time has passed, or locomotion is lost. Once the steady state locomotion was identified for a flat slope, the nature of the gait was added to the bifurcation map and the slope was increased by $1/2°$. The increase of slope continued until either the robot began walking backward or locomotion was lost. From the map, the maximum slope the robot can walk and the corresponding gait patterns has been identified.

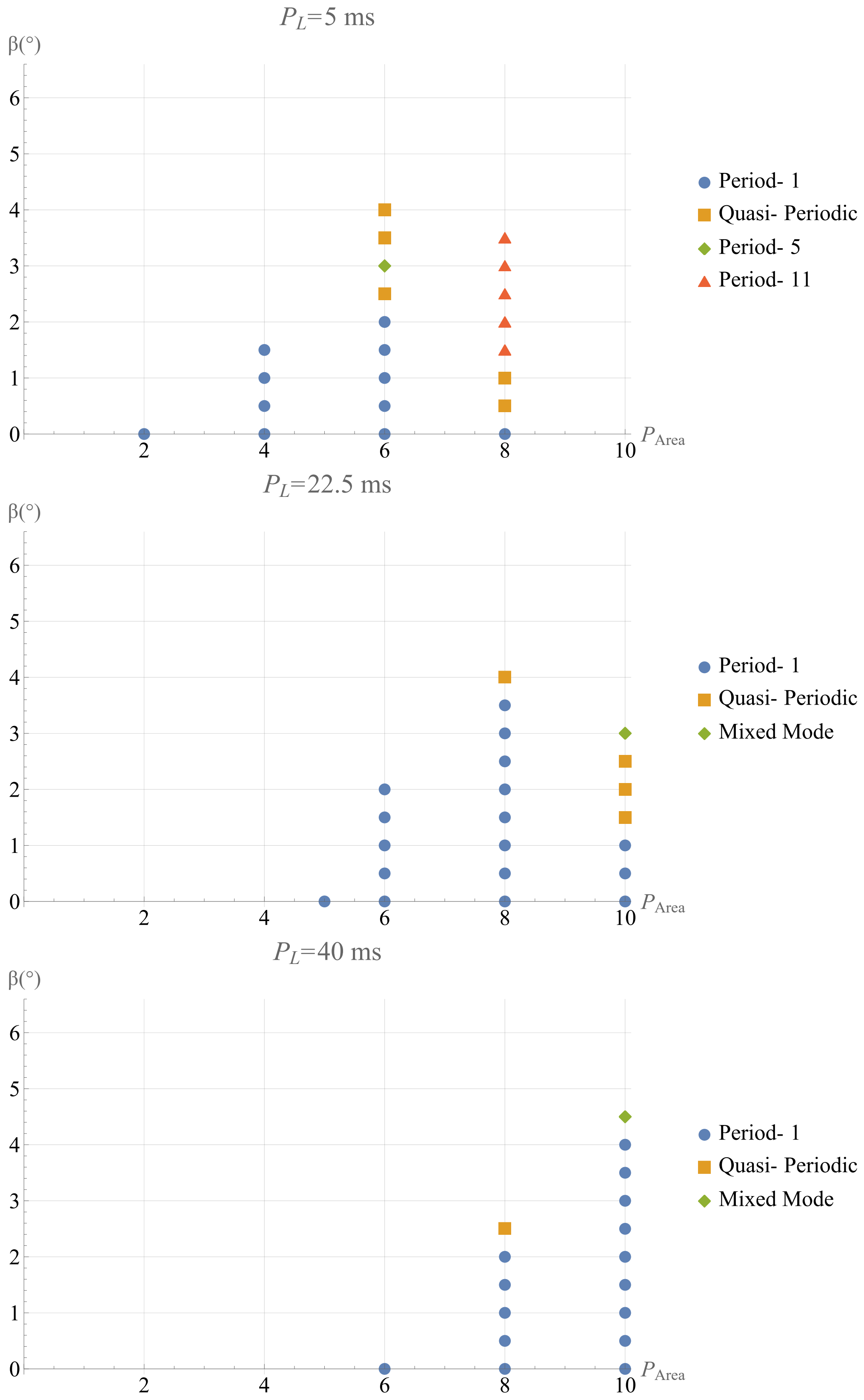

Figure 6.1: Heel Strike Actuation Scheme Bifurcation Map.

The purpose of this analysis is to identify the optimal operating region for Big Foot. We have chosen two goals for locomotion. The first goal is the desired to walk the steepest slope. Based on our results, longer pulse lengths with higher pulse areas is best. In our runs, a maximum slope of 4.5° at a pulse length of 40 ms was achieved. The second goal is to walk the steepest slope with a period-1 gait. This occured at 4° at a pulse length of 40 ms, also. The period-1 gait is useful for controllability as the displacement per step is constant.

Some overall trends in the results were observed as well. Quasi-Periodic gaits were observed as, while increasing the slope, the gait transitioned from one periodic gait to another. In Fig. 6.2, the Poincaré return map for ψ on a Quasi-Periodic orbit is show as an example. For $P_L = 5$ ms and $P_L = 22.5$ ms, the bifurcation plot is triangular. The peak of these triangles is the result of the intersection of two conditions. First, the maximum slope in pulse areas less that the peak occured when the robot started walking backward at the maximum slope. After the peak, the robot becomes unstable and is limited by stability, not power.

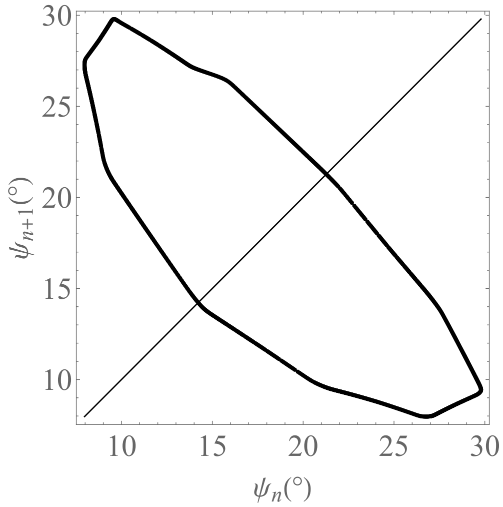

Figure 6.2: Poincaré Return Map for the yaw angle in a Quasi-Periodic gait.

6.1.2 Constant Pulse Wave Scheme Simulation Results

Next, simulations for the constant pulse wave actuation scheme were conducted. A bifurcation map of the same structure of Fig. 6.1 was setup for the constant pulse wave scheme. The results of this map are shown in Fig. 6.3. For this map, the same parameters of Fig. 6.1 with a $t_{off} = 60$ ms was chosen.

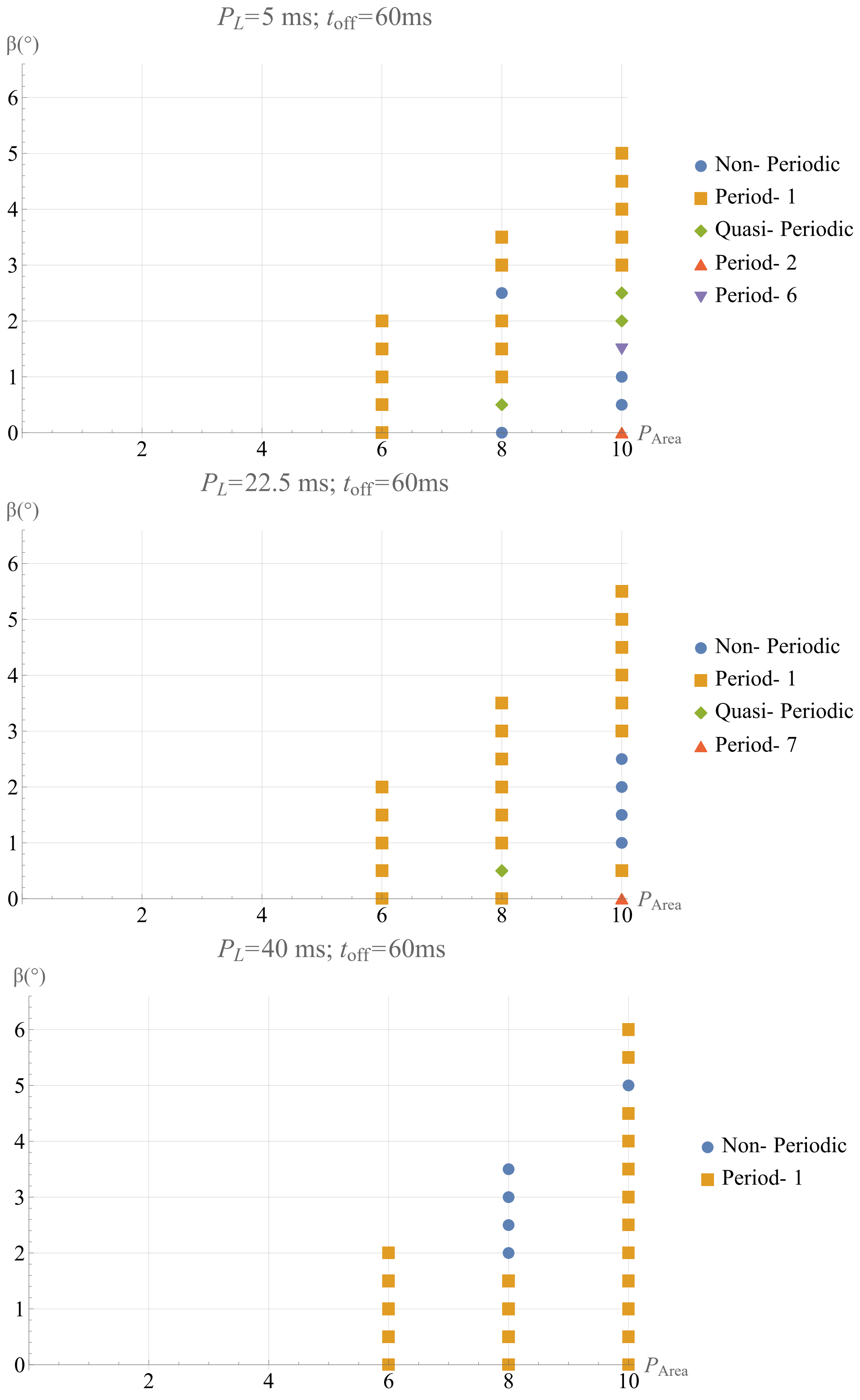

Figure 6.3: Constant Pulse Wave Actuation Scheme Bifurcation Map.

The difference in results of the heel strike scheme and the constant pulse wave scheme are as follows. The maximum slope achieved by the constant pulse wave scheme is significantly higher with 6° at $P_L = 40$ ms and $P_{Area} = 10$ %ms. Another difference is the generation of different periodic gaits. The heel strike scheme predictably performed period-1 gaits at lower slopes. Where as, the gait patterns of the constant pulse wave do not appear to be predictable from this study. For the constant pulse wave scheme a gait pattern called "Non-Periodic" was identified. "Non-Periodic" refers to a gait that appeared to have a random gait pattern and could not be classified as periodic or quasi-periodic. Another observation is that the performance did not vary greatly with different pulse lengths for the constant pulse wave, where it does for the heel strike. For the constant pulse wave, the robot was only operational in pulse areas 6 through 10 for all pulse lengths. For a control engineer, the heel strike appeared more desireable performance for period-1 gait, but the constant pulse wave scheme achieves much great slopes.

6.1.3 Stability Analysis

Let $\phi_p(t) = (\theta_1, \theta_2, \phi, \psi, \dot{\theta}_1, \dot{\theta}_2, \dot{\phi}, \dot{\psi}) \in \mathbb{R}^8$ be a periodic solution of Equ. 5.18 [114]. The one-sided hyper plane Poincaré section is defined as

$$\mathcal{S} \equiv (\theta_1, \theta_2, \psi, \dot{\theta}_1, \dot{\theta}_2, \dot{\phi}, \dot{\psi}) \in \mathbb{R}^7 : \phi = 0, \dot{\phi} < 0. \tag{6.2}$$

If $\boldsymbol{\xi}[k] \in \mathcal{S}$ denotes the kth intersection of $\mathcal{S}$ by the flow of ϕ_p, the discrete-time Poincaré Map $\mathcal{P} : \mathcal{S} \to \mathcal{S}$ can be expressed as

$$\boldsymbol{\xi}[k+1] = \mathcal{P}(\boldsymbol{\xi}[k]) \tag{6.3}$$

Subsequently, if $\boldsymbol{\xi}^*$ stands for a fixed point of the Poincaré Map, then the local exponential stability of $\boldsymbol{\xi}^*$ on $\mathcal{S}$ is equivalent to local exponential stability of the underlying limit cycle [113]. We used Floquet Theory for stability analysis of a specific limit cycle [49, 50]. Therefore, the local linearization of the Poincaré Map about $\boldsymbol{\xi}^*$ gives:

$$\begin{aligned}\mathcal{P}(\boldsymbol{\xi}) &\simeq \mathcal{J}(\boldsymbol{\xi}^*)(\boldsymbol{\xi}-\boldsymbol{\xi}^*)\\ \mathcal{J}(\boldsymbol{\xi}) &= \frac{\partial \mathcal{P}(\boldsymbol{\xi})}{\partial \boldsymbol{\xi}}\end{aligned} \tag{6.4}$$

where $\mathcal{J}(\boldsymbol{\xi})$ is the 7×7 linearized Jacobian matrix of $\mathcal{P}(\boldsymbol{\xi})$. Next, the floquet multipliers are defined as:

$$\rho_i = |Re(\lambda_i)| : \lambda_i = \text{eig}(\mathcal{J}(\boldsymbol{\xi})) \tag{6.5}$$

where ρ_i and λ_i are the ith floquet multiplier and eigenvalue of $\mathcal{J}(\boldsymbol{\xi})$. Accordingly, stability of the limit cycle can be defined as:

$$\phi_p(t) = \begin{cases}\text{stable :} & \forall \rho_i < 1\\ \text{unstable :} & \exists \rho_i \geq 1\end{cases} \tag{6.6}$$

A typical set of input parameters and platform slope were selected to study the stability of a period-1 limit cycle. These parameters are $\{\beta = 3°, \phi_{in} = 60°, \psi_{in} = 10°, P_L = 0.009 \text{ s}, P_m = 11.1 \text{ (mN-mm)}, I_c = 0.1 \text{ (mN-mm-s)}\}$. The control scheme selected was the Foot Strike Controller. The limit cycle is shown in the phase portraits of Fig. 6.4.

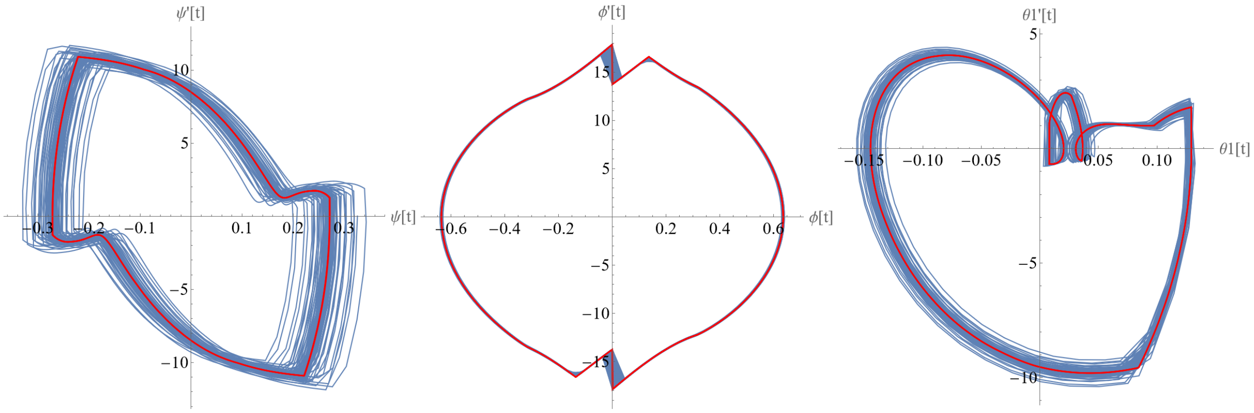

Figure 6.4: Period-1 Limit Cycle

The initial states of the run were all of the states on the fixed point $\mathcal{S}^*$, except the initial value for ψ was multiplied by 1.2. This selection will be explained after the Floquet multipliers are discussed.

To find the Floquet multipliers, the following algorithm was used:

```
define list $\boldsymbol{A} = \{\}$
for $n \in \mathcal{S}$ do
    $\mathcal{S}(0)_n = (1 + \delta)\mathcal{S}(0)_n$
    integrate for one cycle
    Join $\boldsymbol{A}$ and $\frac{\mathcal{S}^* - \mathcal{S}(t_f)}{\delta \mathcal{S}}$ to form a new $\boldsymbol{A}$, where $t_f$ is the final time of the cycle.
end
$\rho_i = |\mathrm{Re}(\mathrm{eig}(\boldsymbol{A})_i)|$
```

Algorithm 1: Floquet Multiplier Finder

One can fully determine the stability of the limit cycle by setting $\delta \rightarrow 0$. For the simulation run in Fig. 6.4, the maximum Floquet multiplier was found to be $\rho_1 = 0.92$. Next, the eigenvector corresponding to ρ_1 was evaluated. The element of the eigenvector with the largest real value magnitude was the third element, which corresponds to ψ. This means that ψ is the slowest state to converge to the limit cycle. This behavior was consistently observed in simulations and the convergence of ψ was used to identify when the system had converged on a limit cycle.

6.1.4 Constant Pulse Wave Off Time Parameter Variation

Next, the Constant Pulse Wave Input was applied to the model. Here, 1,101 simulations were run with an constant pulse wave frequency from 3.68 Hz to 6.17 Hz. In the simulations, the pulse length was held at 0.08s and the pulse off-time was varied. The results are shown in Fig. 6.5.

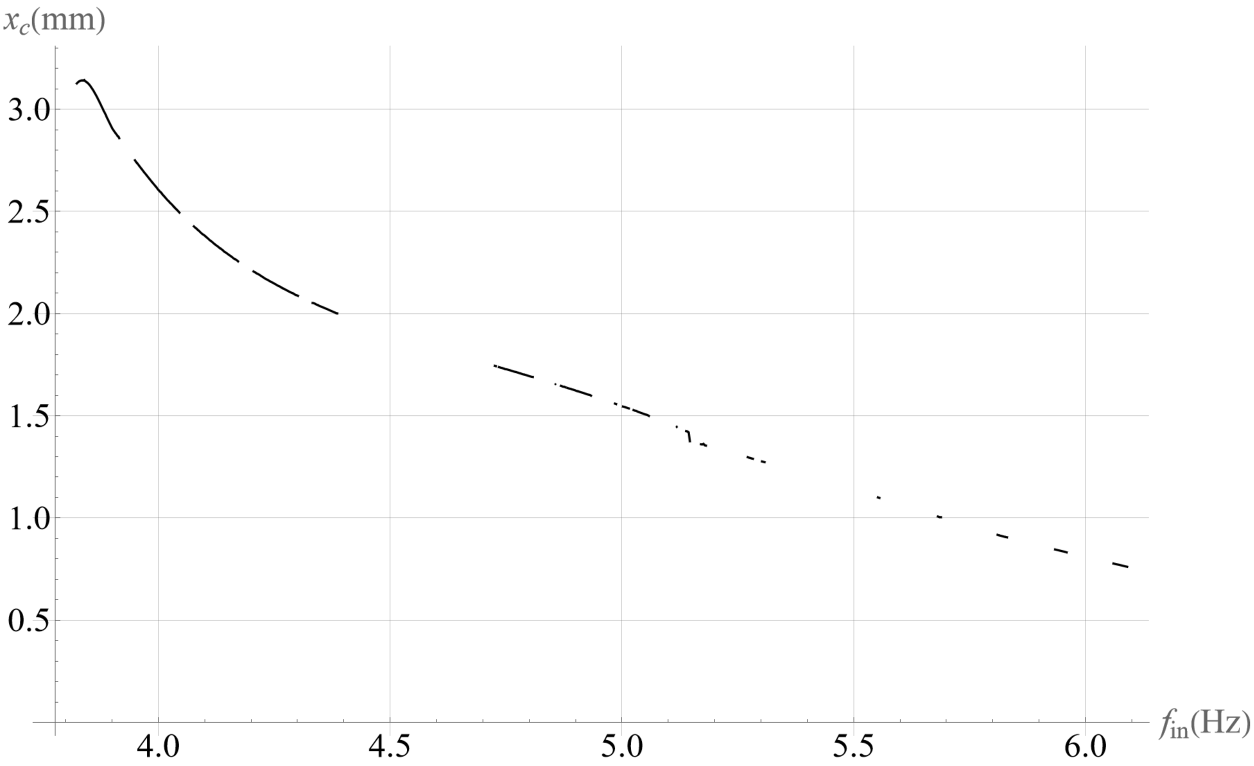

Figure 6.5: Simulation: Stride Length vs. Input Frequency.
$\{\beta = 0°, \phi_m = 55°, \psi_m = 25°, I_c = 0.2 \text{ (mN-mm-s)}, P_m = 13.2\%\}$

In Fig. 6.5, there are segments of the curve that are missing. The empty ranges are a result of off-times that cause a loss of limit cycles and zero locomotion. One can see that there exists a critical frequency that the stride length is at a maximum. This frequency is about 3.84 Hz. Including the critical frequency, three sample responses were chosen to investigate this behavior:

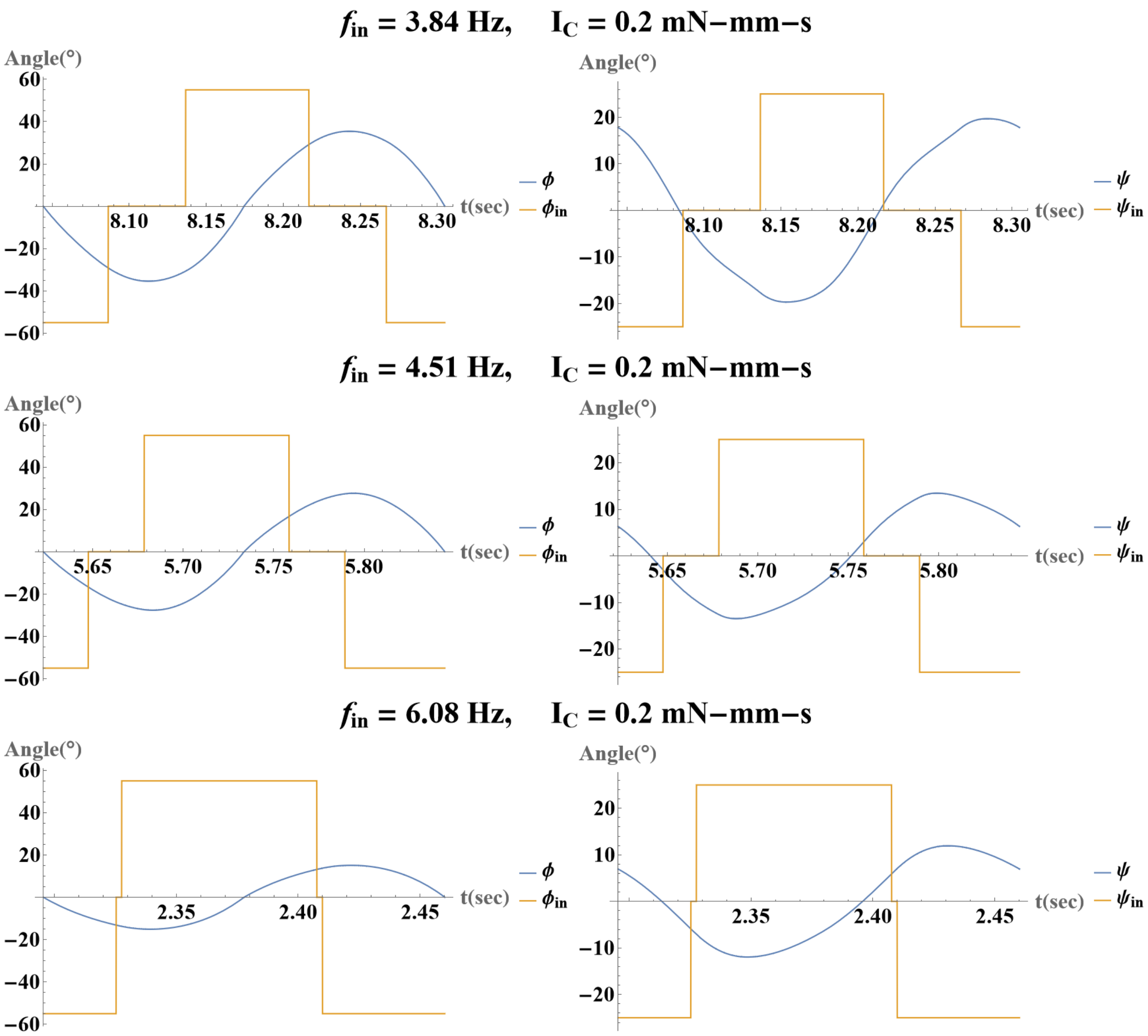

Figure 6.6: Sample Frequency Responses.

The responses in Fig. 6.6 show the interaction of input frequency with the responses. As the frequency decreases, the amplitude of ϕ and ψ increase. This corresponds to longer strides. Also, the increase in off-time allows for larger dynamics to be produced. Therefore, the power and time the magnetic field pulse is applied are both important.

6.2 Experimental Setup

The experimental setup includes 3 pairs of Helmholtz coils, a test platform, a light, a camera, an Arduino, a motor driver, and a PC. Helmholtz coils require two identical, parallel coils separated by a distance equal to their radius. Both coils are connected via wires such that their current flows in the same direction. A simple schematic of a single set Helmholtz coils is shown below in Fig. 6.7

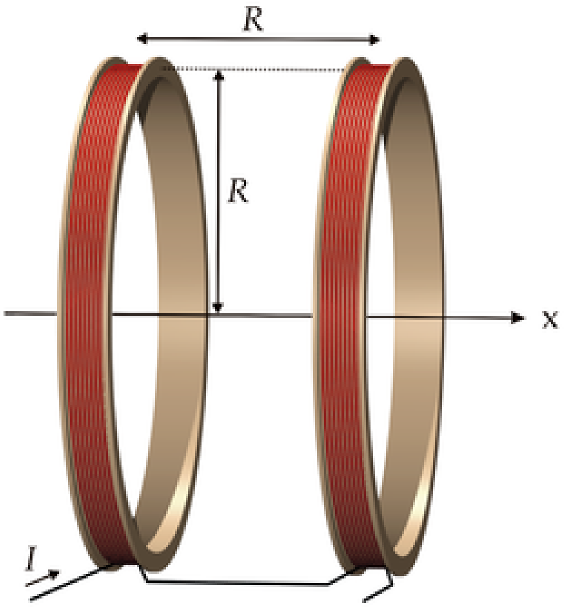

Figure 6.7: A single pair of Helmholtz Coils [3]

The experimental setup follows the outline set by Abbott [111] for nested circular coils that was used by Khatib et al. [101] as well. This involves three pairs of Helmholtz coils positioned orthogonally around a platform on which Big Foot moves, as pictured in Fig. 6.8

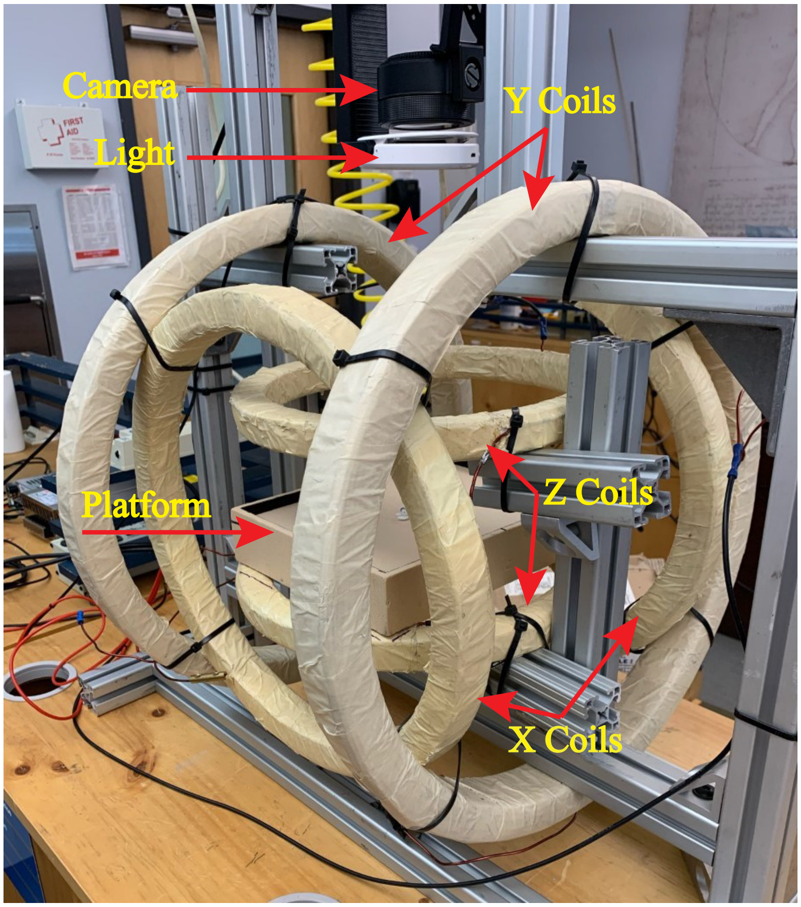

Figure 6.8: Experimental setup of three orthogonally positioned pairs of Helmholtz coils

The outer diameters of the y, x, and z coils are approximately 46 cm, 40 cm, and 31 cm respectively. The inner diameters are approximately 40 cm, 34 cm, and 25.5 cm and the coil thicknesses are approximately 4.47 cm, 3.61 cm, and 3.21 cm. The support structure was formed out of 80/20 aluminum T-slot building systems and the coils were further secured with Zip Ties. The platform was machined out of engineering foam, and a Ultra-Thin 10A durometer Silicone Rubber Sheet was placed on top of the platform's surface to prevent slipping. At the top of the setup a Razer (Irvine, California, USA) Kiyo Pro camera is secured with a Xinbaohong (Guangdong Province, China) XJ-19 Selfie Ring Light around it. The camera connected to a PC running Microsoft Visual Studio. The footage was recieved by a Python program that used OpenCV to collect data. The ring light was placed in front of the camera. Reflective tape was applied to the Shaft Body of Big Foot. This resulted in the light reflecting off of Big Foot and back to the camera. This setup greatly improved the quality of the data. Testing of various incline angles was done with the use of 3D printed ramps that hooked on the bottom z coil.

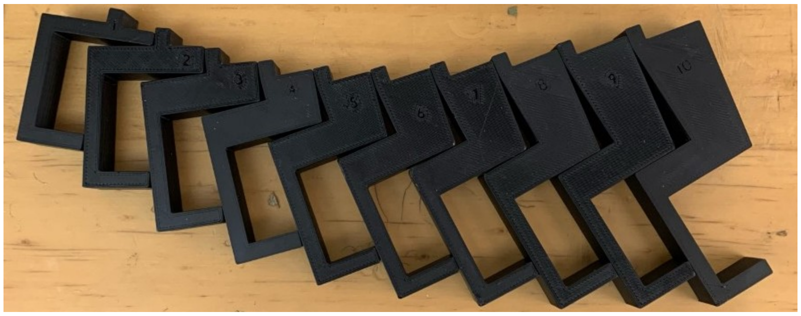

Figure 6.9: Ramps from 1° to 10° used to test at various inclines.

The approximately uniform magnetic fields caused by the three pairs of coils induce torques, as briefly noted in Equ. 5.16. The input control of the coils contains three variables that are the attitude angles and power of the overall magnetic field created. These variables are: yaw (ψ_m), pitch (ϕ_m), and power (-1.00 and 1.00). The magnitude of the magnetic field can be calculated via the following equation:

$$B = \left(\frac{4}{5}\right)^{\frac{3}{2}} \frac{\mu_0 n I}{R} \tag{6.7}$$

where, B is the magnetic field measured in Tesla, n is the number of turns in the coils, I is the current measured in amperes, R is the radius of the coil measured in meters, and $\mu_0 = 4\pi \times 10^{-7}$ Tm/A is the permeability of free space. The circuit schematic for the setup is pictured in Fig. 6.10 below.

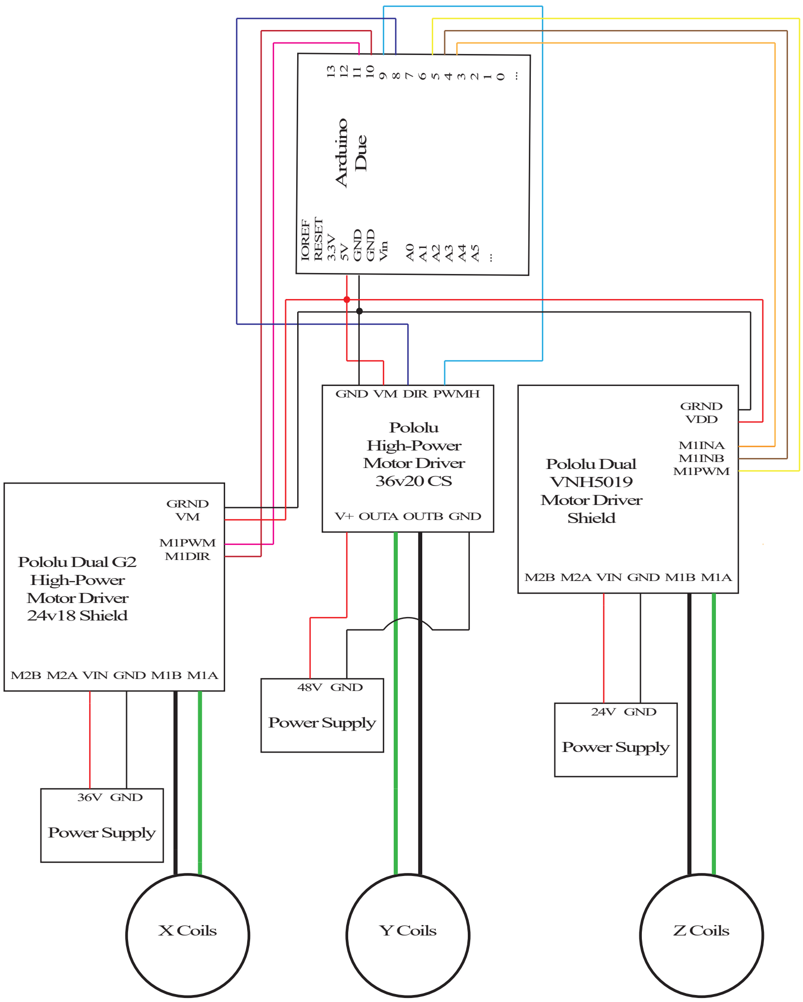
Arduino Due
13 12 11 10 9 8 7 6 5 4 3 2 1 0 ...
IOREF RESET 3.3V 5V GND GND Vin A0 A1 A2 A3 A4 A5 ...
GND VM DIR PWMH
Pololu High-Power Motor Driver 36v20 CS
V+ OUTA OUTB GND
GRND VDD M1INA M1INB M1PWM
Pololu Dual VNH5019 Motor Driver Shield
M2B M2A VIN GND M1B M1A
GRND VM M1PWM M1DIR
Pololu Dual G2 High-Power Motor Driver 24v18 Shield
M2B M2A VIN GND M1B M1A
48V GND
Power Supply
24V GND
Power Supply
36V GND
Power Supply
X Coils
Y Coils
Z Coils

Figure 6.10: Circuit schematic for the experimental setup

6.3 Experimental Results

6.3.1 Data Collection

The data for experiments was acquired through selecting a preset distance on the platform for Big Foot to travel. The distance selected was 210 mm. Big Foot was placed at one end of the platform. A quick alignment program was run to make sure Big Foot was directed along the experiment's path. Next, the constant pulse wave controller is turned on to generate locomotion in Big Foot. The Heel Strike Controller was not available for implementation in experiments as there was no way to have a sensor detecting the heel strikes to provide feedback. Next, Big Foot was run open loop until 1 of 3 conditions were satisfied. First, the pulse wave could be too strong, Big Foot would fall, and the program was terminated. Second, the slope was too steep or there was not enough power provided to create forward locomotion. Finally, a successful walk ended when Big Foot had traveled 210 mm across the platform. Upon the termination of the program, the MCU prints the number of cycles of pulses sent during the walk. Based on observation and simulation results, the number of steps taken is assumed to be identical to twice the number of pulse cycles sent. Next, by dividing the distance traveled by the number of steps, the stride length (x_c) of Big Foot was calculated. Stride length was the primary output measurement taken.

6.3.2 Parameter Variation: Platform Slope

The first set of experiments were carried out to see how Big Foot performs with different impulses at different platform slopes. The results are shown in Fig. 6.11.

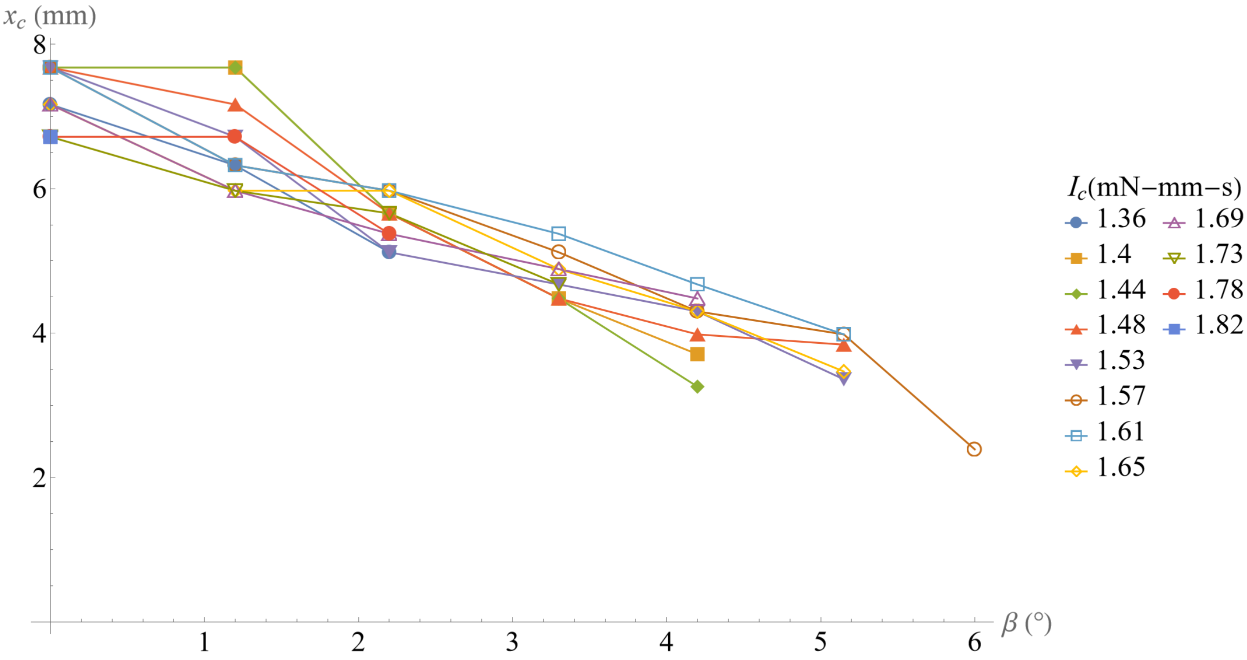

Figure 6.11: Experimental results of Big Foot stride length vs. Platform Slope. $\{\phi_m = 53^\circ, \psi_m = 25^\circ, P_L = 0.22\ \mathrm{s}, t_{off} = 0.046\ \mathrm{s}\}$.

The results show that the impulse does not have a significant effect on the stride length. This contrasts greatly with simulation results in Fig. **??** where the stride length variation can be a factor of 6 with different impulses. Also contrasting with the simulation, the magnitude of the impulses in experiments were approximately 10 times more. This is a result of the difference in pulse length. The pulse lengths in simulations were on the order of 0.01s. Operation of Big Foot in the impact regime was not achieved in experimentation as the setup was not fast enough to supply high frequencies. Also, the simulations run in Fig. **??** used the Heel Strike Actuation Scheme, where as Fig. 6.11 is with the Constant Pulse Wave Actuation Scheme. However, the big similarity between experiments and simulations is the curve of stride length with respect to the platform slope. Both curves are very linear.

6.3.3 Parameter Variation: Pulse Length

Finally, the input pulse length was varied to see its influence on dynamics. In Fig. 6.12, the results are shown.

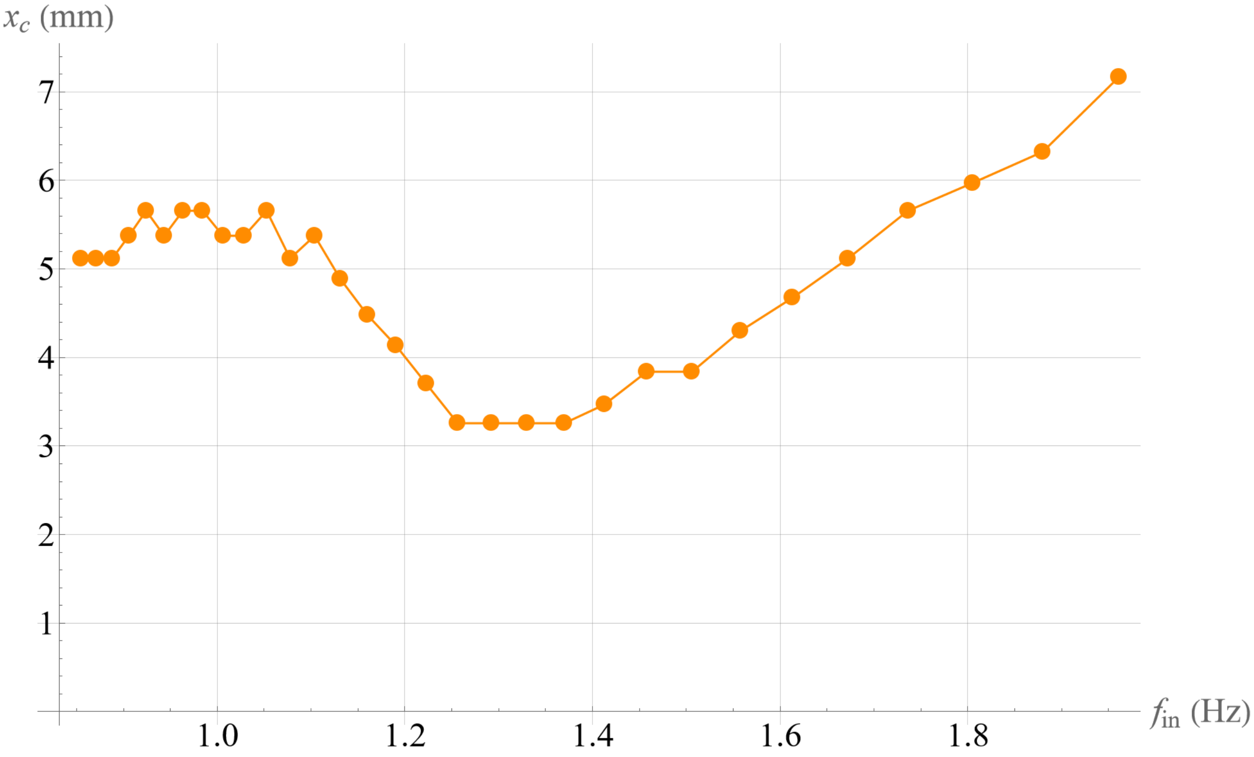

Figure 6.12: Experimental results of Big Foot input frequency vs. Platform Slope. $\{\phi_m = 53°, \psi_m = 20°, P_m = 33.8\%, t_{off} = 0.046 \text{ s}, \beta = 0°\}$.

This experiment shows the nonlinear nature of Big Foot. Initially, the stride length is invariant with respect to input frequency. However, as the frequency goes beyond 1.104 Hz, the relationship becomes parabolic. In observation, at this frequency, Big Foot never reaches steady state. So, beyond 1.104 Hz, the leg motions are different with respect to different frequencies. So, the foot placement at each step will be different. This leads to different stride lengths.

Chapter 7

Discussion and Conclusion

7.1 MoRIS

MoRIS is an aerospace tube network inspection system. It consists of a Base Station and Vertebrae. The design of MoRIS has been optimized to navigate inside tube networks. It can climb tube sections in all orientations, including vertical ones. The configuration space of the Locomotion Vertebrae has been presented. The resulting kinematics have been introduced. A localization algorithm has been developed and tested. The resulting localization function proved to be sufficiently accurate for practical use. Future work includes extending the analysis to tube bends and developing Vertebrae for different tube sizes. With tighter tolerances and higher manufacturing precision, it would be possible to decrease internal friction of the Locomotion Vertebra. This would allow for higher normal forces and would allow even greater performance. Higher power stepper motors would increase performance as well. Now that the basic prototype has been developed, it needs to be tested in real-world applications on the factory floors and assembly lines. A dynamical analysis would aid in understanding the performance of the Vertebrae. Also, the kinematical analysis was applied only to the Locomotion Vertebra. It should be applied to all of the Vertebrae combined. The tether reel should be developed further. Automating the reel will facilitate a simpler operation of the device. A longer tether would also expand the capability of the inspection system. Extending the tether length would necessitate longer camera cables, which was the limiting factor in the current design. All of these would improve the applicability of MoRIS to a wider range of industries and uses.

7.2 Big Foot

In this work, a novel impulsive walker was introduced. A physical prototype, Big Foot, was produced. The prototype is the smallest bipedal walker ever built and the first purely impulsive controlled robot built. A complete dynamical model was developed of Big Foot. The impulsive actuation scheme was shown. Both a heel strike actuation scheme and a constant pulse wave actuation scheme was tested. Testing was done both through simulations and experiments. Two regimes were found, corresponding to the characteristics of the magnetic moment impulse applied to Big Foot. It can be concluded that impact-like impulses and longer duration impulses can be used to create locomotion in bipedal walkers.

APPENDIX A

7.3 Localization Algorithm

```
$c_1$ = First Section Length
$\boldsymbol{F}_1$ = Space-Fixed Coordinates
$\boldsymbol{m}_1$ = Straight Tube Section Model
for All of $t_n$ do
    if Bent Section then
        $c_q$= Bent Tube Section Centerline Curve Arc-Length
        $\boldsymbol{F}_q$ = Frenet Coordinate System of the Bent Tube Section
        $\boldsymbol{m}_n$ = Tube Model of Bent Sector
    else
        $c_q$= Straight Tube Section Length
        $\boldsymbol{F}_q$ = Coordinate System of the Straight Tube Section
        $\boldsymbol{m}_n$ = Tube Model of Straight Section
    end
end
```

Algorithm 2: Setting up tube network model

```
$\boldsymbol{t}_{P1} = \{0,0,0\}$
$line = \boldsymbol{m}_2 - \boldsymbol{t}_{P1}$
$\boldsymbol{t}_{P2}$ = Solution of $(line.\boldsymbol{F}_2.\hat{\boldsymbol{e}}_{\boldsymbol{n}} = 0)$
for All of $t_n$ do
    $line = \boldsymbol{m}_{q+1} - \boldsymbol{m}_{q-1}$
    $\boldsymbol{t}_{Pq}$ and $\boldsymbol{t}_{Pq+1}$ = Solution to $(line.\boldsymbol{F}_{q+1}.\hat{\boldsymbol{e}}_{\boldsymbol{n}} = 0$ and $line.\boldsymbol{F}_{q-1}.\hat{\boldsymbol{e}}_{\boldsymbol{n}} = 0)$
end
$q$ = Size of $\boldsymbol{t}_n$
$\boldsymbol{t}_{Pq+1}$ = end of tube network center-line
$line = \boldsymbol{t}_{Pq+1} - \boldsymbol{m}_q$
$\boldsymbol{t}_{Pq}$ = Solution of $line.\boldsymbol{F}_{q-1}.\hat{\boldsymbol{e}}_{\boldsymbol{n}} = 0$.
```

Algorithm 3: Calculating tether contact points

```
for All of $t_n$ do
    $b_{q-1}$ = tether length solution to $((\boldsymbol{m}_q - \boldsymbol{t}_{Pq}).\boldsymbol{F}_q.\hat{\boldsymbol{e}}_{\boldsymbol{t}} = 0)$
    $b_q$ = tether length solution to $((\boldsymbol{m}_q - \boldsymbol{t}_{Pq+1}).\boldsymbol{F}_q.\hat{\boldsymbol{e}}_{\boldsymbol{t}} = 0)$
end
```

Algorithm 4: Calculating tether contact lengths

```
for All of $t_n$ do
    $t_{Crit0}$ = tether length position it switch from the previous bend radius to the straight taut length.
    $t_{Crit2}$ = tether length from entrance to touching the first bend.
    $t_{Crit1}$ = tether length position it crosses from the straight section to the bend.
    $t_{Crit3}$ = tether length position it switches from the bend's radius to the straight taut section.
    $r_q$ = the localization fuction from the previous $t_{Crit(q-1)}$ to the next $t_{Crit(q)}$.
end
```

Algorithm 5: Building localization function

BIBLIOGRAPHY

[1] G. L. Corporation, "Borescope origins: Where it all began," Aug 2021. [Online]. Available: https://www.gradientlens.com/borescope-origins-where-it-all-began/ ix, 2

[2] H. Choi and S.-g. Roh, *In-pipe Robot with Active Steering Capability for Moving Inside of Pipelines*, 09 2007. ix, 3, 4

[3] A. Hellwig, *Helmholtz coils*, Jun 2005. [Online]. Available: https://commons.wikimedia.org/wiki/File:Helmholtz_coils.png#filelinks xi, 68

[4] W. Griffioen and D. Plumettaz, "Cable pulling force in pipes with 3d bends for different installation methods," *Journal of Pipeline Systems Engineering and Practice*, vol. 12, no. 4, p. 04021060, 2021. 2

[5] J. Okamoto, J. C. Adamowski, M. S. Tsuzuki, F. Buiochi, and C. S. Camerini, "Autonomous system for oil pipelines inspection," *Mechatronics*, vol. 9, no. 7, pp. 731–743, 1999. [Online]. Available: https://www.sciencedirect.com/science/article/pii/S0957415899000318 4

[6] T. Okada and T. Kanade, "A three-wheeled self-adjusting vehicle in a pipe, ferret-1," *The International Journal of Robotics Research*, vol. 6, no. 4, pp. 60–75, 1987. [Online]. Available: https://doi.org/10.1177/027836498700600406 4

[7] S. Hirose, H. Ohno, T. Mitsui, and K. Suyama, "Design of in-pipe inspection vehicles for /spl phi/25, /spl phi/50, /spl phi/150 pipes," in *Proceedings 1999 IEEE International Conference on Robotics and Automation (Cat. No.99CH36288C)*, vol. 3, 1999, pp. 2309–2314 vol.3. 4

[8] M. Kolesnik, "Visual orientation in the sewer - adaptation to the environment," in *2002 International Conference on Pattern Recognition*, vol. 2, 2002, pp. 856–859 vol.2. 4

[9] K. Suzumori, K. Hori, and T. Miyagawa, "A direct-drive pneumatic stepping motor for robots: designs for pipe-inspection microrobots and for human-care robots," in *Proceedings. 1998 IEEE International Conference on Robotics and Automation (Cat. No.98CH36146)*, vol. 4, 1998, pp. 3047–3052 vol.4. 4

[10] T. Tsubouchi, S. Takaki, Y. Kawaguchi, and S. Yuta, "A straight pipe observation from the inside by laser spot array and a tv camera," in *Proceedings. 2000 IEEE/RSJ International Conference on Intelligent Robots and Systems (IROS 2000) (Cat. No.00CH37113)*, vol. 1, 2000, pp. 82–87 vol.1. 4

[11] K.-U. Scholl, V. Kepplin, K. Berns, and R. Dillmann, “Controlling a multi-joint robot for autonomous sewer inspection,” in *Proceedings 2000 ICRA. Millennium Conference. IEEE International Conference on Robotics and Automation. Symposia Proceedings (Cat. No.00CH37065)*, vol. 2, April 2000, pp. 1701–1706 vol.2. 4

[12] M. Muramatsu, N. Namiki, R. Koyama, and Y. Suga, “Autonomous mobile robot in pipe for piping operations,” in *Proceedings. 2000 IEEE/RSJ International Conference on Intelligent Robots and Systems (IROS 2000) (Cat. No.00CH37113)*, vol. 3, Oct 2000, pp. 2166–2171 vol.3. 4

[13] J. Ong, D. Kerr, and K. Bouazza-Marouf, “Design of a semi-autonomous modular robotic vehicle for gas pipeline inspection,” *Proceedings of the Institution of Mechanical Engineers, Part I: Journal of Systems and Control Engineering*, vol. 217, 03 2003. 4

[14] H. Choi and S. Ryew, “Robotic system with active steering capability for internal inspection of urban gas pipelines,” *Mechatronics*, vol. 12, no. 5, pp. 713–736, 2002. [Online]. Available: https://www.sciencedirect.com/science/article/pii/S0957415801000228 4

[15] S. Ryew, S. Baik, S. Ryu, K. Jung, S. Roh, and H. Choi, “In-pipe inspection robot system with active steering mechanism,” in *Proceedings. 2000 IEEE/RSJ International Conference on Intelligent Robots and Systems (IROS 2000) (Cat. No.00CH37113)*, vol. 3, Oct 2000, pp. 1652–1657 vol.3. 4

[16] S. Roh, S. Ryew, J. Yang, and H. Choi, “Actively steerable in-pipe inspection robots for underground urban gas pipelines,” in *Proceedings 2001 ICRA. IEEE International Conference on Robotics and Automation (Cat. No.01CH37164)*, vol. 1, May 2001, pp. 761–766 vol.1. 4

[17] S. gon Roh and H. Choi, “Strategy for navigation inside pipelines with differential-drive inpipe robot,” in *Proceedings 2002 IEEE International Conference on Robotics and Automation (Cat. No.02CH37292)*, vol. 3, May 2002, pp. 2575–2580 vol.3. 4

[18] S. gon Roh and H. R. Choi, “Differential-drive in-pipe robot for moving inside urban gas pipelines,” *IEEE Transactions on Robotics*, vol. 21, no. 1, pp. 1–17, Feb 2005. 4

[19] H. Schempf and G. Vradis, “Explorer: Long-range untethered real-time live gas main inspection system,” in *Proceedings - Natural Gas Technologies II: Ingenuity and Innovation*, 2004, proceedings - Natural Gas Technologies II: Ingenuity and Innovation ; Conference date: 08-02-2004 Through 11-02-2004. 4

[20] H. Schempf, E. Mutschler, V. Goltsberg, and W. Crowley, “Grislee: Gasmain repair and inspection system for live entry environments,” *International Journal of Robotics Research*, vol. 22, no. 8, pp. 603 – 616, July 2003. 4

[21] B. Gamble and R. Wiesman, “Tethered mouse system for inspection of gas distribution mains. final report, december 1992-october 1996,” 1996. 4

[22] H. Roman, B. Pellegrino, and W. Sigrist, “Pipe crawling inspection robots: an overview,” *IEEE Transactions on Energy Conversion*, vol. 8, no. 3, pp. 576–583, Sep. 1993. 4

[23] W. Neubauer, “A spider-like robot that climbs vertically in ducts or pipes,” in *Proceedings of IEEE/RSJ International Conference on Intelligent Robots and Systems (IROS’94)*, vol. 2, Sep. 1994, pp. 1178–1185 vol.2. 4

[24] F. Pfeiffer, T. Rossmann, and K. Loffler, “Control of a tube crawling machine,” in *2000 2nd International Conference. Control of Oscillations and Chaos. Proceedings (Cat. No.00TH8521)*, vol. 3, July 2000, pp. 586–591 vol.3. 4

[25] G. Kostin, F. Chernousko, N. Bolotnik, and F. Pfeiffer, “Regular motions of a tube-crawling robot: simulation and optimization,” in *Proceedings of the First Workshop on Robot Motion and Control. RoMoCo’99 (Cat. No.99EX353)*, June 1999, pp. 45–50. 4

[26] F. Nickols, D. Ho, S. Harrold, R. Bradbeer, and L. Yeung, “An ultrasonically controlled robot submarine for pipe inspection,” in *Proceedings Fourth Annual Conference on Mechatronics and Machine Vision in Practice*, Sep. 1997, pp. 142–147. 4

[27] T. Fukuda, H. Hosokai, and M. Uemura, “Rubber gas actuator driven by hydrogen storage alloy for in-pipe inspection mobile robot with flexible structure,” in *Proceedings, 1989 International Conference on Robotics and Automation*, May 1989, pp. 1847–1852 vol.3. 4

[28] Y. Kondoh and S. Yokota, “Micro in-pipe mobile machines by making use of an electro-rheological fluid,” in *Proceedings of the 1997 IEEE/RSJ International Conference on Intelligent Robot and Systems. Innovative Robotics for Real-World Applications. IROS ’97*, vol. 3, Sep. 1997, pp. 1672–1677 vol.3. 4

[29] C. Anthierens, C. Libersa, M. Touaibia, M. Betemps, M. Arsicault, and N. Chaillet, “Micro robots dedicated to small diameter canalization exploration,” in *Proceedings. 2000 IEEE/RSJ International Conference on Intelligent Robots and Systems (IROS 2000) (Cat. No.00CH37113)*, vol. 1, Oct 2000, pp. 480–485 vol.1. 4

[30] T. Shibata, T. Sasaya, and N. Kawahara, “Microwave energy supply system for in-pipe micromachine,” in *MHA’98. Proceedings of the 1998 International Symposium on Micromechatronics and Human Science. - Creation of New Industry - (Cat. No.98TH8388)*, 1998, pp. 237–242. 4

[31] K. Tsuruta, T. Sasaya, T. Shibata, and N. Kawahara, “Control circuit in an in-pipe wireless micro inspection robot,” in *MHS2000. Proceedings of 2000 International Symposium on Micromechatronics and Human Science (Cat. No.00TH8530)*, Oct 2000, pp. 59–64. 4

[32] L. Sun, P. Sun, L. Lian, X. Qin, and Z. Gong, "Improvement of characteristics of in-pipe micro robot," in *MHS'99. Proceedings of 1999 International Symposium on Micromechatronics and Human Science (Cat. No.99TH8478)*, Nov 1999, pp. 153–156. 4

[33] S. Landsberger and B. Martin, "The design of a pipe crawling robot for control of zebra mussel infestations," vol. 2, Oct 1992, pp. 819–824. 4

[34] A. Menciassi, J. Park, S. Lee, S. Gorini, P. Dario, and J.-O. Park, "Robotic solutions and mechanisms for a semi-autonomous endoscope," in *IEEE/RSJ International Conference on Intelligent Robots and Systems*, vol. 2, Sep. 2002, pp. 1379–1384 vol.2. 4

[35] N. Mitumoto, K. Tsuruta, T. Shibata, and N. Kawahara, "Wireless link system for communication and energy transmission of microrobot," in *MHS2001. Proceedings of 2001 International Symposium on Micromechatronics and Human Science (Cat. No.01TH8583)*, Sep. 2001, pp. 57–62. 4

[36] M. TAKAHASHI, I. HAYASHI, N. IWATSUKI, K. SUZUMORI, and N. OHKI, "The development of an in-pipe microrobot applying the motion of an earthworm," in *1994 5th International Symposium on Micro Machine and Human Science Proceedings*, Oct 1994, pp. 35–. 4

[37] A. Bertetto and M. Ruggiu, "In-pipe inch-worm pneumatic flexible robot," in *2001 IEEE/ASME International Conference on Advanced Intelligent Mechatronics. Proceedings (Cat. No.01TH8556)*, vol. 2, July 2001, pp. 1226–1231 vol.2. 4

[38] I. Hayashi and N. Iwatuki, "Micro moving robotics," in *MHA'98. Proceedings of the 1998 International Symposium on Micromechatronics and Human Science. - Creation of New Industry - (Cat. No.98TH8388)*, Nov 1998, pp. 41–50. 4

[39] H. Nishikawa, T. Sasaya, T. Shibata, T. Kaneko, N. Mitumoto, S. Kawakita, and N. Kawahara, "In-pipe wireless micro locomotive system," in *MHS'99. Proceedings of 1999 International Symposium on Micromechatronics and Human Science (Cat. No.99TH8478)*, Nov 1999, pp. 141–147. 4

[40] C. Anthierens, A. Ciftci, and M. Betemps, "Design of an electro pneumatic micro robot for in-pipe inspection," in *ISIE '99. Proceedings of the IEEE International Symposium on Industrial Electronics (Cat. No.99TH8465)*, vol. 2, July 1999, pp. 968–972 vol.2. 4

[41] I. Hayashi, N. Iwatsuki, and S. Iwashina, "The running characteristics of a screw-principle microrobot in a small bent pipe," in *MHS'95. Proceedings of the Sixth International Symposium on Micro Machine and Human Science*, Oct 1995, pp. 225–228. 4

[42] M. Horodinca, I. Doroftei, E. Mignon, and A. Preumont, "A simple architecture for in-pipe inspection robots," 06 2002. 4

[43] S. Iwashina, I. Hayashi, N. Iwatsuki, and K. Nakamura, “Development of in-pipe operation micro robots,” in *1994 5th International Symposium on Micro Machine and Human Science Proceedings*, Oct 1994, pp. 41–. 4

[44] A. Kakogawa, T. Nishimura, and S. Ma, “Designing arm length of a screw drive in-pipe robot for climbing vertically positioned bent pipes,” *Robotica*, vol. 34, pp. 1–22, 01 2014. 4

[45] A. Kakogawa, S. Ma, and S. Hirose, “An in-pipe robot with underactuated parallelogram crawler modules,” in *2014 IEEE International Conference on Robotics and Automation (ICRA)*, May 2014, pp. 1687–1692. 4

[46] A. Kakogawa and S. Ma, “Design of a multilink-articulated wheeled pipeline inspection robot using only passive elastic joints,” *Advanced Robotics*, vol. 32, no. 1, pp. 37–50, 2018. [Online]. Available: https://doi.org/10.1080/01691864.2017.1393348 4

[47] J. Bocko, M. Kelemen, K. Tatiana, and J. Jaromír, “Wheeled locomotion inside pipe,” *Bulletin of Applied Mechanics*, vol. 5, 01 2009. 4

[48] Y. Hürmüzlü and G. D. Moskowitz, “The role of impact in the stability of bipedal locomotion,” *Dynamics and Stability of Systems*, vol. 1, no. 3, pp. 217–234, 1986. [Online]. Available: https://doi.org/10.1080/02681118608806015 5

[49] Y. Hurmuzlu and G. Moskowitz, “Bipedal locomotion stabilized by impact and switching: I. two-and three-dimensional, three-element models,” *Dynamics and Stability of Systems*, vol. 2, pp. 73–95, 01 1987. 5, 63

[50] ——, “Bipedal locomotion stabilized by impact and switching: Ii. structural stability analysis of a four-element model.” *Dynamics and Stability of Systems*, vol. 2, pp. 99–112, 01 1987. 5, 63

[51] Y. Hurmuzlu, “Dynamics of Bipedal Gait: Part I—Objective Functions and the Contact Event of a Planar Five-Link Biped,” *Journal of Applied Mechanics*, vol. 60, no. 2, pp. 331–336, 06 1993. [Online]. Available: https://doi.org/10.1115/1.2900797 5

[52] ——, “Dynamics of Bipedal Gait: Part II—Stability Analysis of a Planar Five-Link Biped,” *Journal of Applied Mechanics*, vol. 60, no. 2, pp. 337–343, 06 1993. [Online]. Available: https://doi.org/10.1115/1.2900798 5

[53] T.-H. Chang and Y. Hurmuzlu, “Sliding Control Without Reaching Phase and Its Application to Bipedal Locomotion,” *Journal of Dynamic Systems, Measurement, and Control*, vol. 115, no. 3, pp. 447–455, 09 1993. [Online]. Available: https://doi.org/10.1115/1.2899122 5

[54] Y. Hurmuzlu and C. Basdogan, “On the Measurement of Dynamic Stability of Human Locomotion,” *Journal of Biomechanical Engineering*, vol. 116, no. 1, pp. 30–36, 02 1994. [Online]. Available: https://doi.org/10.1115/1.2895701 5

[55] Y. Hurmuzlu, C. Basdogan, and J. J. Carollo, “Presenting joint kinematics of human locomotion using phase plane portraits and poincaré maps,” *Journal of Biomechanics*, vol. 27, no. 12, pp. 1495–1499, 1994. [Online]. Available: https://www.sciencedirect.com/science/article/pii/0021929094901996 5

[56] Y. Hurmuzlu, C. Basdogan, and D. Stoianovici, “Kinematics and Dynamic Stability of the Locomotion of Post-Polio Patients,” *Journal of Biomechanical Engineering*, vol. 118, no. 3, pp. 405–411, 08 1996. [Online]. Available: https://doi.org/10.1115/1.2796024 5

[57] E. Borzova and Y. Hurmuzlu, “Passively walking five-link robot,” *Automatica*, vol. 40, no. 4, pp. 621–629, 2004. [Online]. Available: https://www.sciencedirect.com/science/article/pii/S0005109803003522 5

[58] Y. Hurmuzlu, F. Génot, and B. Brogliato, “Modeling, stability and control of biped robots—a general framework,” *Automatica*, vol. 40, no. 10, pp. 1647–1664, 2004. [Online]. Available: https://www.sciencedirect.com/science/article/pii/S0005109804000998 5, 44

[59] *A Hybrid of Impulsive and Continuous Control for Kneeless Bipedal Walking*, ser. Dynamic Systems and Control Conference, vol. ASME 2011 Dynamic Systems and Control Conference and Bath/ASME Symposium on Fluid Power and Motion Control, Volume 2, 10 2011. [Online]. Available: https://doi.org/10.1115/DSCC2011-6125 6

[60] A. Tavakoli and Y. Hurmuzlu, “Robotic locomotion of three generations of a family tree of dynamical systems. part ii: Impulsive control of gait patterns,” vol. 73, pp. 1991–2012, 2013. 6

[61] *Gravity Powered Locomotion and Active Control of Two Simple Systems*, ser. Dynamic Systems and Control Conference, vol. ASME 2009 Dynamic Systems and Control Conference, Volume 1, 10 2009. [Online]. Available: https://doi.org/10.1115/DSCC2009-2699 6

[62] *Gravity Powered Locomotion and Active Control of Three Mass System*, ser. Dynamic Systems and Control Conference, vol. ASME 2010 Dynamic Systems and Control Conference, Volume 2, 09 2010. [Online]. Available: https://doi.org/10.1115/DSCC2010-4194 6

[63] J. E. Wilson, “Walking toy,” Dec 1938. 6

[64] S. Mochon and T. A. McMahon, “Ballistic walking,” *Journal of Biomechanics*, vol. 13, no. 1, pp. 49–57, 1980. [Online]. Available: https://www.sciencedirect.com/science/article/pii/002192908090007X 6

[65] T. McGeer, “Passive dynamic walking,” *The International Journal of Robotics Research*, vol. 9, no. 2, pp. 62–82, 1990. [Online]. Available: https://doi.org/10.1177/027836499000900206 6

[66] A. Goswami, B. Espiau, and A. Keramane, "Limit cycles in a passive compass gait biped and passivity-mimicking control laws - autonomous robots," Sep 1997. [Online]. Available: https://link.springer.com/article/10.1023/A:1008844026298 6

[67] J. A. S. Kelso, K. G. Holt, P. Rubin, and P. N. Kugler, "Patterns of human interlimb coordination emerge from the properties of non-linear, limit cycle oscillatory processes: theory and data." *Journal of motor behavior*, vol. 13 4, pp. 226–61, 1981. 6

[68] M. Garcia, A. Chatterjee, A. Ruina, and M. Coleman, "The Simplest Walking Model: Stability, Complexity, and Scaling," *Journal of Biomechanical Engineering*, vol. 120, no. 2, pp. 281–288, 04 1998. [Online]. Available: https://doi.org/10.1115/1.2798313 6

[69] A. D. Kuo, "Stabilization of lateral motion in passive dynamic walking," *The International journal of robotics research*, vol. 18, no. 9, pp. 917–930, 1999. 6

[70] T. McGeer, "Passive walking with knees," *Proceedings., IEEE International Conference on Robotics and Automation*, pp. 1640–1645 vol.3, 1990. 6

[71] S. H. Collins, M. Wisse, and A. Ruina, "A three-dimensional passive-dynamic walking robot with two legs and knees," *The International Journal of Robotics Research*, vol. 20, no. 7, pp. 607–615, 2001. [Online]. Available: https://doi.org/10.1177/02783640122067561 6

[72] M. Spong and F. Bullo, "Controlled symmetries and passive walking," *IEEE Transactions on Automatic Control*, vol. 50, no. 7, pp. 1025–1031, July 2005. 6

[73] S. Ijaz, H. Li, M. C. Hoang, C.-S. Kim, D. Bang, E. Choi, and J.-O. Park, "Magnetically actuated miniature walking soft robot based on chained magnetic microparticles-embedded elastomer," *Sensors and Actuators A: Physical*, vol. 301, p. 111707, 2020. [Online]. Available: https://www.sciencedirect.com/science/article/pii/S0924424719310908 6

[74] A. T. Baisch, O. Ozcan, B. Goldberg, D. Ithier, and R. J. Wood, "High speed locomotion for a quadrupedal microrobot," *The International Journal of Robotics Research*, vol. 33, no. 8, pp. 1063–1082, 2014. [Online]. Available: https://doi.org/10.1177/0278364914521473 6

[75] A. T. Baisch, C. Heimlich, M. Karpelson, and R. J. Wood, "Hamr3: An autonomous 1.7g ambulatory robot," in *2011 IEEE/RSJ International Conference on Intelligent Robots and Systems*, 2011, pp. 5073–5079. 6

[76] A. T. Baisch and R. J. Wood, "Design and fabrication of the harvard ambulatory micro-robot," in *Robotics Research*, C. Pradalier, R. Siegwart, and G. Hirzinger, Eds. Berlin, Heidelberg: Springer Berlin Heidelberg, 2011, pp. 715–730. 6

[77] A. T. Baisch, P. S. Sreetharan, and R. J. Wood, "Biologically-inspired locomotion of a 2g hexapod robot," in *2010 IEEE/RSJ International Conference on Intelligent Robots and Systems*, 2010, pp. 5360–5365. 6

[78] *Microrobotics and Micromechanical Systems.* SPIE the International Society for Optical Engineering, 1996. 6

[79] A. Buzzin, A. Rossi, E. Giovine, G. de Cesare, and N. P. Belfiore, "Downsizing effects on micro and nano comb drives," *Actuators*, vol. 11, no. 3, 2022. [Online]. Available: https://www.mdpi.com/2076-0825/11/3/71 6

[80] F. Fettweis, B. Verrelst, and S. Bram, "Micro-range actuation by pressure-induced elastic deformation of 316l steel membranes produced by laser powder bed fusion," *Actuators*, vol. 10, no. 11, 2021. [Online]. Available: https://www.mdpi.com/2076-0825/10/11/296 6

[81] H. Zeng, O. M. Wani, P. Wasylczyk, and A. Priimagi, "Light-driven, caterpillar-inspired miniature inching robot," *Macromolecular Rapid Communications*, vol. 39, no. 1, p. 1700224, 2018. [Online]. Available: https://onlinelibrary.wiley.com/doi/abs/10.1002/marc.201700224 7

[82] S. Islam, K. Carter, J. Yim, J. Kyle, S. Bergbreiter, and A. M. Johnson, "Scalable minimally actuated leg extension bipedal walker based on 3d passive dynamics," *IEEE International Conference on Robotics and Automation.* [Online]. Available: https://par.nsf.gov/biblio/10335321 7

[83] G. Nandi, A. Ijspeert, and A. Nandi, "Biologically inspired cpg based above knee active prosthesis," in *2008 IEEE/RSJ International Conference on Intelligent Robots and Systems*, Sep. 2008, pp. 2368–2373. 7

[84] S. Kajita, F. Kanehiro, K. Kaneko, K. Fujiwara, K. Harada, K. Yokoi, and H. Hirukawa, "Biped walking pattern generation by using preview control of zero-moment point," in *2003 IEEE International Conference on Robotics and Automation (Cat. No.03CH37422)*, vol. 2, Sep. 2003, pp. 1620–1626 vol.2. 7

[85] T. Sugihara, Y. Nakamura, and H. Inoue, "Real-time humanoid motion generation through zmp manipulation based on inverted pendulum control," in *Proceedings 2002 IEEE International Conference on Robotics and Automation (Cat. No.02CH37292)*, vol. 2, May 2002, pp. 1404–1409 vol.2. 7

[86] R. Takano and M. Yamakita, "Sequential-contact bipedal running based on slip model through zero moment point control," in *2017 IEEE International Conference on Advanced Intelligent Mechatronics (AIM)*, July 2017, pp. 1477–1482. 7

[87] J. Pratt, J. Carff, S. Drakunov, and A. Goswami, "Capture point: A step toward humanoid push recovery," in *2006 6th IEEE-RAS International Conference on Humanoid Robots*, Dec 2006, pp. 200–207. 7

[88] M. M. Pelit, J. Chang, R. Takano, and M. Yamakita, "Bipedal walking based on improved spring loaded inverted pendulum model with swing leg (slip-sl)," in *2020 IEEE/ASME International Conference on Advanced Intelligent Mechatronics (AIM)*, July 2020, pp. 72–77. 7

[89] E. T. Whittaker, *A treatise on the analytical dynamics of particles and rigid bodies.* CUP Archive, 1964. 7

[90] T. R. Kane and D. A. Levinson, *Dynamics, theory and applications.* McGraw Hill, 1985. 7

[91] J. B. Keller, "Impact With Friction," *Journal of Applied Mechanics*, vol. 53, no. 1, pp. 1–4, 03 1986. [Online]. Available: https://doi.org/10.1115/1.3171712 7

[92] R. M. Brach, "Rigid Body Collisions," *Journal of Applied Mechanics*, vol. 56, no. 1, pp. 133–138, 03 1989. [Online]. Available: https://doi.org/10.1115/1.3176033 8

[93] Y. Hurmuzlu and T.-H. Chang, "Rigid body collisions of a special class of planar kinematic chains," *IEEE Transactions on Systems, Man, and Cybernetics*, vol. 22, no. 5, pp. 964–971, Sep. 1992. 8

[94] R. Du, S. Song, H. Yuan, D. Nie, and J. Gu, "Discussion on the stiffness of the drive chain in the legs of biped robots," *Actuators*, vol. 11, no. 3, 2022. [Online]. Available: https://www.mdpi.com/2076-0825/11/3/79 8

[95] K. B. Yesin, K. Vollmers, and B. J. Nelson, "Modeling and control of untethered biomicrorobots in a fluidic environment using electromagnetic fields," *The International Journal of Robotics Research*, vol. 25, no. 5-6, pp. 527–536, 2006. [Online]. Available: https://doi.org/10.1177/0278364906065389 8

[96] H. Choi, J. Choi, G. Jang, J. oh Park, and S. Park, "Two-dimensional actuation of a microrobot with a stationary two-pair coil system," *Smart Materials and Structures*, vol. 18, no. 5, p. 055007, mar 2009. [Online]. Available: https://doi.org/10.1088/0964-1726/18/5/055007 8

[97] S. Jeong, H. Choi, J. Choi, C. Yu, J. oh Park, and S. Park, "Novel electromagnetic actuation (ema) method for 3-dimensional locomotion of intravascular microrobot," *Sensors and Actuators A: Physical*, vol. 157, no. 1, pp. 118–125, 2010. [Online]. Available: https://www.sciencedirect.com/science/article/pii/S092442470900483X 8

[98] J. Kim, C. Park, J. Yoo, and S.-J. Kim, "Two-dimensional motion control of micro-robot by using two pairs of helmholtz coils," in *IEEE ISR 2013*, Oct 2013, pp. 1–2. 8

[99] A. W. Mahoney, D. L. Cowan, K. M. Miller, and J. J. Abbott, "Control of untethered magnetically actuated tools using a rotating permanent magnet in any position," in *2012 IEEE International Conference on Robotics and Automation*, May 2012, pp. 3375–3380. 8

[100] J. Li, H. Wang, Q. Shi, Z. Zheng, J. Cui, T. Sun, P. Ferraro, Q. Huang, and T. Fukuda, "Biped walking of magnetic microrobot in oscillating field for indirect manipulation of non-magnetic objects," *IEEE Transactions on Nanotechnology*, vol. 19, pp. 21–24, 2020. 8

[101] E. Al Khatib, A. Bhattacharjee, P. Razzaghi, L. W. Rogowski, M. J. Kim, and Y. Hurmuzlu, "Magnetically actuated simple millirobots for complex navigation and modular assembly," *IEEE Robotics and Automation Letters*, vol. 5, no. 2, pp. 2958–2965, April 2020. 8, 50, 68

[102] "Mandrel bending stainless steel pipe and tube facts," Nov 2018. [Online]. Available: https://www.highpurity.com/what-is-mandrel-bending 10

[103] Abdellatif, Mohamed, Mohamed, Hazem, Hesham, Mohamed, Abdelmoneim, Ahmed, Kamal, Amro, and Khaled, Ahmed, "Mechatronics design of an autonomous pipe-inspection robot," *MATEC Web Conf.*, vol. 153, p. 02002, 2018. [Online]. Available: https://doi.org/10.1051/matecconf/201815302002 10

[104] Y. Wang, H. Cao, and J. Jiang, "An improved method for estimating the domain of attraction of passive biped walker," *Discrete Dynamics in Nature and Society*, vol. 2019, p. 11, 2019. [Online]. Available: http://proxy.libraries.smu.edu/login?url=https://www.proquest.com/scholarly-journals/improved-method-estimating-domain-attraction/docview/2212651648/se-2

[105] L. B. Freidovich, U. Mettin, A. S. Shiriaev, and M. W. Spong, "A passive 2-dof walker: Hunting for gaits using virtual holonomic constraints," *IEEE Transactions on Robotics*, vol. 25, no. 5, pp. 1202–1208, 2009.

[106] J. da Silva, E. R. Salameh, M. V. Ötügen, and D. Fourguette, "Photonic Seismometer Based on Whispering Gallery Modes," *Seismological Research Letters*, vol. 93, no. 2A, pp. 753–762, 01 2022. [Online]. Available: https://doi.org/10.1785/0220210253

[107] J. H. Ginsberg, *Engineering dynamics.* Cambridge University, 2008. 44

[108] "Chapter 18 - fifty-two additional applications," in *Applied Dimensional Analysis and Modeling (Second Edition)*, second edition ed., T. Szirtes and P. Rózsa, Eds. Burlington: Butterworth-Heinemann, 2007, pp. 527–657. [Online]. Available: https://www.sciencedirect.com/science/article/pii/B9780123706201500241 50

[109] Y. Hurmuzlu and D. B. Marghitu, "Rigid body collisions of planar kinematic chains with multiple contact points," *The International Journal of Robotics Research*, vol. 13, no. 1, pp. 82–92, 1994. [Online]. Available: https://doi.org/10.1177/027836499401300106

[110] S. Miyakoshi and G. Cheng, "Ballistic walking by compass-like biped walker: Exploiting physical dynamics in achieving human-like walking," in *International Conference Series on Climbing and Walking Robots*, 01 2002. 42

[111] J. Abbott, "Parametric design of tri-axial nested helmholtz coils," *Review of Scientific Instruments*, vol. 86, p. 054701, 05 2015. 68

[112] Y. Hurmuzlu, "Complementarity Relationships and Critical Configurations in Rigid-Body Collisions of Planar Kinematic Chains With Smooth External Contacts,"

Journal of Applied Mechanics, vol. 87, no. 12, 09 2020, 121004. [Online]. Available: https://doi.org/10.1115/1.4048189 52

[113] E. R. Westervelt, J. W. Grizzle, C. Chevallereau, and B. Morris, *Feedback control of dynamic bipedal robot locomotion*, 1st ed., ser. Automation and Control Engineering. CRC Press, 2007, vol. 28. 63

[114] M. Kashki, J. Zoghzoghy, and Y. Hurmuzlu, "Adaptive control of inertially actuated bouncing robot," *IEEE/ASME Transactions on Mechatronics*, vol. 22, no. 5, pp. 2196–2207, 2017. 63